CLOSED LOOP FORCE CONTROL FOR A ROBOTIC GRINDING SYSTEM

by

Allan Robert Tate

B.S.M.E., Tufts University
(1981)

Submitted to the Department of Mechanical Engineering
in partial fulfillment of the requirements
for the degree of

MASTER OF SCIENCE
IN MECHANICAL ENGINEERING

at the

MASSACHUSETTS INSTITUTE OF TECHNOLOGY

June 1986

Signature of Author: _____
Department of Mechanical Engineering
June 1986

Certified by: _____
Alexander C. Edsall
Technical Supervisor

Certified by: _____
Bruce K. Walker
Thesis Supervisor

Accepted by: _____
Ain A. Sonin
Chairman, Department Committee

DISCLAIMER

The views and conclusions expressed in this thesis are those of the author and should not be interpreted as necessarily representing the position of the National Science Foundation, The Charles Stark Draper Laboratory, Inc., or the Massachusetts Institute of Technology.

CLOSED LOOP FORCE CONTROL FOR A ROBOTIC GRINDING SYSTEM

by

Allan Robert Tate

B.S.M.E., Tufts University
(1981)

Submitted to the Department of Mechanical Engineering
in partial fulfillment of the requirements
for the Degree of Master of Science

ABSTRACT

As a step toward automating the process of weld bead grinding, a robot was used to manipulate an industrial grinder and control the normal force applied to the workpiece. This robot was part of a prototype system that incorporated off-the-shelf hardware. A nonlinear force control law was designed with the ability to track a wide variety of desired force profiles, reject positional disturbances such as jigging errors, and remain stable. The maximum normal force controlled was 40 N and the maximum frequency of the reference force was 2.23 Hz.

Before designing the force controller, a model of the robot system in contact with the workpiece was developed. System identification techniques were used to estimate the frequency response relating output force to input displacement. The dynamic characteristics of this system were dominated by a time delay in series with a nonlinear compliance.

A number of designs for force control laws, including proportional and PI controllers, are presented along with experimental and simulated results. Overall, the best performance was achieved using a nonlinear force control law. This control law is presented in a form that is applicable to most plants that can be modeled as a time delay followed by a compliance.

Thesis Supervisor: Bruce K. Walker

Title: Associate Professor of Aeronautics and Astronautics

ACKNOWLEDGEMENTS

I thank the National Science Foundation for their financial support (grant #ECS-8214366) of this thesis and my graduate studies at MIT. James L. Nevins offered me the opportunity to perform this work in his department at the Charles Stark Draper Laboratory. I also thank the Eastman Kodak Company, especially Frank A. Mondziel, for their help and for granting me a leave of absence.

My technical advisor, Alexander C. Edsall, provided the communication software between various system elements that were used throughout this research. His guidance, assistance, and encouragement on a daily basis made this work possible.

I thank my thesis advisor, Professor Bruce K. Walker for guidance, insights at critical stages, and support.

All of the members of the Robotics and Assembly Systems Division of Draper Laboratory have been helpful in this research. Thomas M. Stepien and Dr. Daniel E. Whitney taught me a great deal about force control and robotics. Their insights were critical for organizing my thoughts during the preparation of this document. Reginald C. Roderick Jr. and Robert P. Fields built some of the hardware components for this research. All of the students with whom I worked provided support in countless ways. Also, the help I received from the computer consulting office and the Draper Library was appreciated.

I thank my professors at MIT, William K. Durfee and Jean-Jacues E. Slotine, who taught me control theory. Their suggestions were helpful in solving some of the problems that were encountered. Also, I appreciate the time that Professor Neville Hogan spent to teach me the fundamentals of impedance control.

Jim Lidington of Bruel & Kjaer Instruments, Inc. provided some of the test equipment used in this research.

Finally, I thank all of my friends for their careful editing of this document.

I wish to dedicate this thesis to Luanne and to my family.

TABLE OF CONTENTS

LIST OF ILLUSTRATIONS

LIST OF TABLES

1.0 INTRODUCTION

This thesis addresses the problem of using a robot to manipulate an industrial grinder and control the normal force applied to a workpiece. The results of this research will be used in the development of a soft-disk, automated grinding system. The specific purpose of this system is to grind weld beads flush with the parent material. For example, this type of system could be used in the automobile industry to grind the welds on car bodies before spray painting. Figure 1 shows the conceptual arrangement of the robot, grinding disk, and workpiece.

The PUMA 560 robot using VAL-II was used in the development of a prototype grinding system. VAL-II is a programming language and control system for the robot. A communication capability is available with VAL-II for modification of the robot's trajectory from an external computer. VAL-II superimposes external inputs on the motion defined by the robot control program. Specifically, for this system, VAL-II allowed real time control of the robot path by an IBM PC-AT computer.

Section 2 discusses the motivation for this research as part of the overall goal of developing an automated grinding system. The goal is to use the normal force between the grinding disk and workpiece as an indi-

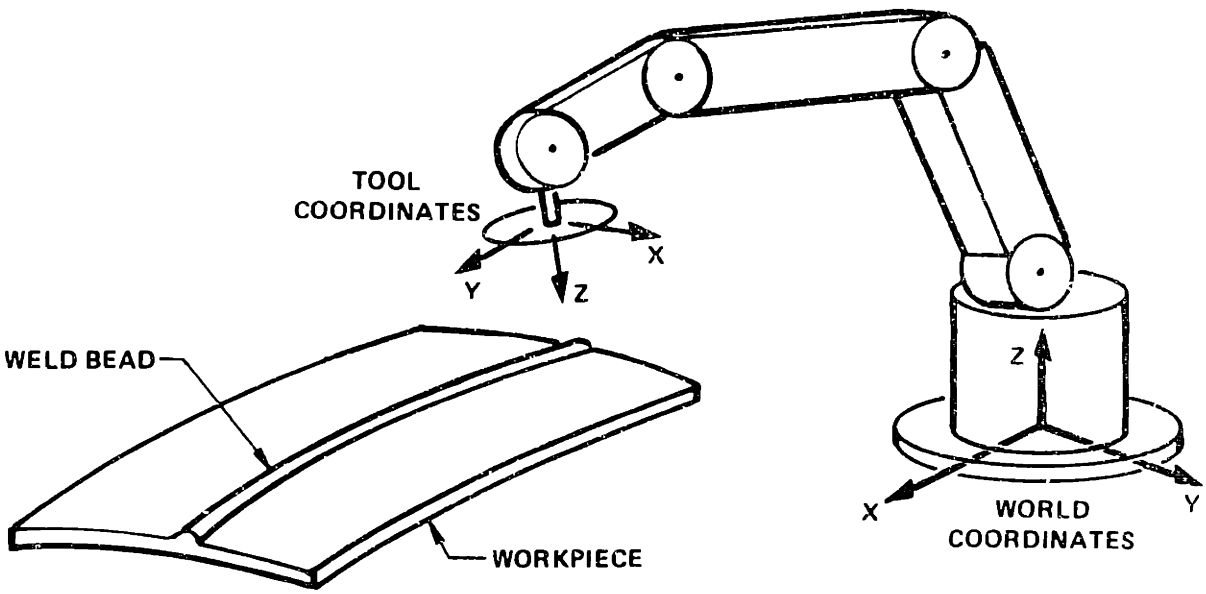

Figure 1. Conceptual arrangement of robot, grinding disk, and workpiece: Tool and world coordinates illustrated

rect way of controlling the material removal rate. In addition, Section 2 introduces the following topics: 1) the major components of the proposed grinding system, 2) the previous research in force control and modeling robot dynamics, 3) the prototype system used for this thesis, and 4) the scope of this research.

Section 3 discusses the modeling of the plant, which consists of the PUMA robot and VAL-II without workpiece contact. The model was based on an experimentally determined frequency response function for the plant. System identification techniques were applied to the input and output displacement histories to estimate the frequency response function. The inputs were sinusoidal or random sequences specified for a single tool coordinate. These sequences were sent by the IBM PC-AT supervisor to VAL-II (tool coordinates are illustrated in Figure 1). The output was the actual displacement of the robot's end effector. This displacement was calculated in the frequency domain from measurements of the end effector acceleration. The major result was that the dominant characteristic of the plant, up to 10 Hz, was a time delay. The specific procedures, techniques, and experimental results are discussed in this section.

The plant model was then extended to include contact with the workpiece. Section 4 examines the effect of this contact on the dynamic model for the robot and VAL-II. An Astek six axis force and torque sen-

sor was attached to the to the robot's end effector. The rubber backing that holds the grinding disk was mounted on the force sensor (the grinder and grinding disk were not mounted in this experiment). The system identification techniques mentioned above were modified to estimate the frequency response function relating output force and input displacement. The input displacements were small enough to allow a linear model of the plant compliance. Two different rubber backings (of different composition and form) were tried with initial contact forces ranging from 250 to 2000 dN. In all cases the dominant characteristic of the plant was the same as found in Section 3, a time delay up to 10 Hz.

To complete the model of the system in contact with the workpiece, the nonlinear plant compliance was modeled. This was done experimentally and the results are presented in Section 5. In this experiment, the grinding disk was mounted on the rubber backing. This is because the presence of the grinding disk was found to have a significant effect on the overall plant compliance. Force measurements during low frequency sinusoidal inputs were used to generate plots of measured force vs. end effector displacement. End effector displacement was estimated from the commanded displacement by accounting for the time delay.

An integrated model of the plant in contact with the workpiece and coupled with the IBM PC-AT supervisor is presented in Section 6. A num-

ber of force control laws were designed for this integrated system. They were tested experimentally and the results were compared. Experiments were performed using the laboratory setup and using simulations written in CTRL-C. The best overall performance was achieved by using a nonlinear controller. A general derivation of this controller is presented that is applicable to any system that can be modeled as a time delay followed by a compliance. However, the compliance must be capable of being modeled such that measured force is a monotonic function of displacement.

Conclusions and recommendations for future research are presented in Section 7. Also, prelimary results from an experiment in which normal force was controlled during grinding are presented. In the opinion of the author, it will be possible to indirectly control the material removal rate by controlling the normal force applied by a robot. When controlling the material removal rate, the accuracy required of the force controller depends on the specifications of the part being ground. If a robot is capable of delivering force to the relevant tolerances, then this research can be used in the development of an automated grinding system.

2.0 MOTIVATION AND SCOPE OF THIS RESEARCH

The Charles Stark Draper Laboratory (CSDL) has been researching automation systems and their application to manufacturing for 20 years. As a focus for current research, CSDL is using robots and machine vision to automate the process of grinding weld beads. This technology could be applied in the automobile and shipbuilding industry where the grinding of weld beads is currently done manually. In addition, the development of an automated grinding workstation will illustrate technical capabilities that may be applied to future automation problems.

A model of the grinding process is necessary for the development of an automated grinding system. Grinding, however, is a poorly understood process. CSDL is currently developing a grinding model. Ivers[8] showed that material removal is a function of the power applied to the contact patch, which is the area of contact between the grinding disk and the workpiece. Applied power can be indirectly controlled by regulating wheel speed and normal force. This thesis examines the feasibility of using this normal force as an indirect means of controlling the material removal.

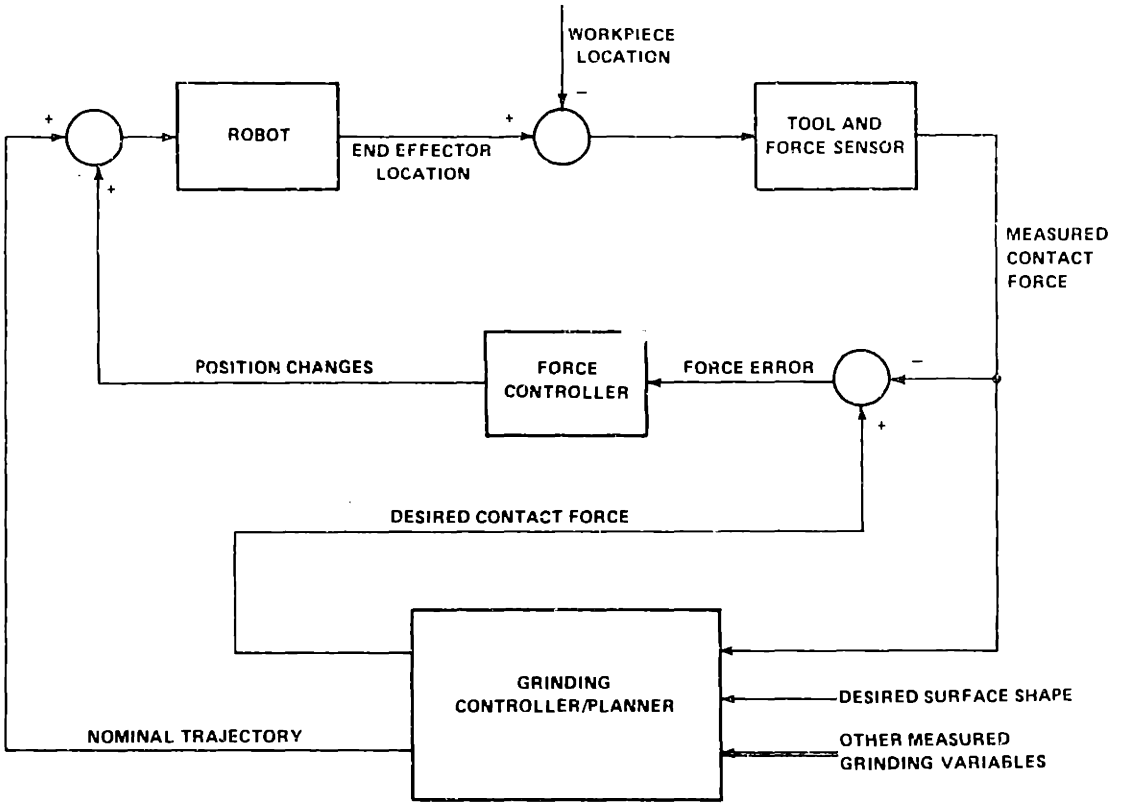

Figure 2. Block diagram of the proposed grinding system

2.1 PROPOSED GRINDING SYSTEM

An overall block diagram of the proposed grinding system is shown in Figure 2. The nominal trajectory is a sequence of position-controlled motions. This trajectory will be calculated prior to each grinding pass based on the weld's nominal contour and a trajectory specification. The nominal contour is the system's estimate of of the shape of the weld surface. Normal force will be controlled by updating the nominal trajectory of the robot in real time. When the trajectory is modified, the

grinding disk will contact the workpiece and the resulting contact force will cause the grinding system and workpiece to deform. Force feedback will be provided by a force sensor attached between the robot's end effector and the grinder.

Parts assembled or machined by current automated workstations must conform to tight dimensional specifications. Welds, however, vary in shape; so the proposed system will have to plan a task strategy for each workpiece. The strategy includes planning the nominal trajectory and the desired contact force prior to each grinding pass. To calculate the nominal trajectory, the system must have the ability to recognize and measure geometrical aspects of the weld. One geometrical aspect of the weld is the nominal contour; another is the weld bead's volume as a function of position along the length of the weld. One possible measurement system, which is currently being investigated at CSDL, is a structured light vision system[19]. It will provide a method of handling welds that are not uniform in shape.

The nominal contour for the weld and a trajectory specification will be used to calculate the nominal trajectory. For example, the nominal trajectory could be specified to keep the contact patch and the contact angle constant in tool coordinates. In this case, the contact patch could also be specified to move along the nominal contour. The resulting nominal trajectory is a set of vectors that describe the position

and orientation of the grinding disk as a function of time. The desired normal force will be calculated as a function of position along the weld in an effort to predict the material that will be removed. This calculation will be based on the grinding model, the current status of the grinding disk, and the weld volume at the contact patch. The material removed on each pass is planned to minimize costs. The time required to complete the job, the life expectancy and sharpness of the grinding disk, and the percentage of ruined parts are some of the factors that will determine cost.

After each grinding pass, the proposed system will update the grinding model parameters and the grinding disk status. This will be done using measurements of the actual material removed and the stored contact force information. Measurements of material removed could be made by the vision system. The system will be able to determine, from measurement histories, when the disk is worn out and change it.

A possible scenario for grinding a weld with the proposed workstation is summarized as follows. A workpiece with a weld to be ground will be transported to the workstation. A data base describing the geometric characteristics of the weld will be generated by the vision system. The nominal trajectory and desired contact force history will be calculated. The robot will begin following the nominal trajectory. When the beginning of the weld is reached, force control starts. The

system will remove the desired material by controlling the normal force applied to the weld. After the pass is complete, the geometry of the weld will be measured again by the vision system. The grinding model parameters and disk status will be updated. If necessary, the grinding disk will be changed. The next grinding pass will be planned, and the sequence repeated until the weld is ground flush with the parent material[9].

2.2 PREVIOUS RESEARCH IN FORCE CONTROL AND ROBOT MODELING

Force control of robot manipulators is a topic of practical importance. It must be considered whenever a manipulator interacts with the environment. Goertz first recognized the problem in the late 1940's during the development of teleoperator arms[13]. He recognized the difficulty in manipulating objects with a purely position-controlled device. It is necessary for the operator, or controller, to sense forces between the end effector and the environment. Many tasks that have been automated, such as spray painting and welding, require little direct interaction between the robot and the workpiece. Other tasks, such as assembly, require some interaction, but the forces are relatively small. In order to expand the range of robot tasks to include jobs

such as grinding, issues of force interaction must be more fully investigated. The solution includes: 1) analysis of task goals to determine a strategy to accomplish the task, 2) analysis of the system to determine a suitable model, 3) determining how to measure forces, 4) designing a force control algorithm, and 5) stabilizing the control system.

Current robot manipulators are usually position-controlled devices. Linkages are actuated by rotary servo motors or stepper motors and their state, consisting of position and velocity, is measured by joint encoders and tachometers. Position control is often not an adequate method of controlling the manipulator after contact is made with the environment. Interaction with the environment introduces a positional constraint. The contact force causes a deformation of the manipulator and environment. The magnitude of the contact force depends on the total compliance of the manipulator and the environment. The compliance of a position-controlled manipulator is determined by the construction of the robot, the strength of the motors, and the controller gains. For many tasks that require interaction, it is desirable to increase the manipulator compliance along one or more degrees of freedom (DOF).

For example, consider an assembly task with a six-DOF, position-controlled manipulator. If the manipulator and the parts are relatively stiff, then the parts must be accurately positioned by the manipulator for them to mesh. Positional errors can cause unwanted contact between

the parts when they are assembled. Manipulators, however, have limited repeatability and accuracy. The tolerance to position errors during assembly can be increased by adding compliance along specific DOFs. In the late 1970's, CSDL developed a passive solution called the Remote Center Compliance (RCC) [4] [12] . This device attaches to the robot's end effector to provide the "give" needed for assembly.

Active control schemes provide the manipulator with compliance through the control system. A review of force feedback architectures is given by Whitney [24]. In general, the robot is commanded along some nominal trajectory or velocity. At some point, contact occurs between the robot and its environment. Their collective deformation and stiffness give rise to forces that react directly on the robot's joints. The contact forces are also sensed and fed to the force controller. The controller uses this feedback to modify the nominal trajectory.

For example, in stiffness control, the force vector is fed back through a 6 x 6 compliance matrix. The resulting position summed with to the original position command. If the force vector is in tool coordinates, then the apparent stiffness of the end effector can be adjusted by selecting desired values of the compliance matrix. Damping control is essentially an integrating controller; desired velocity is specified instead of desired position. Sensed forces are multiplied by an admittance matrix to give rise to velocity modifications. Hogan[6] discusses

the concept of impedance control, which is a generalization of stiffness and damping control.

Another active control scheme is hybrid force/position control. A hybrid controller allows force to be commanded along certain DOFs and position to be commanded along the remaining DOFs. DOFs are often naturally divided when a manipulator interacts with the ervironment. This division is described within a compliance frame. For example, consider putting a peg in a hole. The compliance frame is chosen so that one axis, the z-axis, coincides with the peg axis. Translation along and rotation about the z-axis are position-controlled, while the other degrees of freedom are force-controlled. Raibert[15], Craig [3] , and others discuss this technique.

The system must be specified and a model determined before a force controller can be designed. This model must include the robot manipulator because the manipulator contributes significantly to the overall plant dynamics. There are two general approaches to modeling a plant. One approach is to analyze internal dynamics based on physical laws to form a model that predicts the input/output behavior. Another approach is to analyze the input/output behavior and form a model that describes this behavior, but does not describe the internal dynamics. In this research, the plant is modeled by analysis of the input/output behavior.

The internal dynamics of robotic manipulators have been analyzed and modeled for 20 years. In early models, the manipulator was assumed to be a linkage of rigid bodies. Dynamic equations are derived by the Newton - Euler method, the Lagrange method, or other methods. Link parameters, such as mass and moment of inertia, are determined by disassembling a robot and carefully measuring the links. Armstrong, et al.[1], performed this procedure on a PUMA 560 arm and expressed the dynamics in the following form.

$$A(q)q'' + B(q)[q'q'] + C(q)[q'^2] + g(q) = \Gamma \qquad (1)$$

where

$q' = dq/dt$,

and

$A(q)$ is the nxn kinetic energy matrix,
$B(q)$ is the nxn(n-1)/2 matrix of Coriolis torques,
$C(q)$ is the nxn matrix of centrifugal torques,
$g(q)$ is the n vector of gravity torques,
q'' is the n vector of accelerations,
Γ is the joint torque vector.

The vector $[q'q']$ is the n(n-1)/2 vector of velocity products. It is given by:

$$[q'_1q'_2,\ q'_1q'_3 \cdots q'_1q'_n,\ q'_2q'_3,\ q'_2q'_4 \cdots q'_{n-2}q'_n,\ q'_{n-1}q'_n]^T.$$

The vector $[q'^2]$ is the n vector of squared velocities. It is given by:

$$[q'^2_1,\ q'^2_2\ \ldots\ q'^2_n]^T.$$

For a typical manipulator, equations like (1) have hundreds of terms and are extremely complex. Many researchers have simplified these equations to reduce computation time [7].

Experimental results, by Good, et al.[5], have shown that this type of model is inadequate for many robot designs. The major weakness is that the drive system is modeled as a pure torque source or first order lag. This assumption is a poor one because of compliant elements in the robot's drive system. Very few studies account for this compliance. In the derivation of equation (1), the arm is modeled as a linkage of rigid bodies. There are unmodeled motions caused by flexibility in the linkages connecting the drive systems to the arm members. There is also bending and torsion of the arm members themselves. Nonlinear effects are not modeled. These include viscous damping, coulomb friction for motor and load inertias, and backlash.

To account for the unmodeled dynamics, Good used system identification and structural dynamic analysis techniques. For example, the dynamic response, from 0 to 50 Hz, of the integrated drive, for each axis, was found. The drive system included the drive motor, harmonic drive, linkages, and arm. Motor current and arm motion were recorded as the servo motor was excited with random or sinusoidal input signals.

The frequency response function was estimated using FFT analysis. This type of research has led to more complete models of robot manipulators and trajectory controllers[5].

2.3 EXPERIMENTAL SYSTEM AND SCOPE OF THIS RESEARCH

The prototype system used in this thesis for force control experiments is shown in Figure 3. The PUMA 560 robot arm is in the background. Attached to the end effector is the Astek FS6-120A-200 six axis force and torque sensor. The grinding disk and backing are attached to the force sensor. The IBM PC-AT is on the left and the terminal for VAL-II is on the right. Note that the system does not include a grinding motor. The payload capacity of the PUMA (5 lb) is too small to manipulate more than a light duty industrial grinder.

A hybrid force/position controller was designed for this prototype system. The nominal trajectory was a straight line path manually taught to VAL-II. Force was measured by the force sensor and fed back to the IBM PC-AT. The desired force profile (i.e., constant, sinusoidal) was predetermined and stored in the memory of the IBM PC-AT before each experiment. The force feedback control strategy was programmed into the

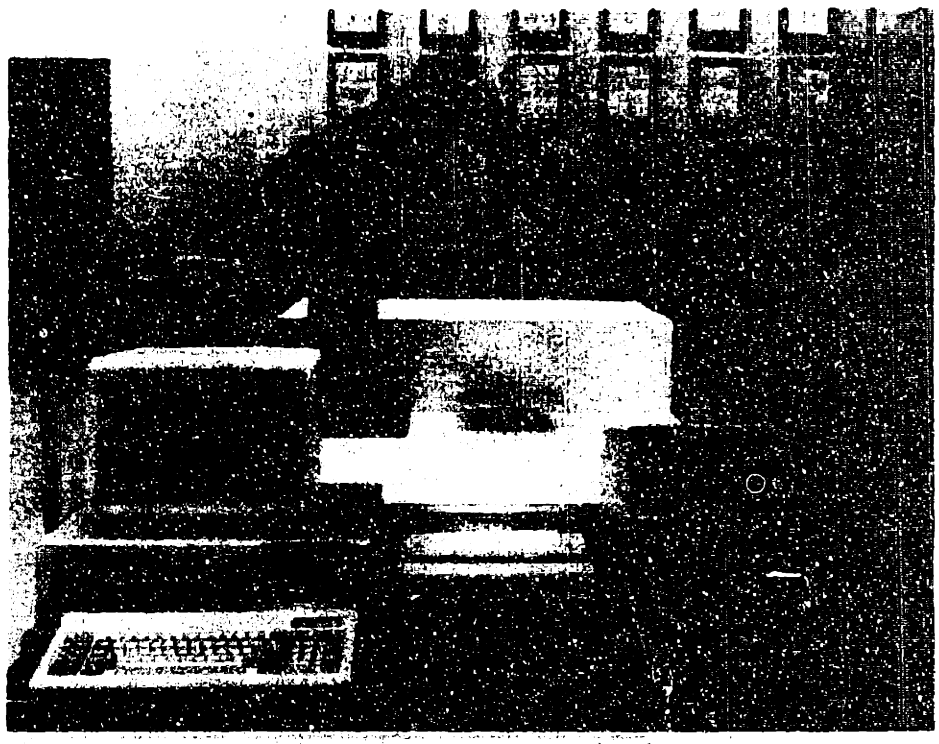

Figure 3. Overall setup for force control experiments

IBM PC-AT. The tool z-component of the commanded manipulator trajectory was updated every 28 ms by the control strategy. This update was passed from the IBM PC-AT to VAL-II and summed with the nominal trajectory. The other trajectory components were position-controlled only. Compliance was primarily provided by the grinding disk and rubber backing. Some compliance was present in the robot gear mechanisms, but this was considered negligible compared to the disk and backing. Stepien,et al. [17] [18] , discuss a robotic system that uses a similar force control architecture. Their system was tested in a deburring application.

As discussed, the z-position commands sent from the IBM-PC to VAL-II were in tool coordinates. The corresponding joint position changes were calculated by the VAL-II software and were transparent to the force controller. Paul[13] discusses the translation of position in tool coordinates to joint coordinates. Future systems may have a need for a multiple axis strategy. For example, force feedback could be used to determine if the contact patch is properly positioned on the weld. The disk angle and feedspeed were not varied in these experiments. The speed of the robot was constant along the nominal path over the weld.

VAL-II has a kinematic model of the PUMA embedded in its software that is used for trajectory control. No attempt was made in this research to change or improve this model or VAL-II's trajectory control-

ler. This research shows that force can be controlled with relatively inexpensive off-the-shelf hardware without modifications.

3.0 FREQUENCY RESPONSE OF PUMA ROBOT WITHOUT WORKPIECE CONTACT

In this section, the frequency response characteristics of the plant consisting of the PUMA robot and VAL-II are discussed. The frequency response relating output displacement to input displacement commands was estimated using system identification techniques. A plant model was constructed based on the frequency responses obtained. The dominant characteristic of the plant, up to 10 Hz, was found to be a time delay, and this is the model proposed in Section 3.4.

The modeling techniques presented in this section differ from those discussed in Section 2. In this research, the PUMA was not divided into components as was done by Good[5] or Armstrong [1] . Rather, the PUMA and VAL-II were considered as an integrated plant and this plant was identified from the input and output displacement histories. Figure 4 shows the PUMA robot with its associated electronics and VAL-II in detail. This figure illustrates the plant along with the input and output signals that were used to identify it.

The general procedure for each experiment is as follows. The robot was configured in a fixed position without workpiece contact. A series of displacement commands from the IBM PC-AT supervisor commanded the

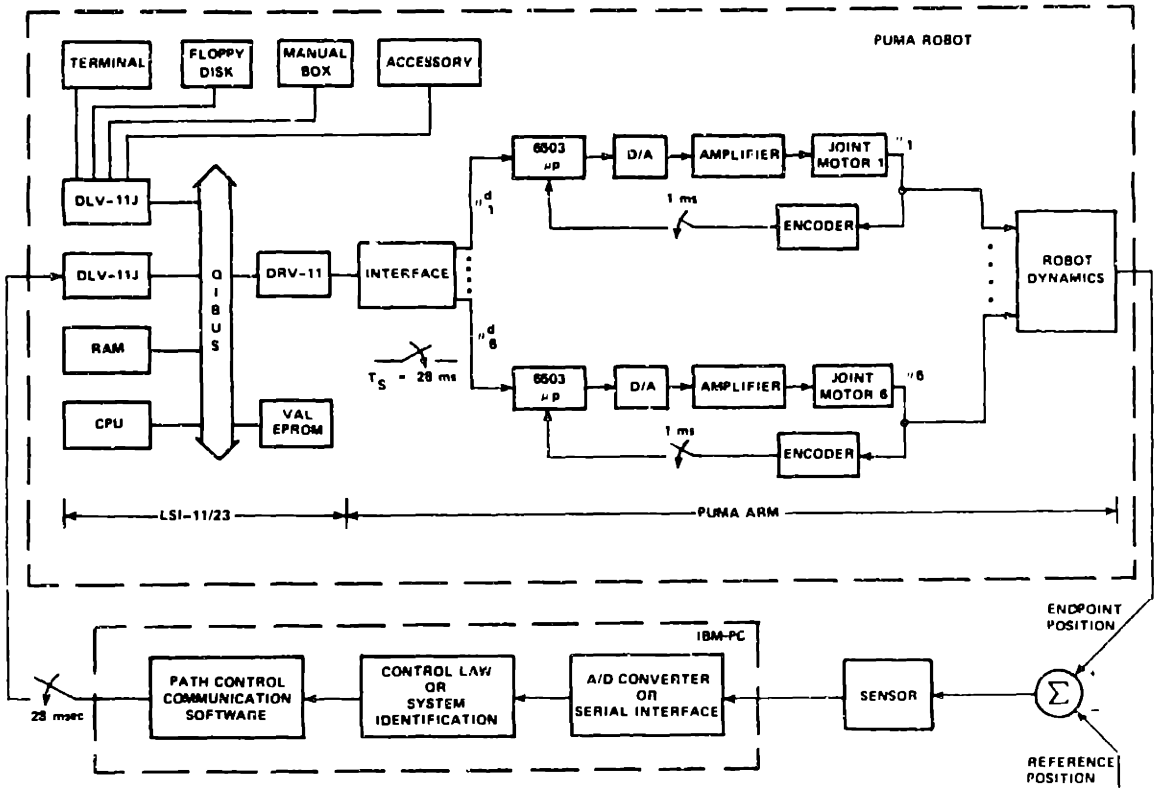

Figure 4. PUMA robot system

robot to move along a single tool coordinate axis. The inputs included sinusoidal and prefiltered random signals. An accelerometer was fixed to the robot's end effector to measure acceleration. The accelerometer output was passed through a Butterworth anti-aliasing filter and then sampled and stored. The cross-spectral and auto-spectral densities were estimated using the method of averaging periodograms and a Hamming window. The frequency response of the system was then estimated from the spectral densities. The experiment was repeated with different masses attached to the endpoint and various positions in the robot's workspace. The frequency responses were verified at intermittent discrete frequencies using sinusoidal inputs. These techniques are explained in Section 3.3.

3.1 EXPERIMENTAL SETUP

The four positions in which the robot was tested were chosen to illustrate how the frequency response changes with the robot's configuration. For each position shown in Figures 5 through 8 the robot was commanded to move along the tool z-axis. These positions, in world coordinates, are specified in Table 1. The response for the tool z-direction is considered the most important because this is the axis

Table 1. Positions of robot in world coordinates

Position	X	Y	Z	ϕ	θ	ψ
1	211.13	670.97	-38.75	174.78	42.52	-96.93
2	202.91	780.97	-57.09	-88.32	89.95	0.0
3	207.41	629.66	-56.97	-88.32	89.96	0.0
4	214.94	371.81	-56.78	-88.32	89.96	0.0

X, Y, Z are distances in mm.
ϕ, θ, ψ are Euler angles in degrees.

along which the force is to be controlled. Tests were also performed in position 3 with the accelerometer mounted on the tool x-axis and tool y-axis. Figure 9 shows the accelerometer mounted on the tool y-axis. Payload can be varied by changing the weight shown. Cross coupling between axes was measured by mounting the accelerometer orthogonal to the excitation axis.

Additional apparatus needed for these experiments is described below.

- Bruel & Kjaer 4381 accelerometer
  - Charge sensitivity (pC/g): 99.6
- Accelerometer mount
  - Weight including bolt (kg): 0.448
  - Additional payload #1 (kg): 1.157
  - Additional payload #2 (kg): 1.957

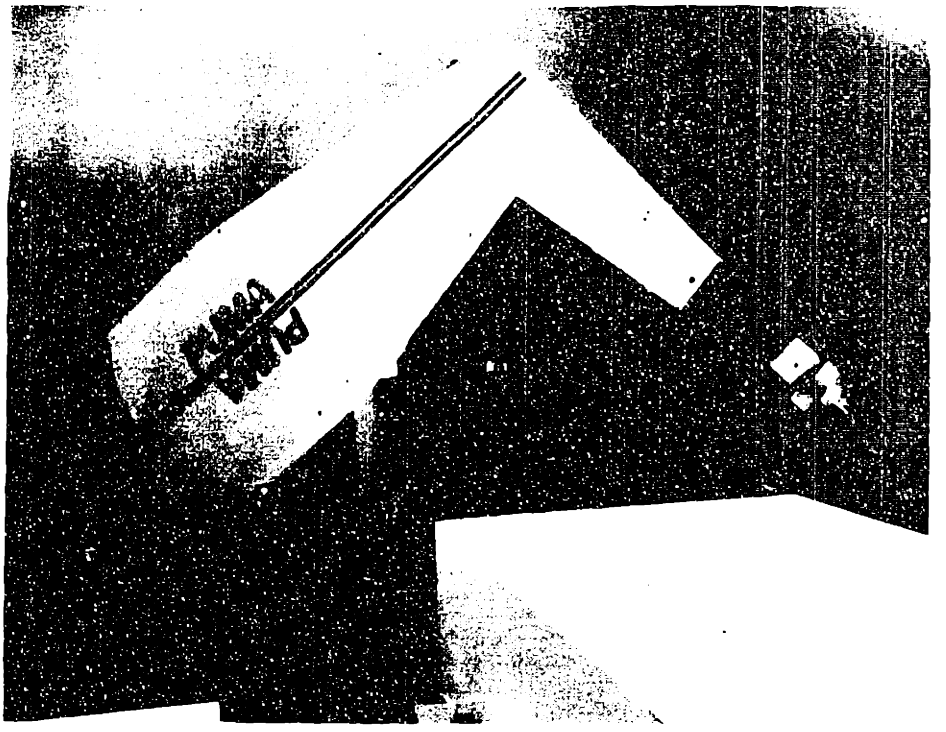

Figure 5. Experimental position 1

- Bruel & Kjaer 2635 charge amplifier; Setup:
  - Transducer Sensitivity (pC/g): 99.6
  - Output gain (mV/g): 100.0
  - Upper frequency limit (kHz): 0.1
  - Lower frequency limit (Hz): 0.2
  - Output set for acceleration
- Analog anti-aliasing filter

Three pole Butterworth low-pass filter with 15 Hz. cutoff frequency. The sampling period for these experiments is 0.028 sec, so the Nyquist frequency is 17.9 Hz.

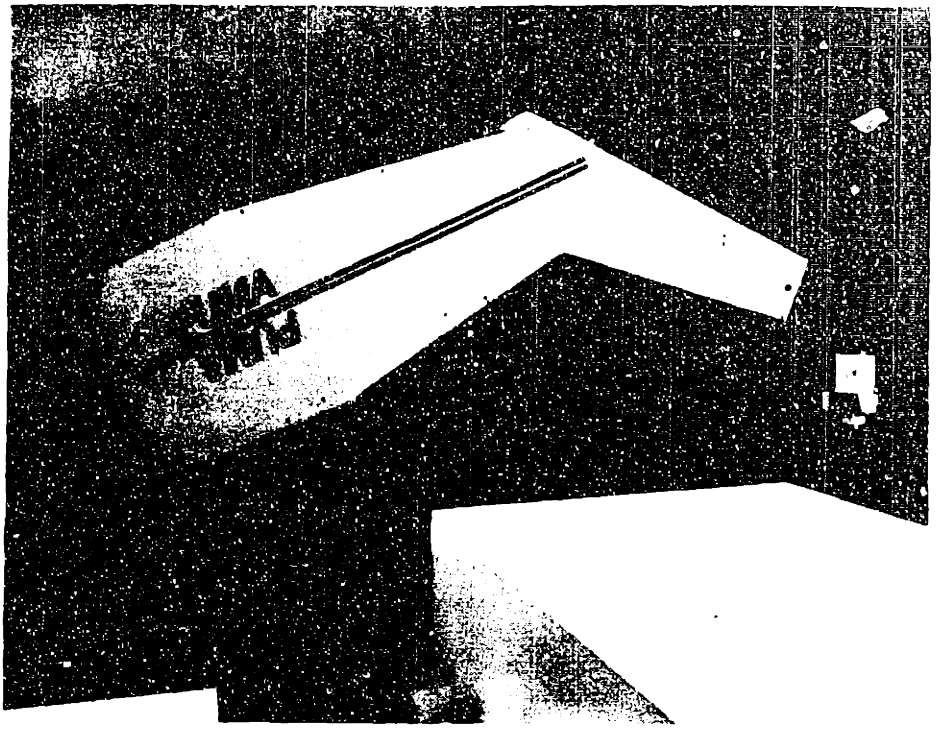

Figure 6. Experimental position 2

3.2 SYSTEM INPUTS

The frequency response was estimated at 4 frequencies using sinusoidal inputs that were sampled every 0.028 seconds for a total sequence length of 1024 samples (28.672 s). The periods of the input signals were chosen to divide evenly into 28.672 s. The amplitudes were chosen to achieve a peak acceleration of at least 0.25 g. In addition, it was desired that the maximum displacement be small, but at least 3.1 mm (100 counts). A count is the smallest displacement change that can be com-

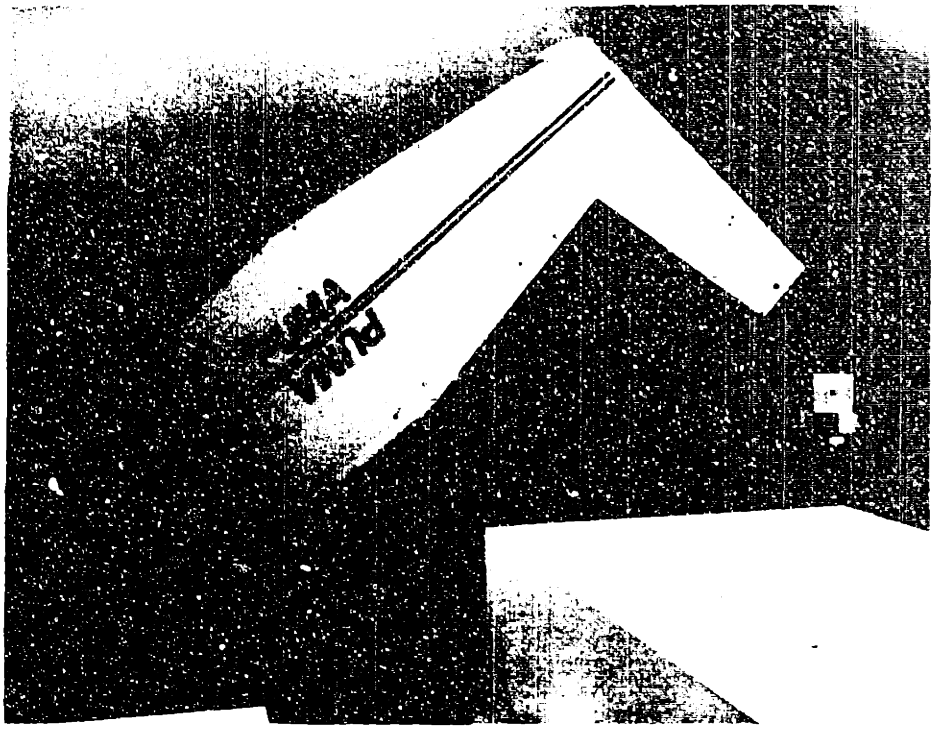

Figure 7. Experimental position 3

manded and is equal to 0.03125 mm (0.00123 in.). The details are given in Table 2. Note that four steps per cycle is the highest reasonable frequency because this produces a triangular waveform.

The random input was also a sequence of 1024 samples. The goal was to create a sequence of displacements that have a flat acceleration spectrum. If $S(d)$ is the displacement spectrum, then the acceleration spectrum is given by $-\omega^2 S(d)$. Thus, a flat displacement spectrum would imply large acceleration power at high frequencies that could be damaging to the robot. To approximate the desired spectrum, a flat displace-

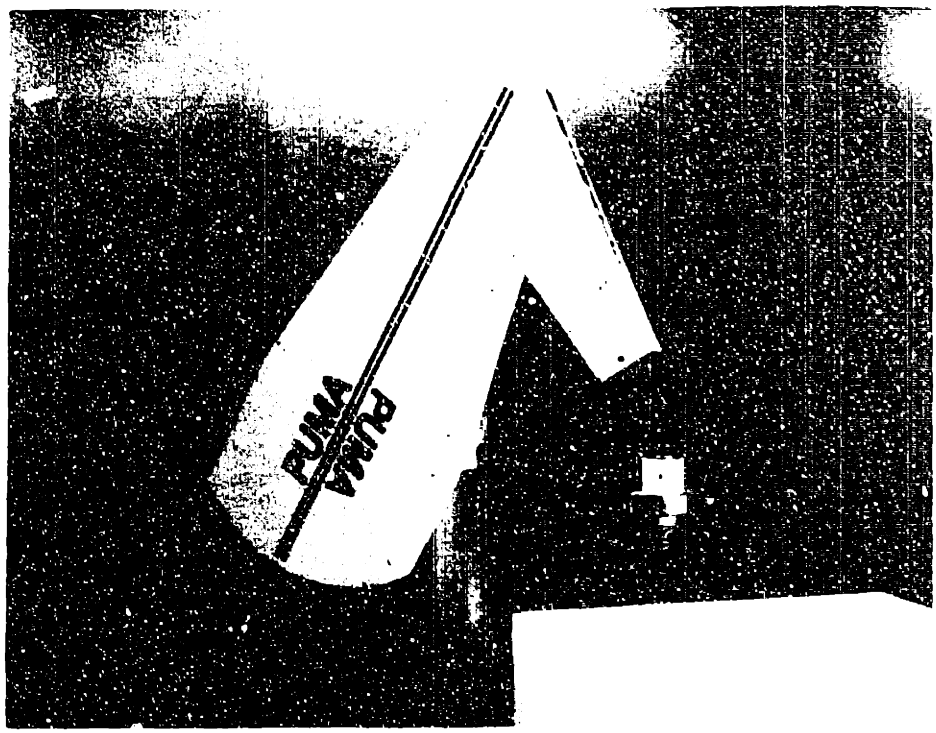

Figure 8. Experimental position 4

ment random sequence was low-pass filtered. The actual acceleration spectrum falls off rapidly below 0.6 Hz and above 10.0 Hz. The procedure for generating the random input signal is summarized as follows:

- Use a pseudo-random number generator that gives floating point numbers uniformly distributed between -1/2 and +1/2.

- For each element of the array, add 3 numbers from the uniform distribution. The distribution of the array elements will be

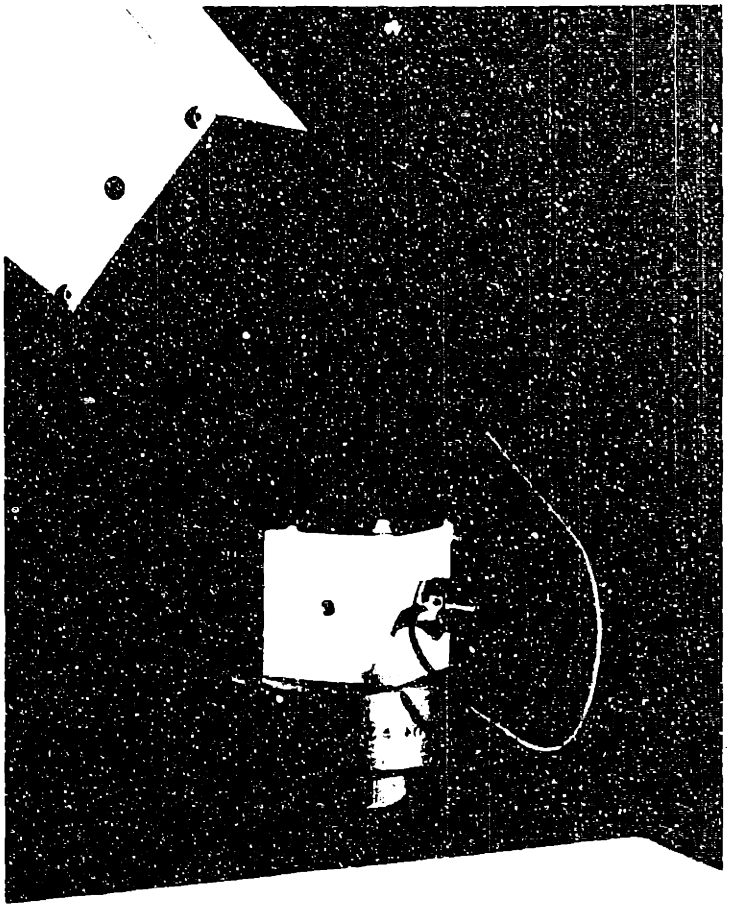

Figure 9. Accelerometer mounted on tool y-axis

approximately gaussian with an approximate mean of 0.0 and standard deviation of 0.5.

- Scale the data to the appropriate maximum amplitude, convert to counts, round off, and store as a sequence of integers.

- Pass the data through a digital low-pass filter to form the final sequence. A two pole Butterworth low-pass filter, approximated

Table 2. Sinusoidal input information.

counts/cycle	frequency (Hz)	amplitude (inches)	amplitude (counts)	acceleration (in/sec-sec)	acceleration (g)
32	1.11607	2.0000	1626	98.35	0.25
16	2.23214	0.9822	799	193.20	0.50
8	4.46286	0.2455	200	193.20	0.50
4	8.92857	0.1228	100	386.40	1.00

by Tustin's (bilinear transform) method, was used with a natural frequency of 4.22 Hz and variable gain. Two random input sequences were constructed. The first, using a gain of 50, is referred to as the low amplitude input, and the second, using a gain of 100, is referred to as the high amplitude input.

3.3 SYSTEM IDENTIFICATION

The general goal of system identification is to determine a model, or parameters of a model, for a system based on the input/output characteristics such as the frequency response function, $H(j\omega)$, of the system.

For the system considered in this thesis, $H(j\omega)$ is experimentally determined and displayed in graphical form.

The technique of using estimated spectral densities to calculate the frequency response of a system is based on linear system theory. The laboratory system was assumed to be approximately linear when responding to band-limited inputs of low amplitude. The two major sources of nonlinear effects were geometrical variations and the nonlinearities in the drive train. The effect of geometrical variations was observed by testing the robot in 4 distinct positions. These positions spanned the range of the expected workspace. Also, the tests were performed for each tool coordinate axis. The effect of the drive train dynamics was observed by testing the robot with inputs of different amplitude.

The linearity of the system for each random input was estimated by calculating the coherence function, defined in Section 3.3.2. This function is a direct measure of the degree to which the output is linearly dependent on the input, and it is independent of the system being identified. The value of the coherence function falls in the range [0, 1], where a value of 1 indicates a perfect linear relationship. There are two causes of a value less then 1: measurement noise and nonlinear plant characteristics. For the experiments presented in this section, the coherence was greater than 0.9 in the frequency range of 1 to 10 Hz.

The frequency response was also calculated at discrete frequencies using sinusoidal inputs. The method, which is further explained below, is to decompose the output signal into an infinite series of sinusoidal components. Then the response for the input frequency is determined. It is not necessary for the plant to be linear to use this method. These results are shown as crosses on the frequency response plots for comparison with the responses obtained from estimating spectral densities.

The input/output signals for the plant are defined as:

- u is the input displacement signal sent by the IBM PC-AT to VAL-II,
- y is the output displacement signal,
- w is measurement noise uncorrelated with the input u,
- z is the measured output displacement ($z = y + w$).

Note that in the laboratory, acceleration was measured, not displacement. The conversion from acceleration to displacement is made in the frequency domain, as explained below.

3.3.1 Frequency Response Estimation Using Sinusoidal Inputs

If $f(t)$ is a continuous function on the interval $0 < t < p$, it may be represented as a Fourier series expansion, given by

$$f(t) = A_0 + \sum_{m=1}^{\infty} [A_m \cos(2m\pi t/p) + B_m \sin(2m\pi t/p)], \qquad (2)$$

where

$$A_0 = 1/p \int_0^p f(t)\ dt$$

$$A_m = 2/p \int_0^p f(t) \cos(2m\pi t/p)\ dt$$

$$B_m = 2/p \int_0^p f(t) \sin(2m\pi t/p)\ dt.$$

If $f(t)$ is given by a finite set of N data points, then a zero order approximation can be written for the integrals. Assume that the sample points are equally spaced a distance T apart, $0 \leq t < NT$. Defining

$$\omega_m = 2\pi m/NT \qquad m = 0, 1, 2, \ldots N-1 \qquad (3)$$

for $\omega_m < \omega_s$ (sampling rate), the integrals are approximated by:

$$A_0 = 1/N \sum_{n=0}^{N-1} f(nt) \tag{4}$$

$$A_m = 2/N \sum_{n=0}^{N-1} f(nt) \cos(2\pi mn/N)$$

$$B = 2/N \sum_{n=0}^{N-1} f(nt) \sin(2\pi mn/N) .$$

Consider the Fourier Transform of a function f(t), defined by

$$F(j\omega) = \int_{-\infty}^{\infty} f(t) e^{-j\omega t} \, dt \tag{5}$$

where $j = (-1)^{1/2}$. A zero-order approximation of the integral is

$$F(m) \simeq T \sum_{n=-\infty}^{\infty} f(nT) e^{-2\pi mn/N} = (T) DFT(m) \tag{6}$$

For N data points the Discrete Fourier Transform (DFT) can be written as

$$DFT(m) = \sum_{n=0}^{N-1} f(nT) \cos(2\pi mn/N) - j \sum_{n=0}^{N-1} f(nT) \sin(2\pi mn/N) . \tag{7}$$

Defining $R_{DFT}(m)$ = real part of DFT(m) and $I_{DFT}(m)$ = imaginary part of DFT(m) equation (7) can be written as

$$DFT(m) = R_{DFT}(m) - jI_{DFT}(m). \tag{8}$$

In this form the DFT can be used to calculate the coefficients of the Fourier series expansion of a signal given by $f(nT)$. The coefficients are given by

$$A_m = (2/N) R_{DFT}(m), \tag{9}$$

$$B_m = (2/N) I_{DFT}(m),$$

where

$m = 0, 1, 2, \ldots N-1$

($A_m = 0$ when $E[y(nT)] = 0$).

In the laboratory, a single input frequency was used with units of displacement. The output sequence $z(nT)$ was obtained by measuring and sampling the output acceleration. The procedure for determining the magnitude and phase response is as follows:

1. Sample output $z(nT)$ in units of (g),
2. Compute and remove the mean ($z(nT) = z(nT) - \text{mean}$),
3. Convert $z(nT)$ to units of in/sec^2,
4. Take the FFT of $z(nT)$ to yield $Z(m)$,
5. Multiply $Z(m)$ by $-(2/N\omega_m^2)$ to yield the series coefficients for the displacement spectrum,
6. Convert to magnitude/phase form.

3.3.2 Frequency Response Estimation Using Random Inputs.

Consider a linear, time-invariant system with the frequency response $H(j\omega)$, input u, and output y. A property of the system is that

$$H(j\omega) = \frac{S_{uy}(j\omega)}{S_{uu}(j\omega)} \tag{10}$$

where $S_{uy}(j\omega)$ and $S_{uu}(j\omega)$ are the cross-spectral and auto-spectral densities of the input and output. These functions are defined by

$$S_{uy}(j\omega) = \int_{-\infty}^{\infty} R_{uy}(t)\, e^{-j\omega t}\, dt \tag{11}$$

and

$$S_{uu}(j\omega) = \int_{-\infty}^{\infty} R_{uu}(t)\, e^{-j\omega t}\, dt \tag{12}$$

where $R_{uy}(t)$ is the cross-correlation function of the input and output and $R_{uu}(t)$ is the auto-correlation function of the input.

Another property of a linear system is that the output spectral density is

$$S_{yy}(j\omega) = |H(j\omega)|^2 \, S_{uu}(j\omega) . \tag{13}$$

If only a noisy measurement of the output is available, then

$$z(t) = y(t) + w(t) \tag{14}$$

where $w(t)$ is noise uncorrelated with the system input $u(t)$. It follows that

$$S_{zz}(j\omega) = S_{yy}(j\omega) + S_{ww}(j\omega) . \tag{15}$$

The coherence function is defined to be

$$C_{uz}(j\omega) = \frac{|S_{uz}(j\omega)|^2}{S_{uu}(j\omega) \, S_{zz}(j\omega)} \tag{16}$$

where $0 \leq C_{uz}(j\omega) \leq 1$.

Since the input and output are measured and sampled for a finite time, the spectral densities must be estimated. In practice, reliable estimates are difficult to obtain from finite data records. Zero-order approximations of equations (11) and (12) are not reliable. The next section discusses the estimation technique used in this research. Let Φ

be an estimate of a spectral density S, then the goal is to estimate the quantities

$$H(j\omega_m) \simeq \frac{\Phi_{uz}(m)}{\Phi_{uu}(m)} \tag{17}$$

and

$$C_{uz}(j\omega_m) \simeq \frac{|\Phi_{uz}(m)|^2}{\Phi_{uu}(m)\Phi_{zz}(m)} \tag{18}$$

where

$$\omega_m = 2\pi m/NT \qquad m = 0, 1, \ldots, N-1.$$

3.3.3 Estimation of Spectral Densities

The method of averaging periodograms to estimate spectral densities is discussed by Welch[20]. Let $X(n)$, $n = 0, 1, \ldots, N-1$ be a sample from a stationary, second-order stochastic sequence. Assume that $E(X) = 0$. Let $X(n)$ have a spectral density $S_{xx}(j\omega)$. Take segments, possibly overlapping, of length L with the starting points of these segments D

units apart. Let X_1, n=0, 1, . . ., L-1 be the first such segment. Then

$$X_1(n) = X(n) \qquad n=0, 1, \ldots, L-1. \tag{19}$$

Similarly,

$$X_2(n) = X(n + D) \qquad n=0, 1, \ldots, L-1$$

and finally

$$X_K(n) = X(n + (K - 1)D) \qquad n=0, 1, \ldots, L-1.$$

Thus, there are K such segments; $X_1(n)$, . . ., $X_K(n)$, and they cover the entire record ($(K - 1)D + L = N$).

The method of estimation is as follows. For each segment of length L, calculate a modified periodogram. That is, select a data window W(n), n=0, 1,. . ., L-1, and form the sequences $X_1(n)W(n)$, . . ., $X_K(n)W(n)$. Then take the finite Fourier transforms $F_1(m)$, . . ., $F_K(m)$ of these sequences. The transforms are given by

$$F_k(m) = 1/L \sum_{n=0}^{L-1} X_k(n) W(n) e^{-j2\pi mn/L}. \tag{20}$$

The K modified periodograms are given by

$$I_k(f_m) = L/U \, |F_k(m)|^2 \qquad k = 1, 2, \ldots, K, \tag{21}$$

where

$$f_m = m/L \qquad n = 0, \ldots, L/2$$

and

$$U = 1/L \sum_{n=0}^{L-1} W^2(n) .$$

The spectral estimate, $\Phi_{xx}(m)$, is is obtained by averaging the periodograms

$$\Phi_{xx}(m) = 1/K \sum_{k=1}^{K} I_k(f_m) . \tag{22}$$

This procedure can be used to calculate the input and output autospectral densities, Φ_{uu} and Φ_{zz}. The calculation of the cross-spectral densities is done is a similar manner. Let $X(n)$, $n=0, \ldots, N-1$, and $Y(n)$, $n=0, \ldots, N-1$, be samples from two second-order stochastic sequences. Both samples are divided into K segments of length L. Call these segments $X_1(n), \ldots, X_K(n)$ and $Y_1(n), \ldots, Y_K(n)$. Modified cross periodograms are calculated for each pair of segments $X_k(n)$, $Y_k(n)$, and the average of these modified cross periodograms constitutes the estimate Φ_{XY}. This procedure was applied to estimate the cross-

spectral density Φ_{uz}. For this research, a 50% overlap of the data segments is used along with a Hamming window. The formula for a Hamming window is

$$W(n) = 0.54 - 0.46 \cos[2\pi n/N] \qquad n = 0, 1, \ldots, N-1. \tag{23}$$

The procedure for calculating the frequency response function from the input u(nT) and the output z(nT) is summarized as follows:

1. Sample output z(nT) in units of (g),
2. Convert z(nT) to units of in/sec^2,
3. Compute the cross-spectral and auto-spectral densities, (Segment means are removed before windowing and transforming to avoid low frequency distortion.)
4. Calculate the estimate of $H(j\omega)$ in magnitude/phase form,
5. Calculate the estimate of C_{uz},
6. Multiply each component of $H(j\omega)$ by $-1/\omega^2$ to convert to output displacement over input displacement.

3.4 EXPERIMENTAL RESULTS

Typical frequency response and coherence functions are shown in Figure 10 and Figure 11 (note that on this plot and the others that the phase was reset to 0 by the transfer function estimation program after -360 deg). There is a strong correlation between the results of the sinusoidal tests (shown by crosses) and the random input tests. The plot shows valid results between 0.6 and 10 Hz. Outside of this range the spectral density of the input is low. Also, the output measurements above 10 Hz are noisy and the spectral estimation error is high. The coherence function shows that the linear approximation is good between 1 and 10 Hz.

The dominant characteristic of the frequency response up to 10 Hz is a phase shift. The phase shift is approximated well by a 0.1 sec time delay; a comparison between the sinusoidal data and this model is given in Table 3. Computation time is the major source of the time delay. VAL-II must calculate the appropriate joint servo motor commands to realize each displacement commanded by the IBM PC-AT supervisor. The plots show the attenuation of the magnitude response as frequency increases (see also data in Table 3). The most likely cause of attenuation in magnitude as frequency increases is servo driver saturation.

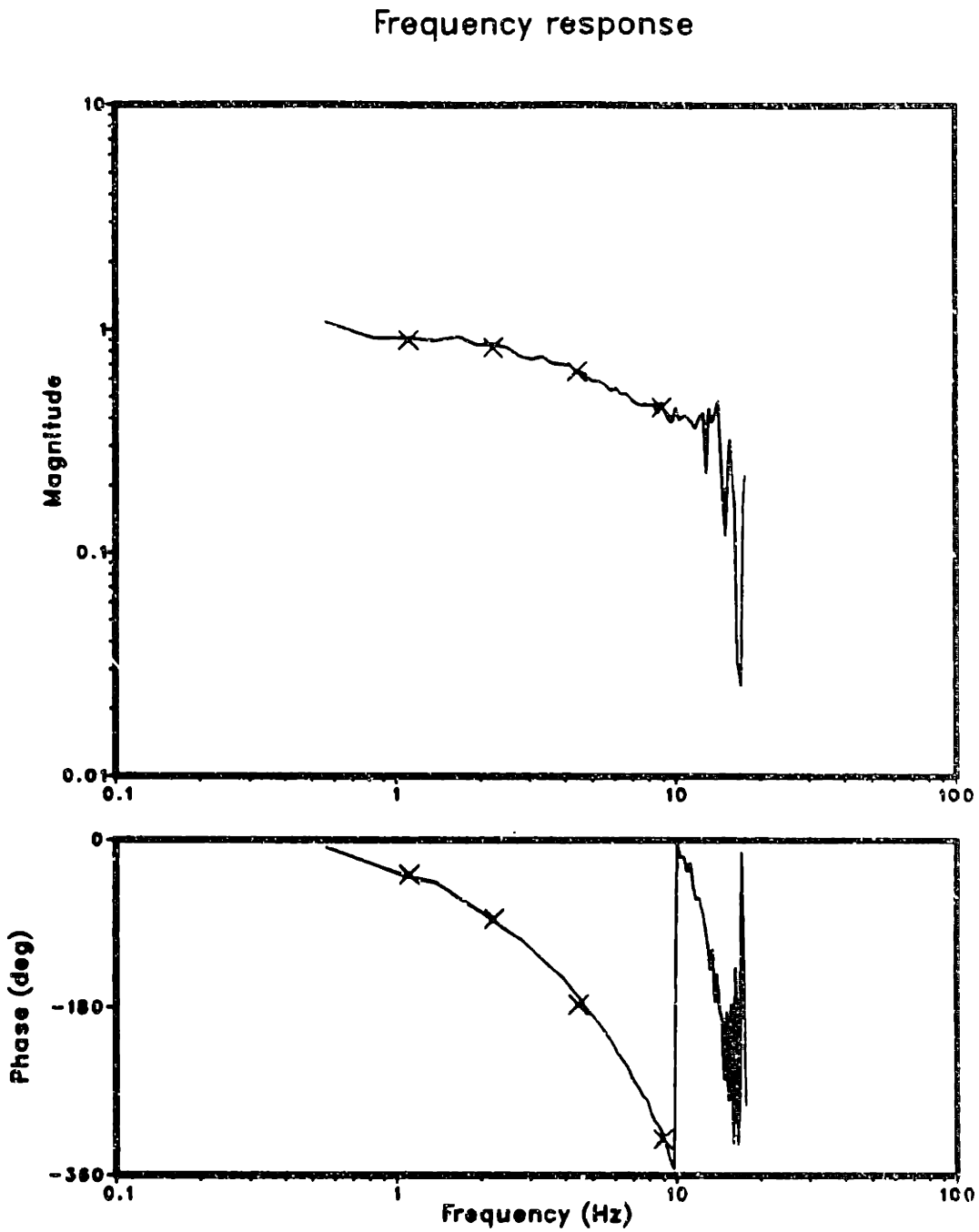

Figure 10. Frequency response of PUMA robot and VAL-II: Position 3, no payload, low amplitude input

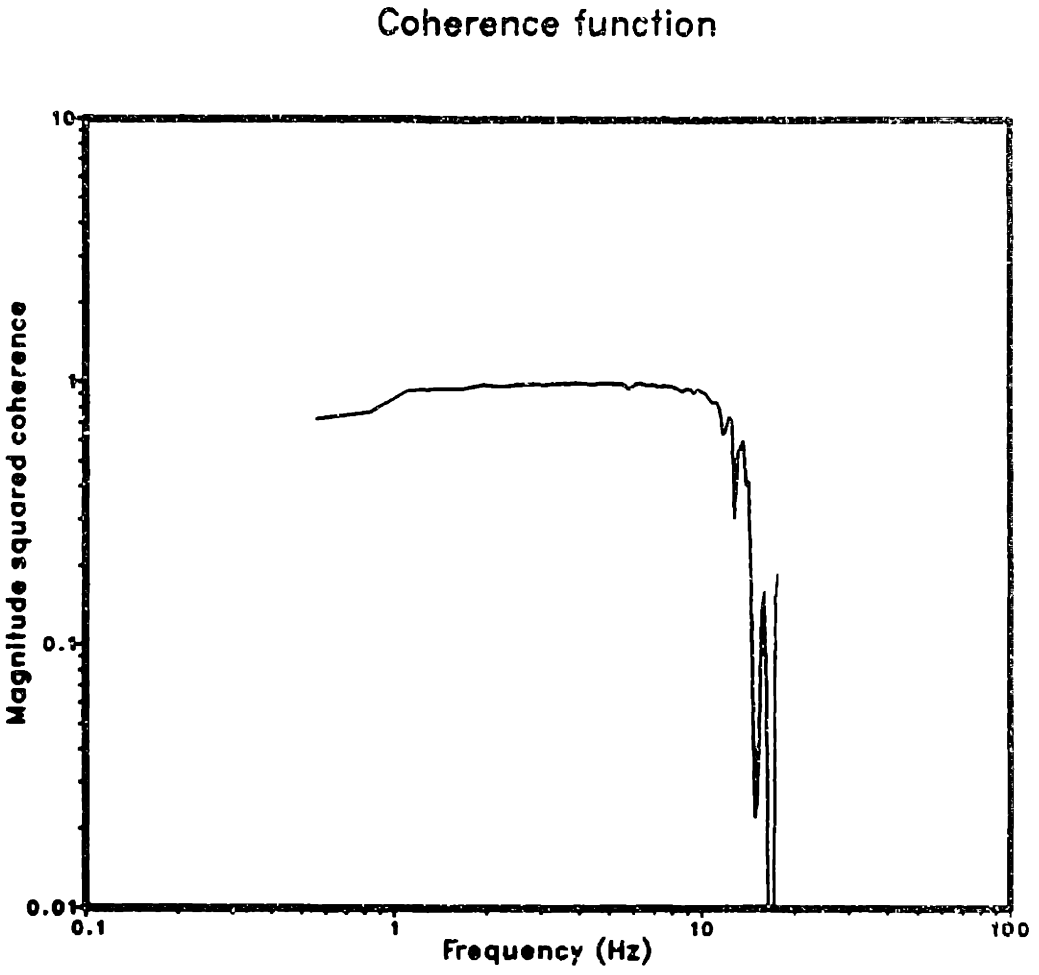

Figure 11. Coherence function of PUMA robot and VAL-II: Position 3, no payload, low amplitude input

Table 3. Sinusoidal test data

Test	Position	Motion axis	Accelerometer axis	Additional payload (kg)
1	3	z	z	-
2	3	z	z	1.152
3	3	z	z	1.957
4	1	z	z	-
5	4	z	z	-
6	2	z	z	-
7	3	y	y	-
8	3	z	y	1.152

magnitude(displacement/displacement) and phase(degrees)

Test	1.116 Hz		2.232 Hz		4.464 Hz		8.929 Hz	
	mag	phase	mag	phase	mag	phase	mag	phase
1	0.90	-37.1	0.83	-84.7	0.65	-177.0	0.45	-321.2
2	0.92	-36.8	0.86	-84.8	0.68	-176.6	0.50	-321.5
3	0.94	-37.4	0.87	-85.3	0.70	-177.2	0.54	-323.3
4	0.88	-37.3	0.88	-85.1	0.68	-175.2	0.46	-316.5
5	0.90	-35.7	0.84	-84.5	0.64	-175.2	not available	
6	0.87	-36.9	0.80	-85.7	0.61	-178.1	0.42	-318.4
7	0.95	-35.9	0.83	-84.1	0.56	-170.7	not available	
8	0.08	-203.1	0.06	-235.4	0.05	-307.1	not available	
*1	1.00	-40.2	1.00	-80.4	1.00	-160.7	1.00	-321.4
*2	1.00	-45.0	1.00	-90.0	1.00	-180.0	1.00	-360.0

*1 is a 0.1 s time delay model.
*2 is a 0.112 s (4 counts) time delay model.

Figure 12 shows the frequency response function in Figure 10 compared with three others. Plot A is the same as in Figure 10. Plot B shows the same test with the high amplitude random input. In plot C, a 1.152 kg payload is added and in plot D a 1.957 kg payload is added.

There is no significant difference in the frequency responses shown in this figure. The characteristics of the frequency response are therefore independent of load up to 2.5 kg in position 3. In addition, no significant effect caused by drive train nonlinearities was observed when the input magnitude was changed.

Figure 13 shows frequency responses for the robot in four different positions. The position of the robot, within the workspace tested, has no significant effect on the frequency response.

Figure 14 shows frequency response functions for the accelerometer mounted in the y-direction. In the first set of plots (A), the robot moves in the y-direction. Again, there is no significant change in the response. In the second set of plots (B), the robot moves in the z-direction. This shows a typical cross-axis magnitude response of about five to ten percent. Correlation function (B) shows that the signal to noise ratio for the second case is low. Results are not given for robot motion in the x-direction because it was damaging to the robot. This is because joint 1, the major axis, had to supply most of the motion. The cross-axis coupling between the robot axes is weak for these positions and magnitude of disturbances.

In summary, the major characteristics of the frequency response function are largely independent of position, excitation direction, and

payload. The PUMA's inner servo loop, operating at 1000 Hz, is able to compensate for these changes in dynamics. More of a difference in the magnitude responses was expected. The dominant characteristic of all the responses is the linear phase shift. As shown in Table 3, the phase shift can be approximated as a 0.1 s time delay. However, the system was modeled as a 0.112 s (4 sample periods) time delay to simplify system analysis during the design stage.

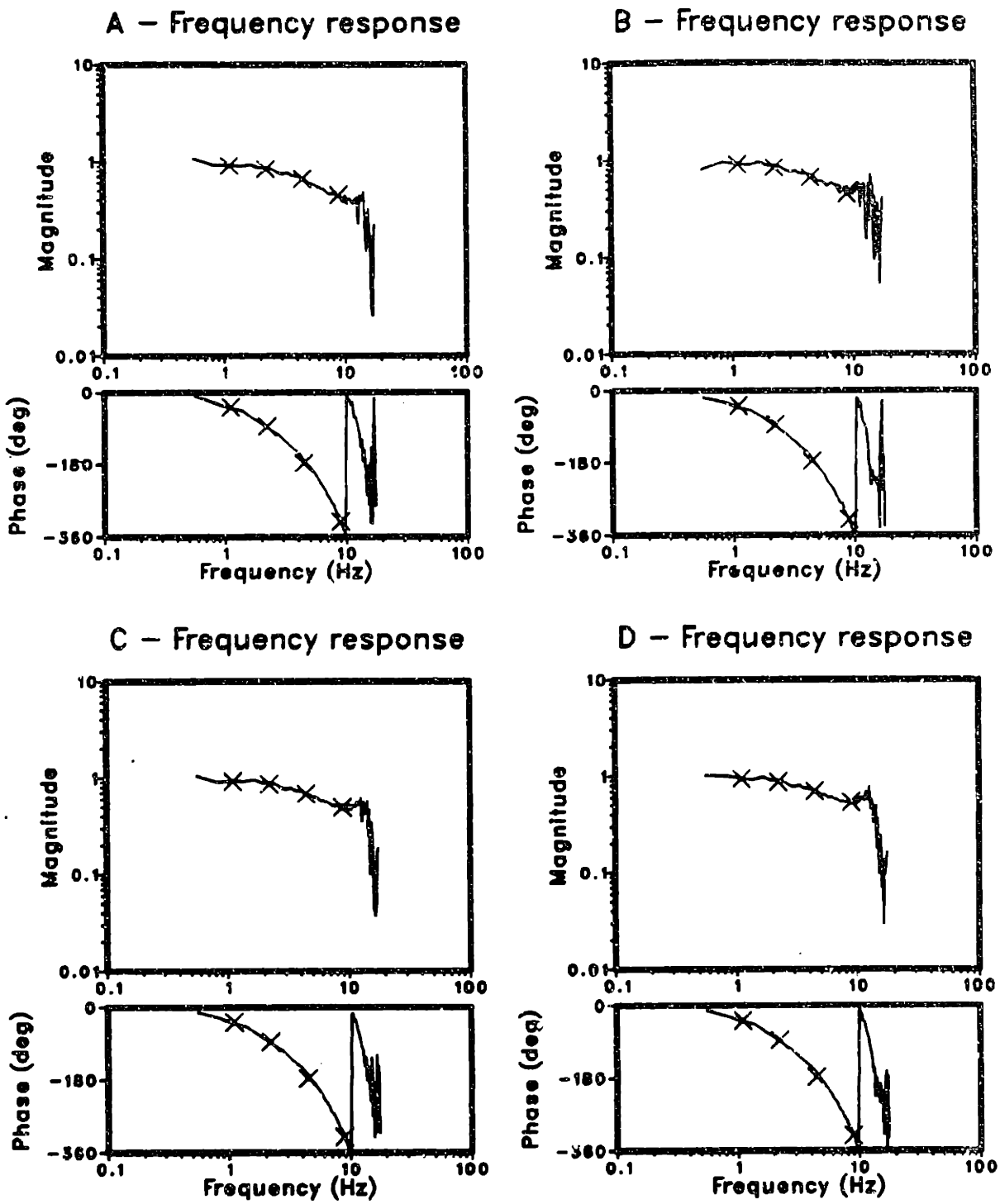

Figure 12. Frequency response comparison - position 3: Payload - (A,B - 0.0 kg. C - 1.152 kg. D - 1.957 kg.) Input - (A,C - low amplitude input B,D - high amplitude input)

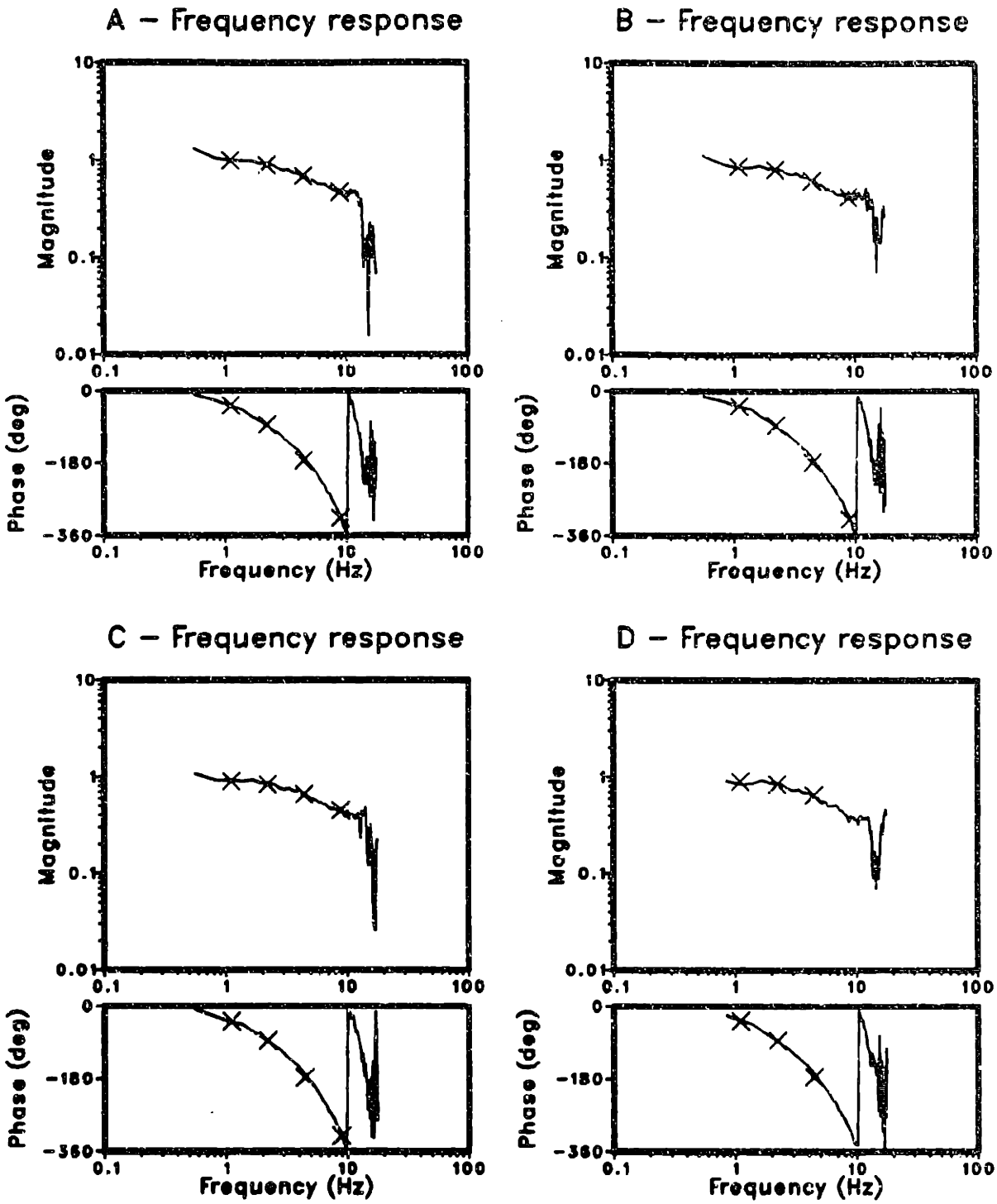

Figure 13. Frequency response comparison - no payload, low amplitude input: (A - position 1, B - position 2, C - position 3, D - position 4)

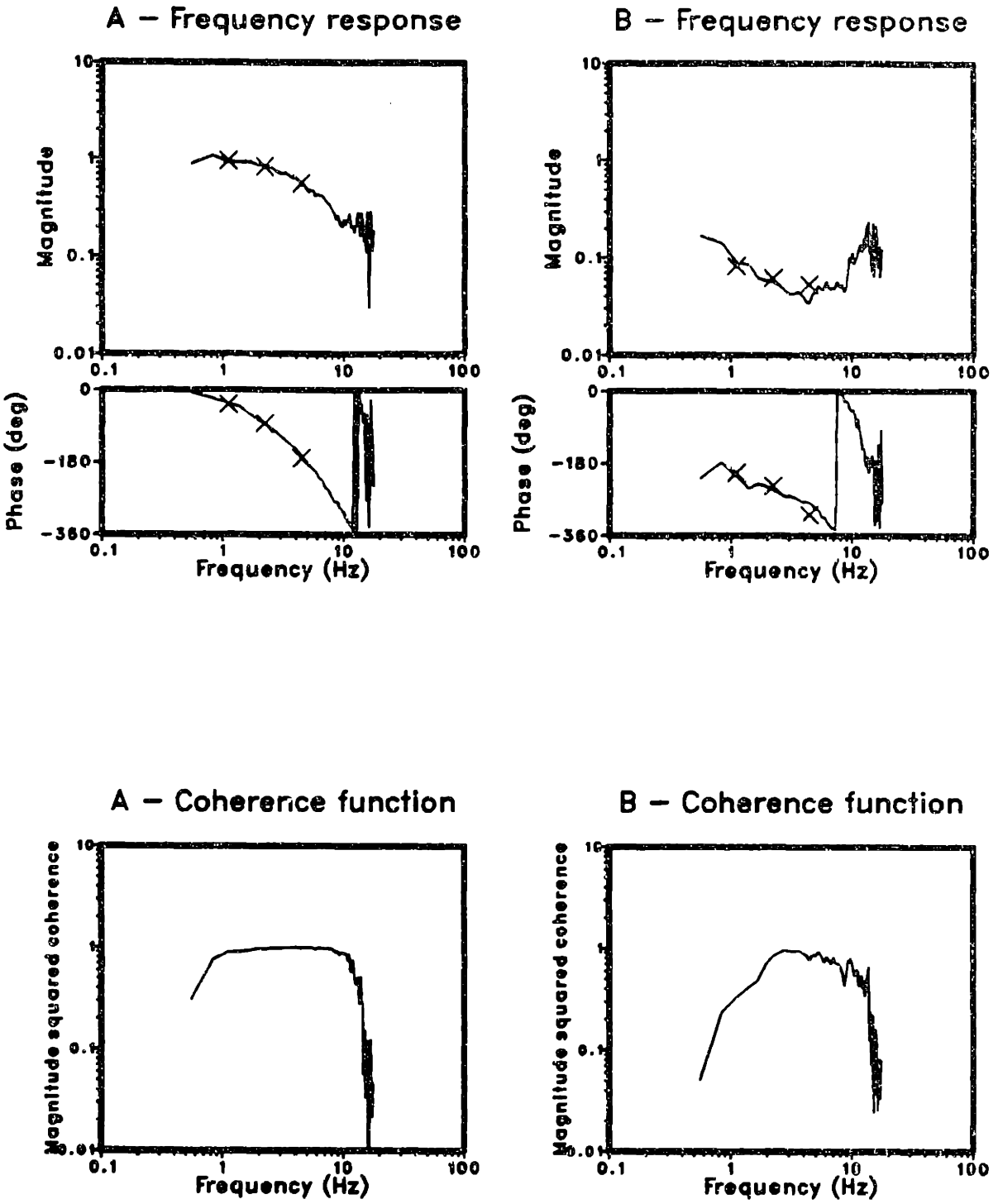

Figure 14. Frequency response compared with cross axis response - position 3: A - (motion y, acceleration y, 0.0 kg. payload) B - (motion z, acceleration y, 1.152 kg. payload)

4.0 FREQUENCY RESPONSE OF PUMA ROBOT IN CONTACT WITH THE WORKPIECE

In this experiment, the plant consisting of the PUMA robot and VAL-II was extended to include the grinding disk backing in contact with the workpiece. The frequency response relating the output force to input displacement for this plant was estimated. In this configuration, the force sensor and disk backing were mounted to the robot's end effector, and the robot was placed in contact with the workpiece as shown in Figure 15. The results are compared with those in Section 3 to determine the changes in dynamics caused by contact with the environment. A time delay remained a valid approximation of the frequency response.

As before, the method of averaging periodograms with a Hamming window was used to estimate the frequency response. In this case, the magnitude of the frequency response has units of stiffness (dN/mm). The random input sequence used in this section had a flat displacement spectrum. This is because a force sensor was used rather than an accelerometer. To protect the robot, the magnitude of this input sequence was smaller than that used in Section 3. The procedure for creating this input sequence is the same as described in Section 3.2 except that the low pass filter was not used.

The lower amplitude of the input sequence allowed the allowed the plant to be approximated as a linear spring in the frequency response analysis. The input commanded motion along the tool z-axis only.

The frequency response was estimated for three contact angles, 10, 21.5, and 30 degrees. Ivers[8] used 21.5 degrees during grinding experiments. Two different disk backings of different composition and form were tried. The grinding disk was not mounted on the backing during these experiments. For each experiment, the contact force was initialized and then the input was started. Initial contact forces were in a range of 250 to 2000 dN. The output from the force sensor was sampled every 0.028 s. This force sensor internally filters the force output in two stages. First, six analog strain gauge signals are filtered individually by a third-order lowpass filter, with the 3 dB point set at 120 Hz. Second, a second-order, programmable, digital filter rolls off the sampled signals at frequencies selectable from 240 Hz to 15 Hz. The digital filter cutoff set by the force sensor based on the effective output data rate.

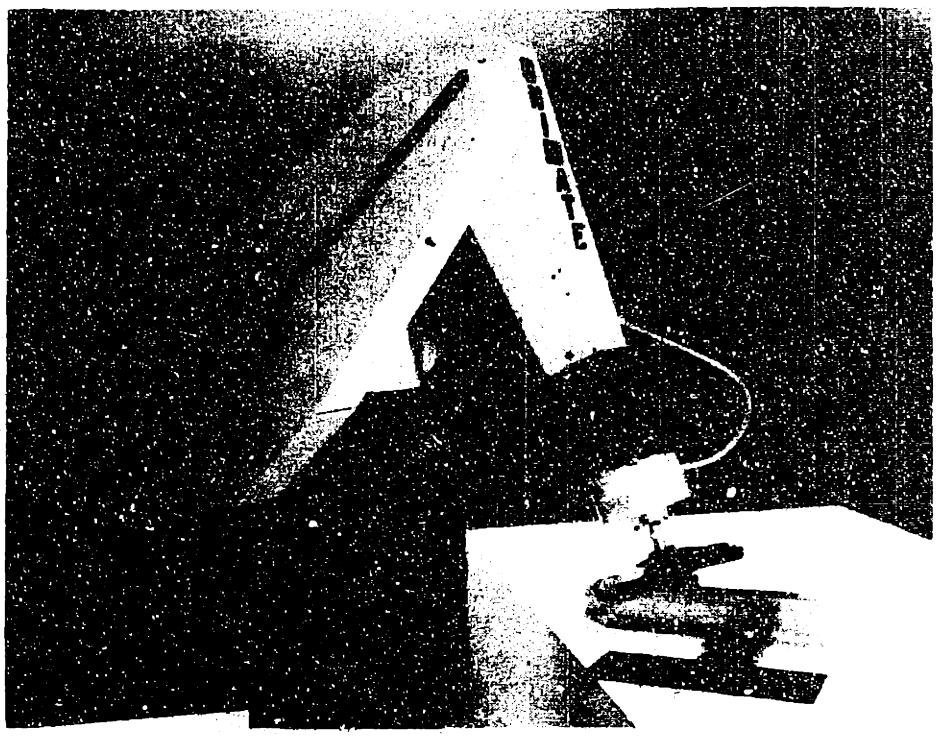

Figure 15. Configuration for experiments with workpiece contact

4.1 EXPERIMENTAL RESULTS

Typical results are shown in Figure 16 for disk #1 and Figure 17 for disk #2. The only significant difference in these responses is the overall height of the magnitude plot. This is due to differences in the initial contact force. There was no other initial parameter that made a significant difference.

The magnitude responses shown in the figures is constant to about 3 Hz and then the magnitude response decreases as frequency increases. This attenuation is faster than what is shown in the figures for the case without workpiece contact. This is not considered significant because most of the input signals to be used by the force controller are expected to have a bandwidth of less then 3 Hz. This is discussed in more detail in Section 6. The phase lag can be approximated by a 0.1 sec time delay within a bandwidth of 10 Hz. In this approximation the attenuation of the magnitude response is neglected.

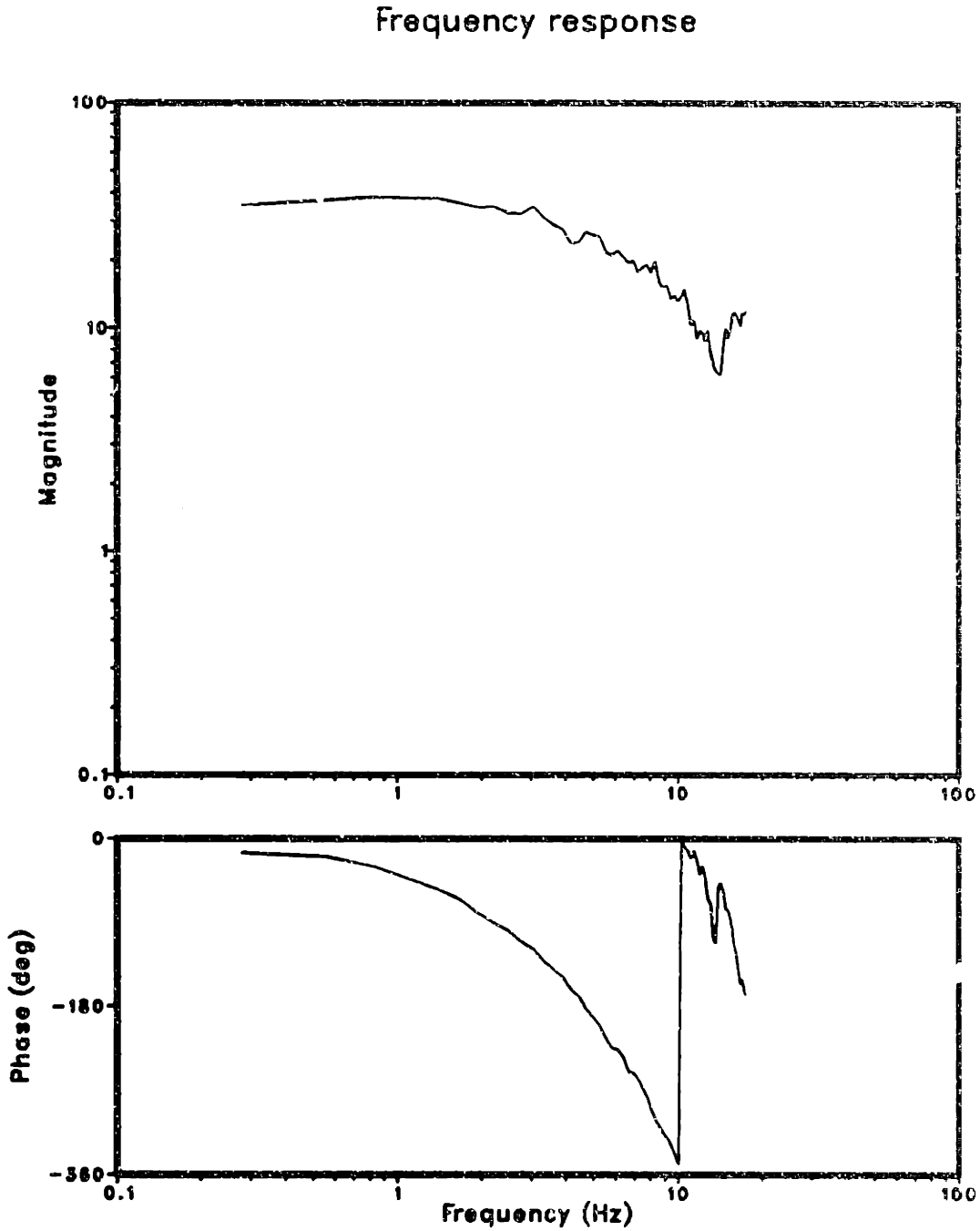

Figure 16. Frequency response of PUMA in contact with the workpiece - disk #1: (initial contact force 1100 dN)

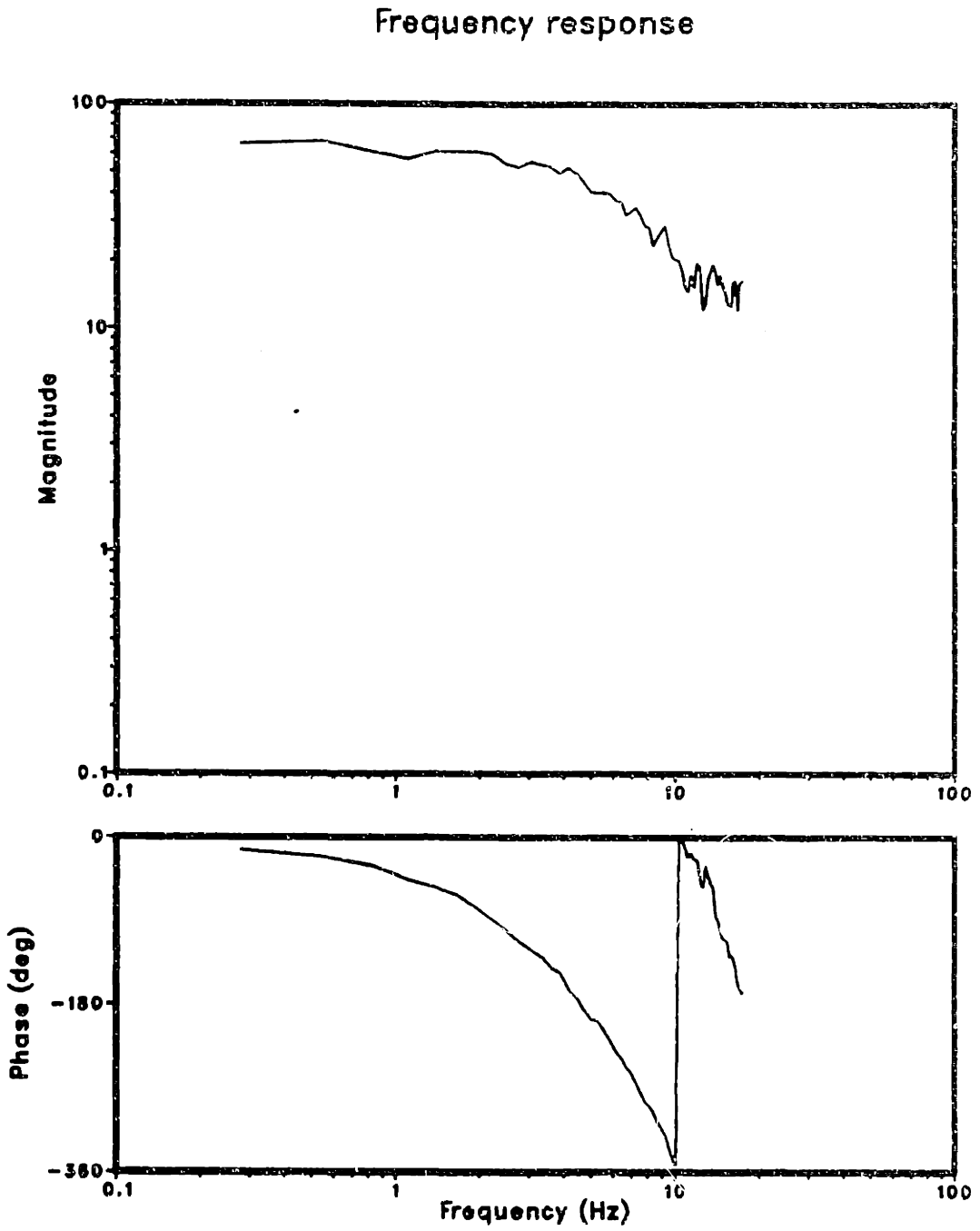

Figure 17. Frequency response of PUMA in contact with the workpiece - disk #2: (initial contact force 2470 dN)

5.0 COMPLIANCE MODEL OF PUMA ROBOT IN CONTACT WITH THE WORKPIECE

For this experiment, the PUMA was set up as described in Section 4 except that an 80 grit grinding disk was mounted to the rubber backing. This configuration was also used for the force control experiments, discussed in Section 6. The compliance of the plant, in this configuration, is experimentally determined. The grinding disk adds significant stiffness to the backing and must be when measuring the plant compliance. The contact angle was set to 21.5 degrees. This is one of the setups used by Ivers[8].

The robot was initially positioned so that the grinding disk just touches the workpiece. A low frequency sinusoidal sequence was used as the input, and is given by

$$u(kT) = A[1 - \cos(2\pi fkT)] \tag{24}$$

where

$A = \{50, 100, 150, 200\}$
$f = 0.13951$ Hz
$k = 0, 1, 2, \ldots, 1023$
$T = 0.028$ s.

The input sequence commanded the robot in the tool z-direction and the force output was recorded. Ordered pairs of {displacement(k), force(k+4)} were formed. The force was offset to compensate for the 0.1 s time delay, which is approximately 4 time steps. The ordered pairs were divided into two final sets; in the first set the displacement is sequentially increasing, and in the second it is decreasing. The robot pushes harder as the displacement increases, and pulls away as it decreases.

Figure 18 and Figure 19 show the results. Each figure has 4 experimental plots and 1 plot of the model (in bold print). Note that the stiffness of the disk appears to increase more quickly for the lower amplitude tests. This effect is not understood. The case of A = 200 can be approximated by

$$F(z) = b/a(e^{az} - 1), \quad z \geq 0, \tag{25}$$

where

F(z) = measured force
a = 0.011
b = 0.1 .

The stiffness P as a function of displacement is then given by

$$P(z) = \frac{df}{dz} = be^{az}. \tag{26}$$

Or, writing stiffness as a function of force yields

$$P(F) = aF + b. \tag{27}$$

In this model, compliance is a linear function of force. Clearly, $P(z)$ is a monotonic function. However, the following form is used during the nonlinear control law derivation for convenience:

$$P(q_2, q_1) = b/a(\exp(q_2) - \exp(q_1)), \quad q1, q2 \geq 0 \tag{28}$$

where $P(q_2, q_1)$ is the change in force that results when the displacement is changed from q_1 to q_2.

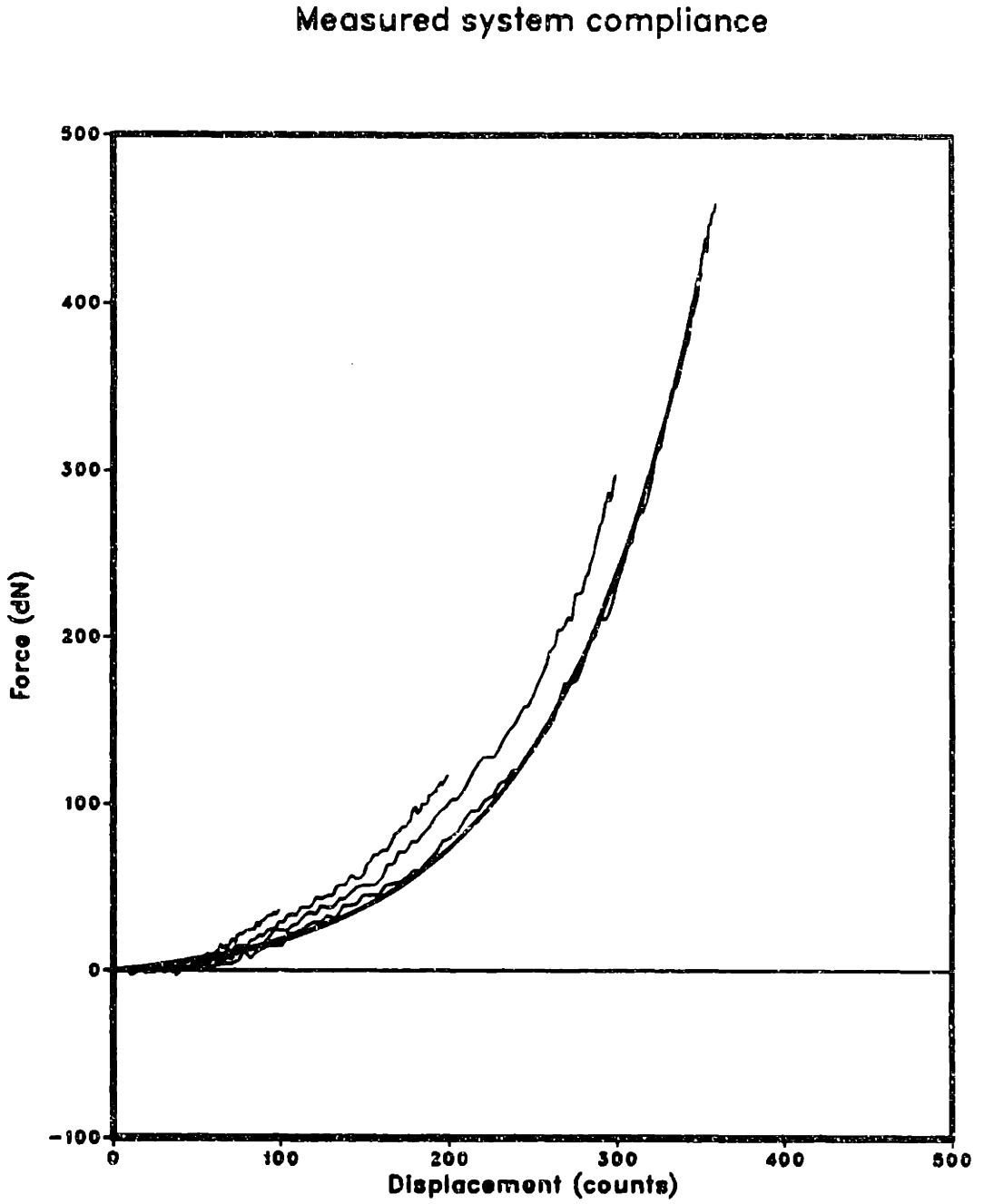

Figure 18. Measured compliance - displacement increasing: Model is in bold print, 1 count = 0.03125 mm (0.00123 in.)

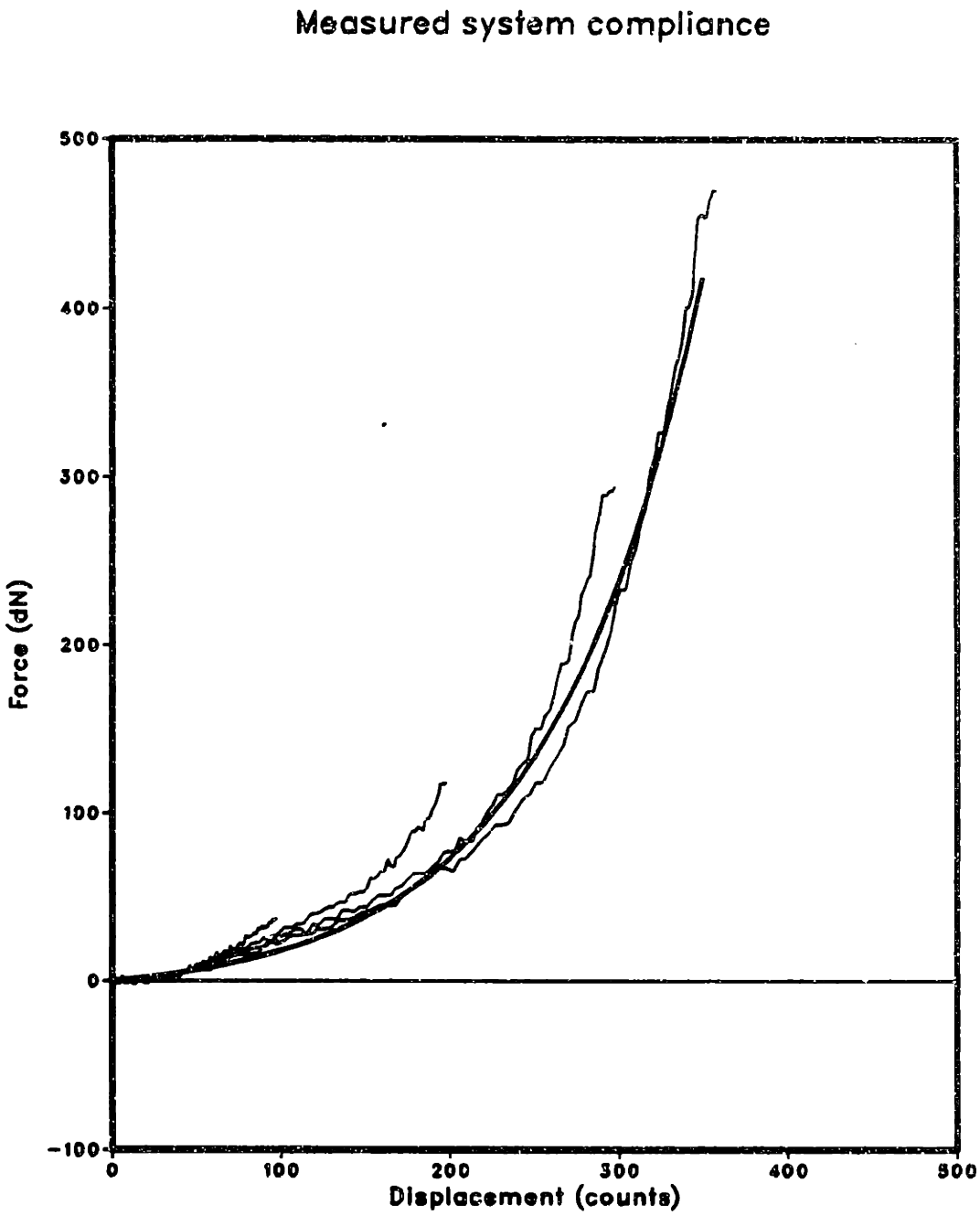

Figure 19. Measured compliance - displacement decreasing: Model is in bold print, 1 count = 0.03125 mm (0.00123 in.)

6.0 DESIGN OF A CLOSED LOOP FORCE CONTROL LAW

The objective of the research presented in this section was to design a force control law for the PUMA robot that would be usable in an automated grinding system. The force control law must by able to track a wide range of input signals, be stable at high forces, be robust to modeling errors, and be able to reject positional disturbances.

To meet this objective, the characteristics of the PUMA robot in contact with the workpiece were integrated into a unified model. This model consists of a time delay followed by a compliance. A number of different force control laws were designed and tested. The properties and limitations of each closed loop system are illustrated by simulations or experiments. The best overall performance was achieved using a nonlinear control law. This control law is presented in a general form.

6.1 DESCRIPTION OF FORCE CONTROL EXPERIMENTS

The experimental set up is shown in Figure 15. In this configuration, the Astek force sensor, grinding disk, and backing were mounted to the robot's end effector.

A nominal trajectory for the robot was specified. In these experiments, the contour traced by the edge of the contact patch as the robot follows the nominal trajectory corresponds to the nominal contour of the weld. The speed of the robot along the nominal contour in these experiments was 0.889 cm/s. If the workpiece was positioned without error, then the edge of the contact patch moved directly along the actual contour of the weld. A positional disturbance resulted when the two contours did not coincide. Other specifications for the nominal trajectory are possible.

The objective of the experiment was to track the desired force signal as the robot followed the actual contour of the workpiece. Thus, the control law must reject positional disturbances. The trajectories and contours discussed above are illustrated in Figure 21. A negative ramp disturbance resulted when the end of the weld was above PFINISH; this case is shown in Figure 22. A positive disturbance resulted when the end of the weld was below PFINISH. A complex disturbance is illus-

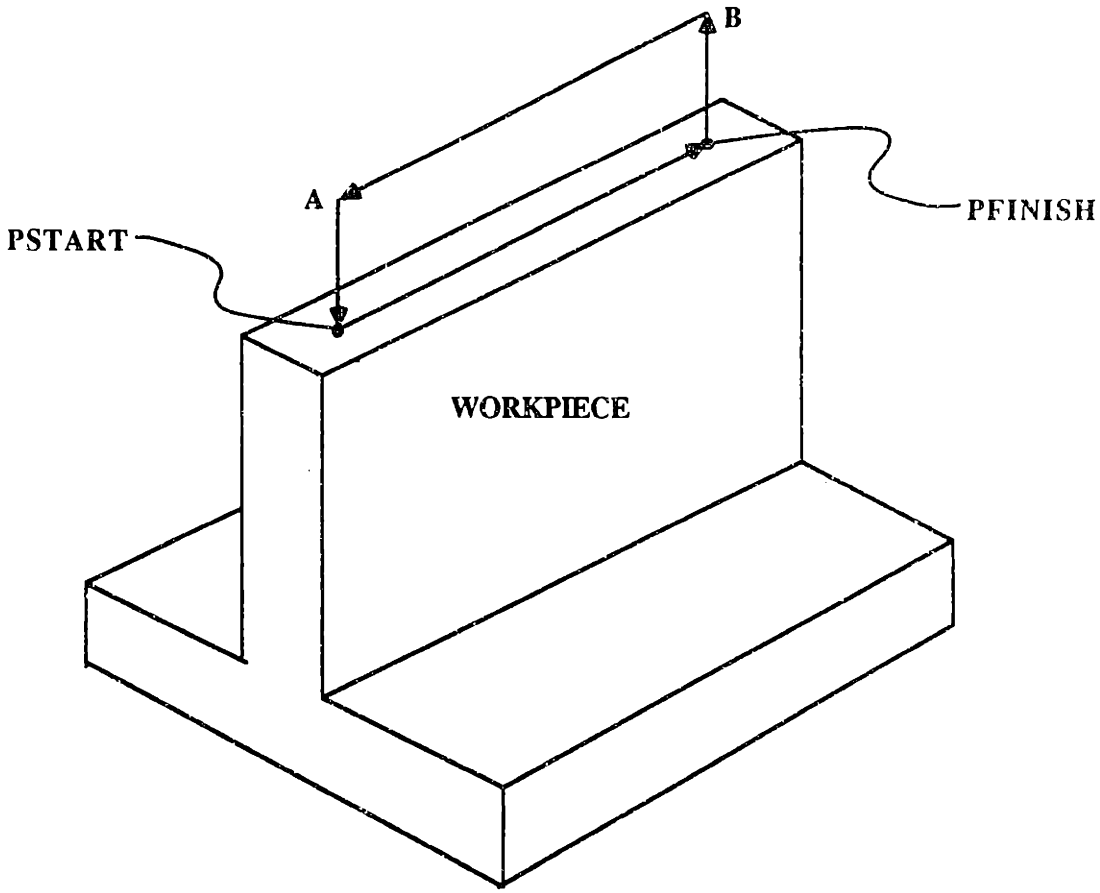

Figure 20. Motion sequence for force control experiments

trated in Figure 23. The workpiece shown in Figure 22 was 304.8 mm (1 ft.) long. The results for three rates of disturbance, given in Table 4, are discussed at the end of this section.

The robot was taught the location of four points, as illustrated in Figure 20. This was done by manually moving the robot to the desired position and orientation, then commanding VAL-II to record the joint

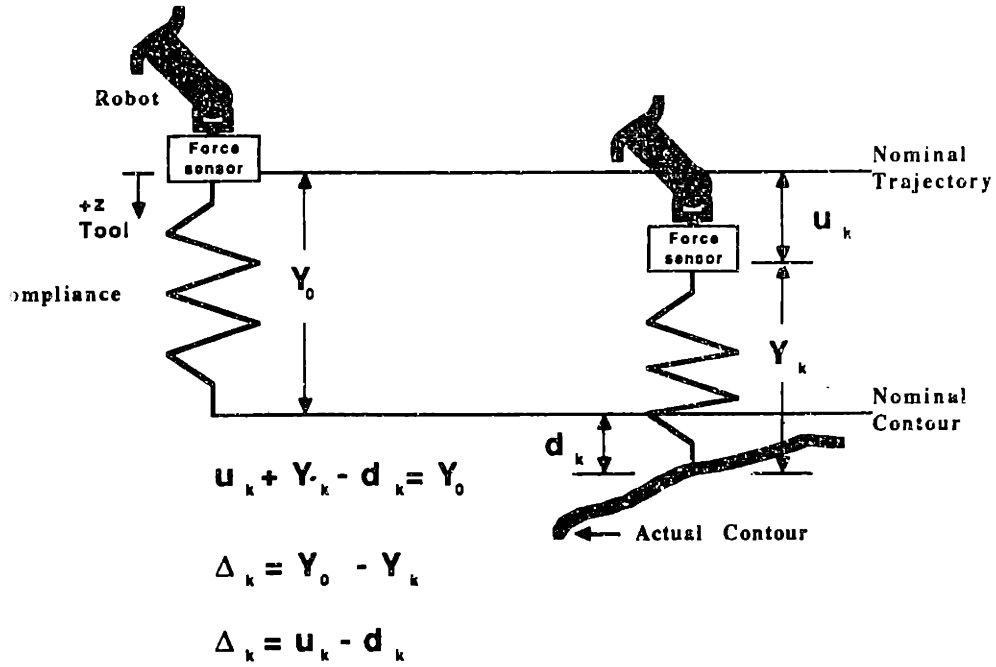

Figure 21. Illustration of contours and trajectories

encoder positions. Force was controlled between PSTART and PFINISH; this leg of the circuit was the system's nominal trajectory.

Each experiment began with the robot stationary at point A. The control parameters, control law, and input signal were selected The input was the desired force profile that the robot was to apply to the workpiece as a function of time. The force sensor was initially com-

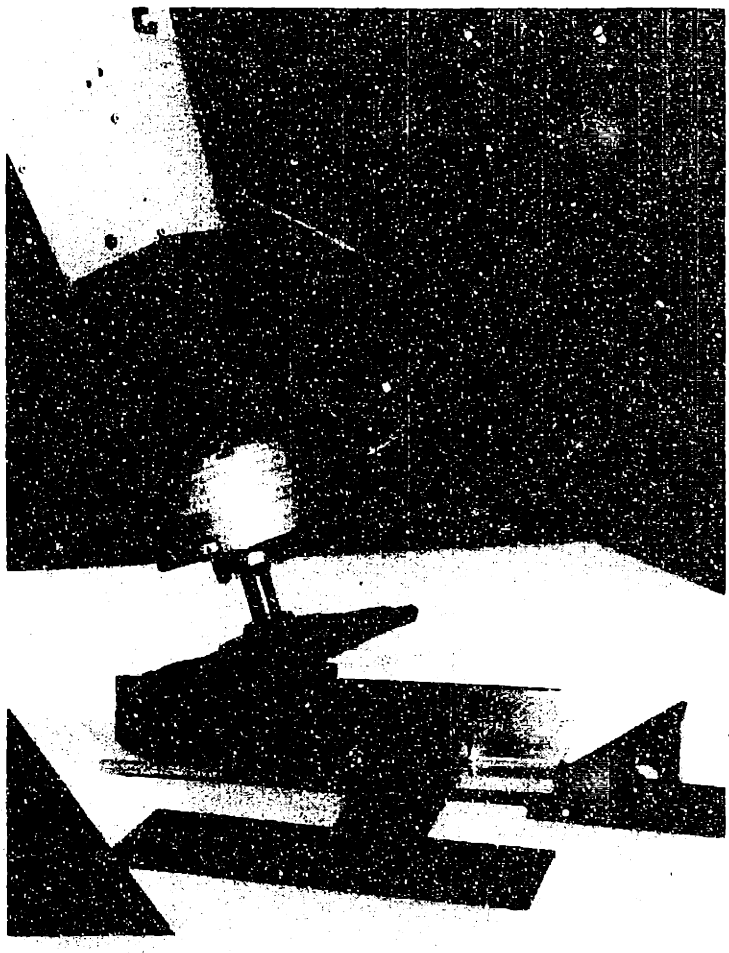

Figure 22. -5% ramp disturbance

Figure 23. Complex disturbance

Table 4. Ramp disturbances

ramp rate	angle of inclination	absolute height error at PFINISH
%	deg	mm
5	2.85	1.5
10	5.71	3.0
15	8.53	4.5

Nominal contour speed = 8.89 mm/s
Workpiece length = 304.8 mm

manded to set the measured output of all forces and moments to zero, eliminating gravitational effects during the experiment.

With the set up complete, a VAL-II program was started that commanded the robot to follow the counterclockwise circuit of straight line paths shown in Figure 20. This program was written in VAL-II's command language.

```
SPEED 20 ALWAYS          ;always move at 20% maximum speed
APPROS PSTART, 50        ;approach the point 50 mm from
                         ; PSTART (negative tool-z)
MOVES PSTART             ;move in a straight line to PSTART
BREAK                    ;wait until PSTART is reached
ALTER (0, 16)            ;interrupt the IBM PC-AT for path
                         ; modifications -
MOVES PFINISH            ; as robot is moving to PFINISH
NOALTER                  ;stop interrupts
DEPARTS 50               ;move 50 mm in negative tool-z
                         ; direction (away from workpiece)
APPROS PSTART, 50        ;go back to starting point and quit
```

When PSTART was reached, force control was activated by the ALTER command in the VAL-II program. This command instructed VAL-II to interrupt the IBM PC-AT every 28 ms for a trajectory modification. VAL-II adds this modification to the nominal trajectory to control the normal force. The control law in the IBM PC-AT determines the trajectory modification from the desired force and the feedback from the Astek force sensor.

6.2 INTEGRATED MODEL OF PUMA ROBOT IN CONTACT WITH THE WORKPIECE

The plant that was controlled consisted of the VAL-II controller, PUMA robot, grinding disk, and backing. The model discussed here describes the plant from the point of view of the controlling computer. This is a discrete time model, described by difference equations. The model describes the plant during contact with the workpiece.

The block diagram of the plant is shown in Figure 24. This figure shows the IBM PC-AT sending u_{k+4}, the commanded tool z-displacement, to the VAL-II controller. The resulting tool z-position of the grinding disk with respect to the nominal trajectory (in 4 sample periods) is u_k. The 4 sampling-period time delay is an approximation of the 0.1 s time delay that was proposed in Sections 3 and 4 as a model for the PUMA and

VAL-II. The displacement disturbance, d_k, is the difference between the actual workpiece contour and the nominal contour along the tool z-axis. The net deflection of the disk, from the undeformed position, is given by $\Delta_k = u_k - d_k$. The output force, y_k, is determined by the compliance function $P(\Delta_k, 0)$. Using the compliance model determined in Section 5, $P(\Delta_k, 0)$ is

$$y_k = P(\Delta_k, 0) = (b/a)(\exp(a\Delta_k) - 1) \quad \Delta_k \geq 0 \tag{29}$$

In this model of the plant, it is assumed that the robot can reach the commanded positions. It is also assumed that the robot can execute each commanded change in position within a single sampling period. The ability of the robot to overcome normal forces up to 2000 dN is verified in Section 4. The magnitude response is also discussed in Section 4, and it is shown to be approximately 1 for an input bandwidth up to 3 Hz. The magnitude response assumption was violated during tests with step inputs because it is impossible for a physical system to exactly follow a step. In these experiments, the maximum desired force was 400 dN. The desired force signals, r_k, were offset sinusoids and steps. All the inputs used in the force control experiments are summarized in Table 5.

Figure 25 shows a block diagram of the IBM PC-AT controlling computer. The inputs are r_k, the desired force signal, and y_k, the measured force output. The control law computations are represented by $G(z)$.

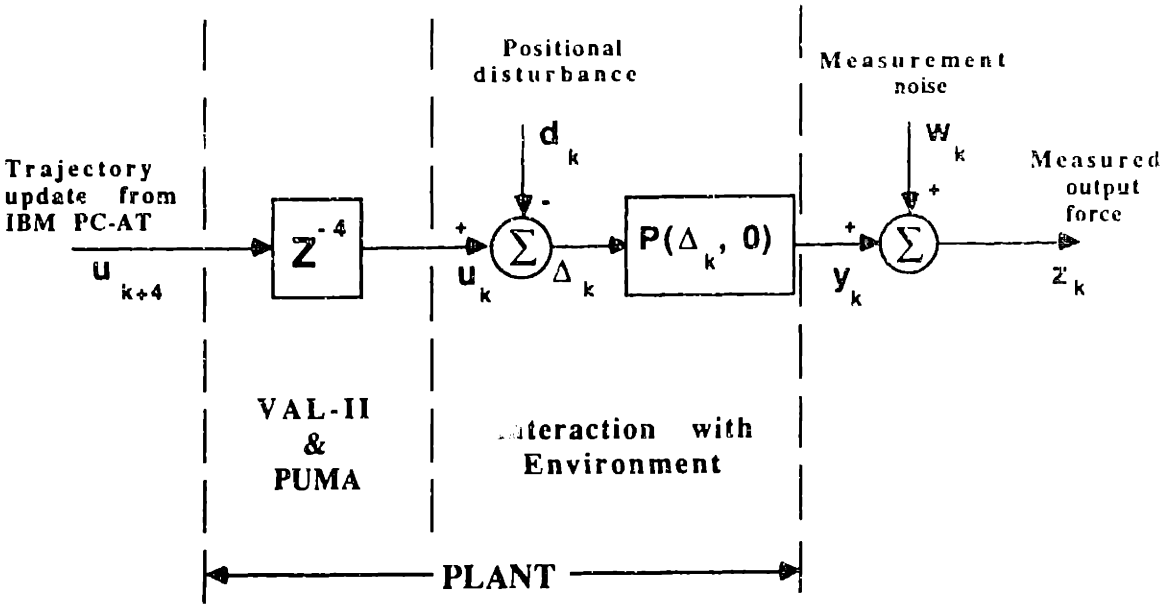

Figure 24. Block diagram of PUMA robot in contact with workpiece

Because of the nature of the VAL-II interface, the control signal, u_{k+5}, was always delayed one time period. Thus, the total time delay in the feedforward path was modeled as 5 sampling periods, or 0.14 s. From a state space point of view, the system description required 5 states, one for each period of delay. The compliance was modeled as a nonlinear gain and did not add a state to the model.

Table 5. Desired force input signals used in force control experiments

Sinusoids $\{r_k = A[1 - \cos(2\pi fkT)] + O_f\}$

nominal frequency Hz	exact frequency (f) Hz	spacial wavelength mm/cycle	Amplitude (A) dN	Offset (O_f) dN
0.14	0.13951	63.5	50	50
0.14	0.13951	63.5	100	100
0.14	0.13951	63.5	150	150
0.14	0.13951	63.5	200	200
0.14	0.13951	63.5	50	75
0.14	0.13951	63.5	50	125
0.20	0.27902	44.5	50	50
0.56	0.55804	15.9	50	50
1.12	1.11607	7.9	50	50
2.23	2.23214	4.0	50	50

(precision of input frequency necessary for symmetric data)

Steps

time of step s	location of step mm from PSTART	magnitude dN
0.000	0.0	0
0.000	0.0	25
3.584	31.9	25
3.584	31.9	50
3.584	31.9	75

T = 0.028 s, k = 0, 1, 2, 3, . . ., 1023
nominal contour speed = 8.89 mm/s
(All input profiles stored in integer format)

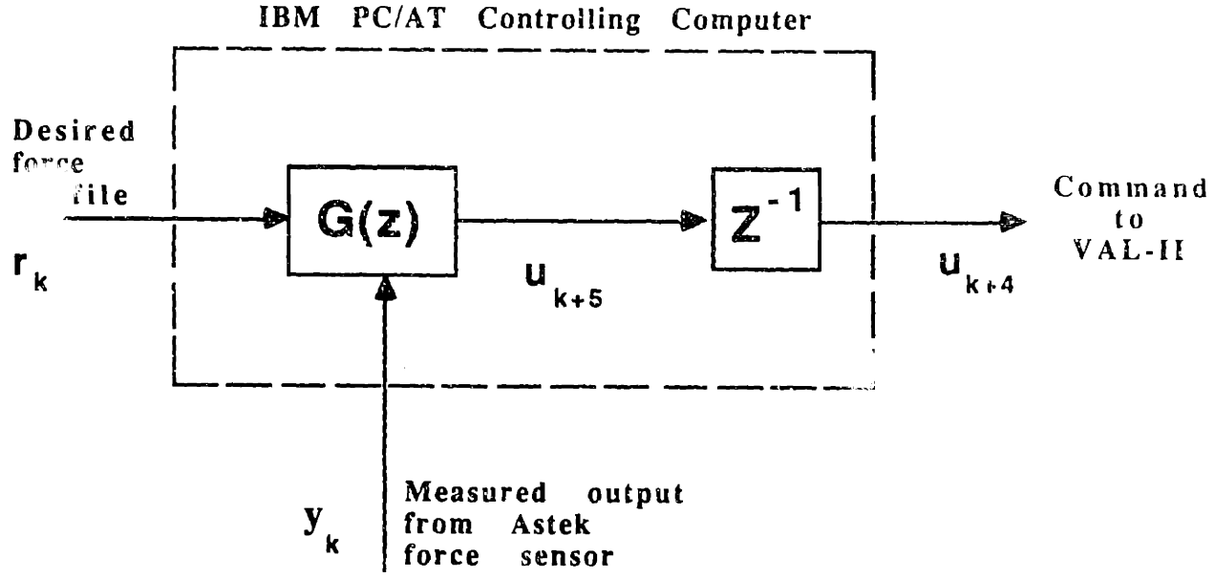

Figure 25. Block diagram of controlling computer

6.3 CONTROLLER BANDWIDTH CONSIDERATIONS

The required controller bandwidth is related to the contact patch size, the nominal contour speed, and the material removal rate. An approximate bound on the required bandwidth can be obtained as follows. The grinding disk contacts the workpiece over a finite contact patch. Each dimension of this contact patch is on the order of 10 mm. The

finite size of this contact patch leads directly to a finite limit in the wavelength of the contour that a grinder can grind into a weld. If L is the length of the contact patch, then the minimum wavelength that can be ground into a weld is greater than 2L. Therefore, a bound on the required bandwidth is 1/2L. For this system, L ≈ 10 mm, so the bandwidth of a contour ground into a weld is less than 0.5 cycles/cm. Assume the bandwidth of the desired force signal is of the same order of magnitude. Then, for a nominal contour speed of 8.89 mm/s, the maximum bandwidth of this signal is 0.56 Hz. The maximum input frequency used in these experiments, 2.23 Hz, would not be needed unless the nominal contour speed was at least 35 mm/s.

6.4 PROPORTIONAL - INTEGRAL CONTROL

As a starting point, consider proportional control of a linear compliance with a five step time delay. The closed loop system is shown in Figure 26. In this figure, K is the controller gain and P is a linear stiffness. Referring to the block diagram of the controlling computer, G(z) is

$$u_{k+5} = K(r_k - z_k). \tag{30}$$

Also, the closed loop transfer function is

$$\frac{Y(z)}{R(z)} = \frac{KP}{z^5 + KP}. \tag{31}$$

The total gain of the system (KP) is the product of the controller gain and the plant stiffness. From the characteristic equation, the stability criterion is

$$KP \leq 1 \tag{32}$$

assuming P is a constant linear compliance.

In addition to stability limitations, proportional control for a linear system always has a steady state error in response to a step input. This is easily shown using the final value theorem. For the laboratory system, P was nonlinear. The gain and stability of the system were therefore functions of the inputs, r_k and d_k.

Steady state errors to step inputs are eliminated by introducing an integrator into the control law. A block diagram of the system with Proportional-Integral (PI) control is shown in Figure 27.

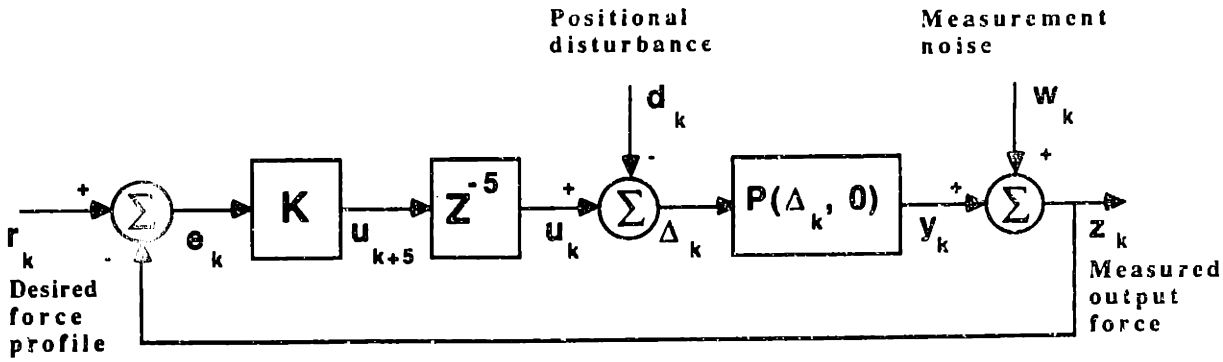

Figure 26. Block diagram of proportional control

The stability of the system now depends on KP and the integral time, T_1. The inverse of the integral time $1/T_1$ is called the reset rate. The reset rate is the number of times per sampling period that the proportional part of the control action is duplicated. When P is a linear compliance, the maximum KP as a function of integration time is shown in Figure 28. The closed loop system will be stable if the point defined by the parameters KP and T_1 falls below the curve. The closed loop characteristic equation for the plant with PI control is

$$1 + KP\left(\frac{(T_1 + 1)z - T_1}{T_1(z^{n+1} - z^n)} \right) = 0 \qquad (33)$$

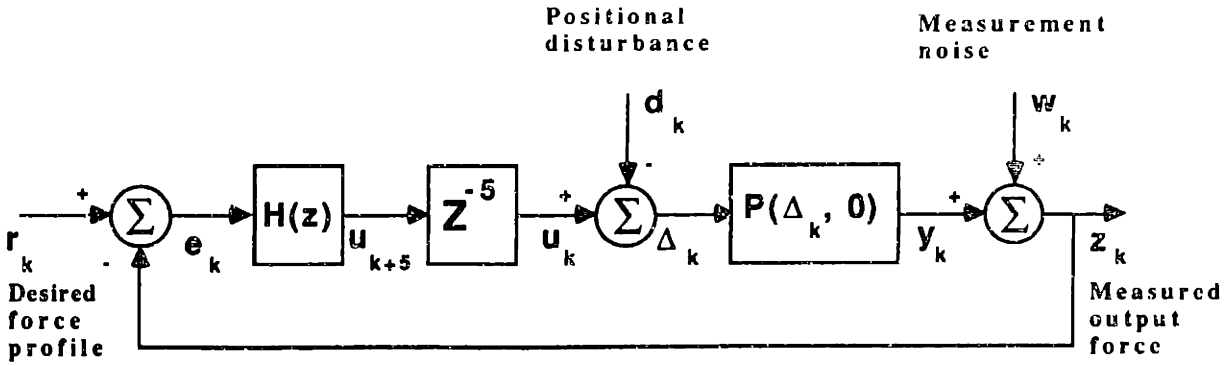

$$H(z) = K(1 + z/T_i (z - 1))$$

Figure 27. Block diagram of proportional - integral control

For $T_i = 20$, the stability criterion is

$$KP < 0.97$$

The characteristics of the linear system are useful for interpreting the responses of the nonlinear laboratory system. The response to a step in the reference input, r_k, is shown in Figure 29. The simulation used equation (29) as the nonlinear compliance model with the parameters listed. In the laboratory system, there was a small gap between the grinding disk and backing. This is why the experiment had a longer delay than the simulation. Both plots illustrate the sluggish response

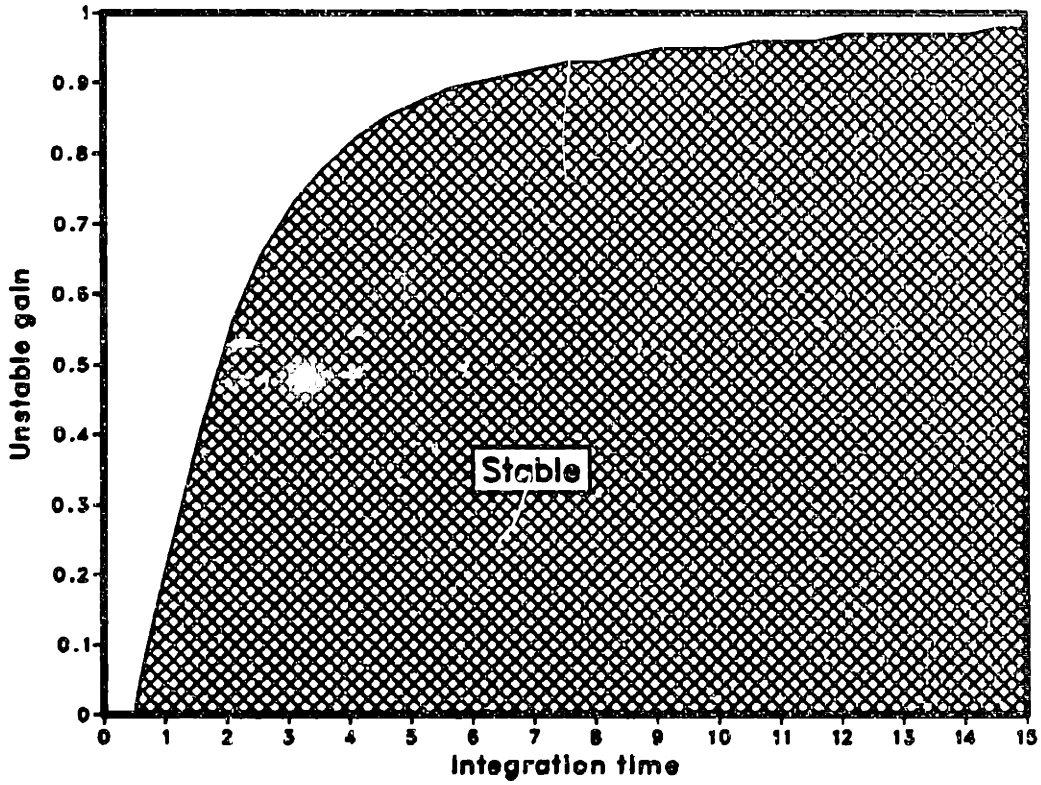

Figure 28. Stability of proportional - integral control

of a PI controller. Higher gains or lower integration times began to yield unacceptable oscillations in the steady state.

As with proportional control, the total gain depends on the controller gain and the plant stiffness. The plant stiffness increases linearly with force; this was discussed in Section 5. Thus, the effective closed loop gain, KP, increases with force. About any operating force, the nonlinear system can be approximated by a linear system. As force

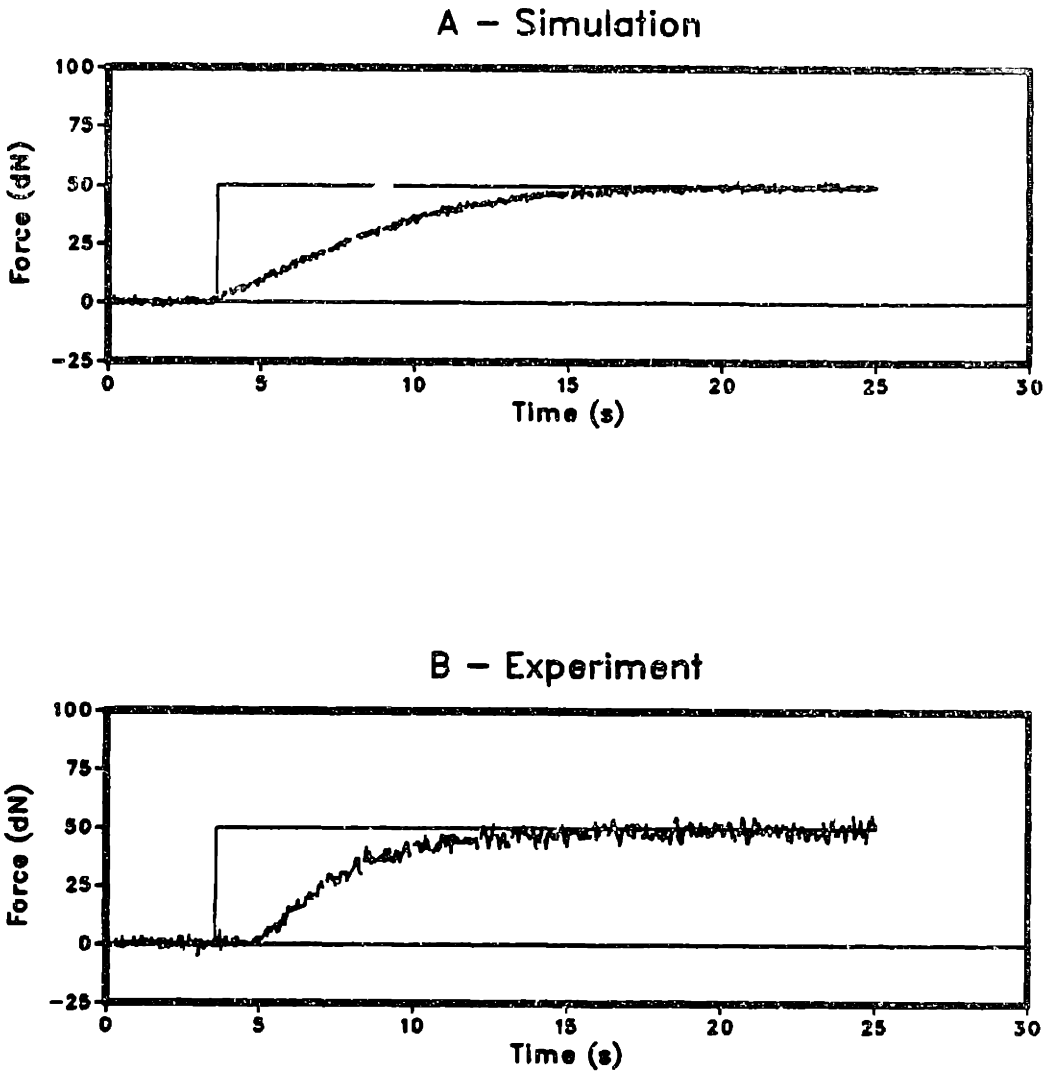

Figure 29. Step response of proportional - integral control: A - (K 0.3, T_i 20, a 0.011, b 0.17) B - (K 0.3, T_i 20)

increases, the closed loop poles of the linear approximation become closer to the unit circle (in the z-domain), thus the stability margin of the nonlinear system decreases. This is illustrated by the responses in Figure 30. Notice that the actual system became unstable at a lower force level than the simulation. The plots in Section 5 showed that the actual compliance tended to be stiffer than the model. In addition, the actual system is not a pure time delay, which was the model used in the simulation.

A desirable property of adding integral action to the control law is that it causes the closed loop system to seek the workpiece (seek a force). If r_k steps from zero to a positive force while the grinding disk is not in contact with the workpiece, the end effector will move in the tool z-direction until contact is made. The contact force increases until the steady state error is eliminated.

A PI controller will have a finite steady state error to a ramp input in either r_k or d_k. In Figure 31, the response of a PI controller regulating a desired force of zero while moving against a -5% ramp is shown. The steady state error is approximately 30 dN.

Each of the examples so far showed the controller regulating a constant desired force, r_k. In general, the controller also has to track time-varying inputs such as sinusoids. The response of the closed loop

A – Simulation

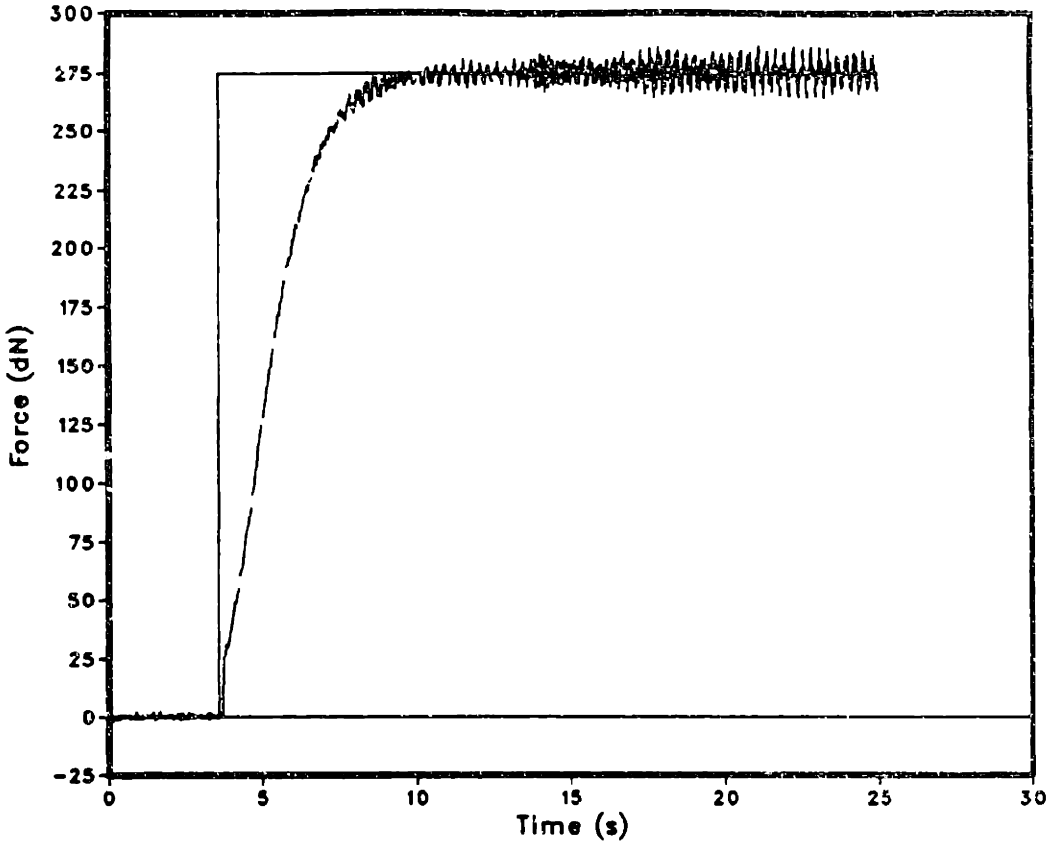

B – Experiment

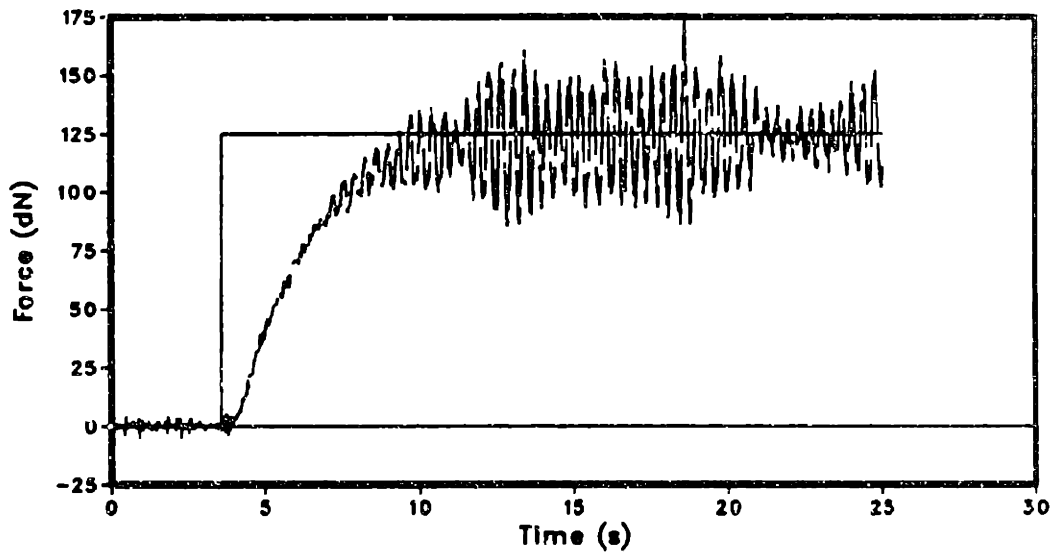

Figure 30. Steady state oscillations at high forces: A - (K 0.3, T_1 20, a 0.011, b 0.17) B - (K 0.3, T_1 20)

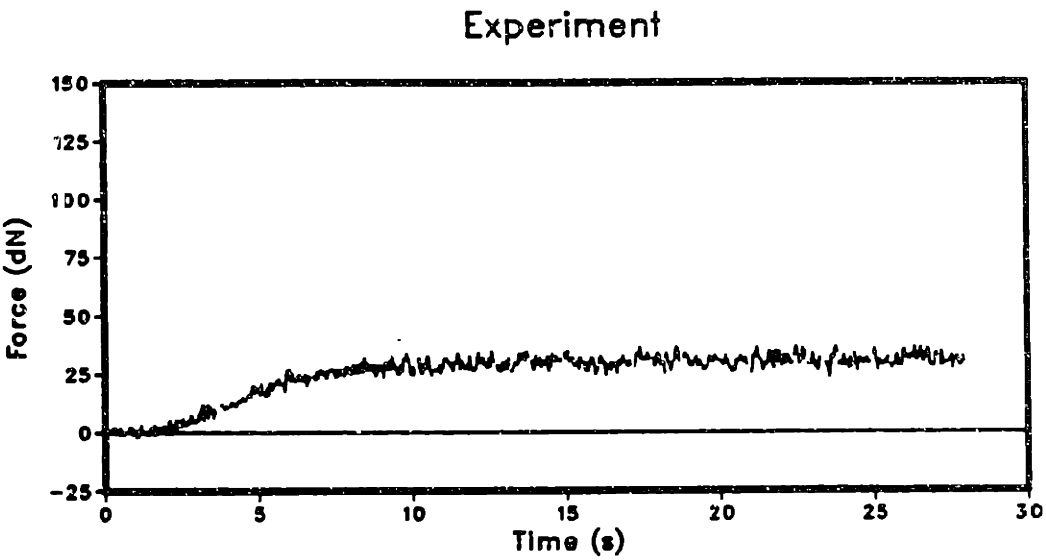

Figure 31. Steady state error to ramp disturbance for PI control: (K 0.3, T_i 20, grade -5%)

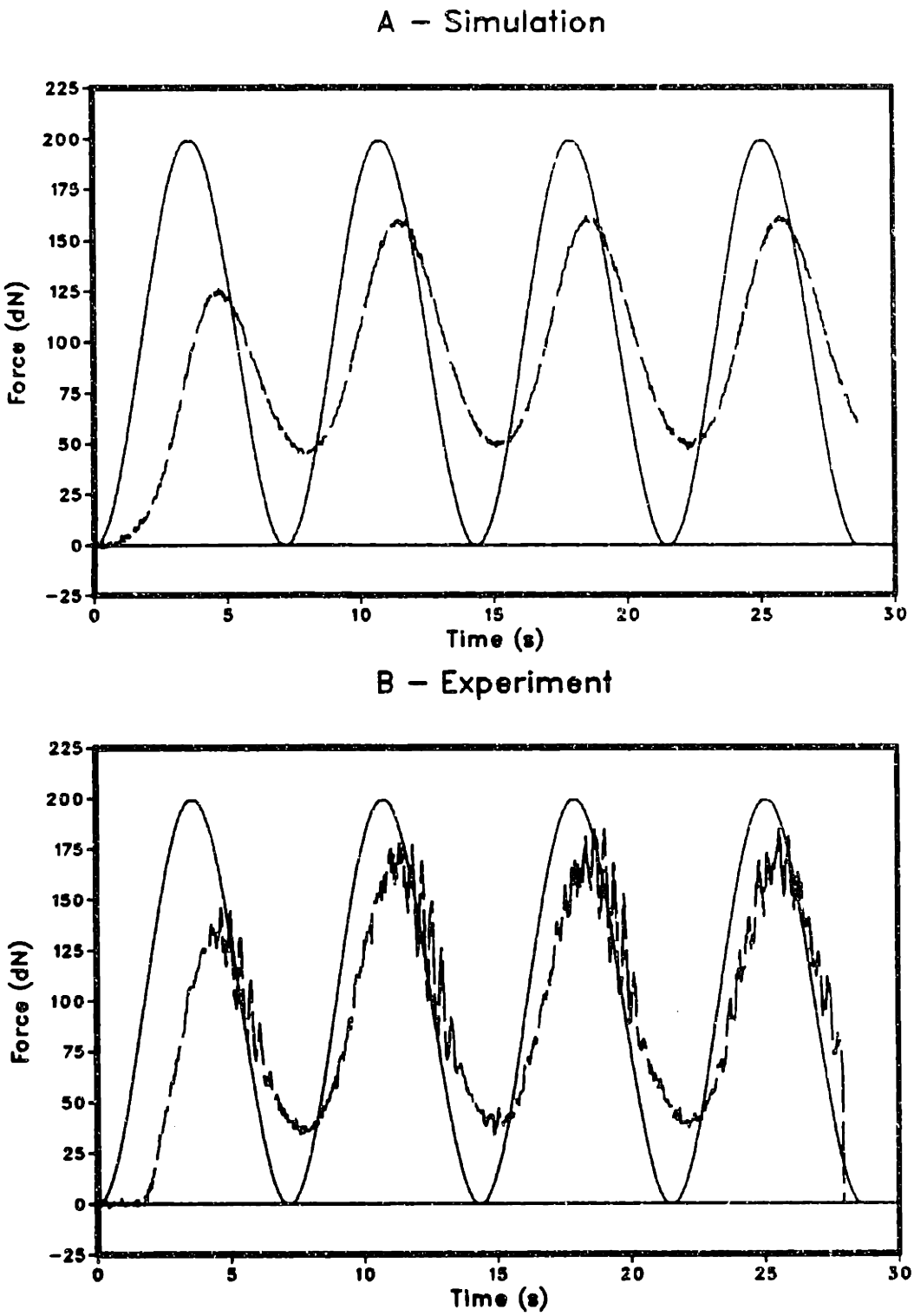

Figure 32. Sinusoidal response of a PI controller: 0.14 Hz, A - (K 0.3, T_1 20, a 0.011, b 0.17) B - (K 0.3, T_1 20)

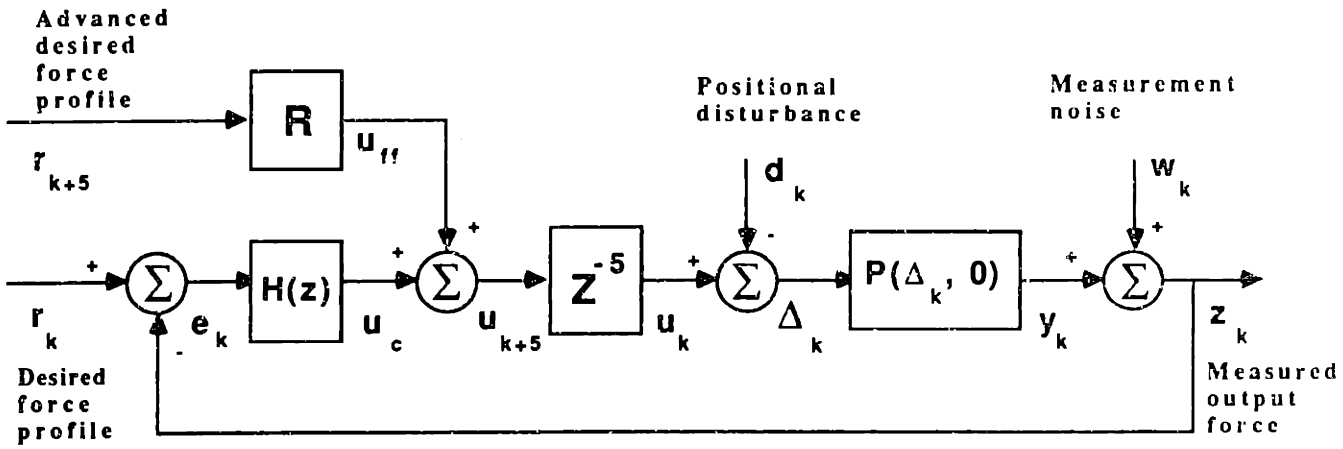

$$H(z) = K(1 + z/T_i\,(z - 1))$$

R = Constant gain

Figure 33. Block diagram of PI controller with linear feedforward compensation

system using PI control to a 0.14 Hz sinusoid varying from 0 to 100 dN is shown in Figure 32. The response is sluggish, and there is a phase lag due to the time delay. As with the step input, oscillations begin as force is increased.

Derivative action was tried in an effort to damp the oscillations, but this effort was unsuccessful. The derivative action had little effect on the response. Because a PI controller became oscillatory as force was increased, it was not an acceptable controller for a robotic grinding system.

6.5 LINEAR FEEDFORWARD COMPENSATION

Feedforward compensation is one way of reducing response times and compensating for phase lag. Consider first a plant consisting of a time delay followed by a linear spring. If the desired force, r_k, is known in advance, then the plant model can be inverted to determine the displacement commands necessary to produce the desired force. This is done by advancing r_k 5 time steps and feeding the advanced input through a feedforward gain. The gain should be chosen to be the reciprocal of the plant stiffness. In the case of nonlinear plant stiffness, an operating

range is determined and the feedforward gain can be chosen to be the average plant stiffness. A block diagram of the system with a PI controller and linear feedforward compensation is shown in Figure 33. The commanded displacement, u_{k+5}, is the sum of the closed loop displacement, u_c, and the feedforward displacement, u_{ff}. The feedforward gain, R, has units of compliance. The closed loop compensator acts to reject disturbances, d_k, and modeling errors in R.

The responses for step inputs of magnitudes 25, 50, and 75 dN are shown in Figure 34. The response is faster than PI control and the time lag is eliminated. However, the response undershoots for low inputs and overshoots for high inputs due to the nonlinear plant compliance. The time lag is also eliminated for sinusoidal inputs, shown in Figure 35, and the magnitude response improved.

6.6 NONLINEAR FEEDFORWARD COMPENSATION AND GAIN SCHEDULING

Consider a plant described by a time delay followed by a nonlinear compliance. Assume this compliance is a monotonic function of displacement. This plant can also be inverted. For the nonlinear stiffness described by equation (29), the inverse for positive forces is given by

$$R(r_k, 0) = (1/a)\ln[(a/b)r_k + 1] \quad r_k \geq 0 \tag{34}$$

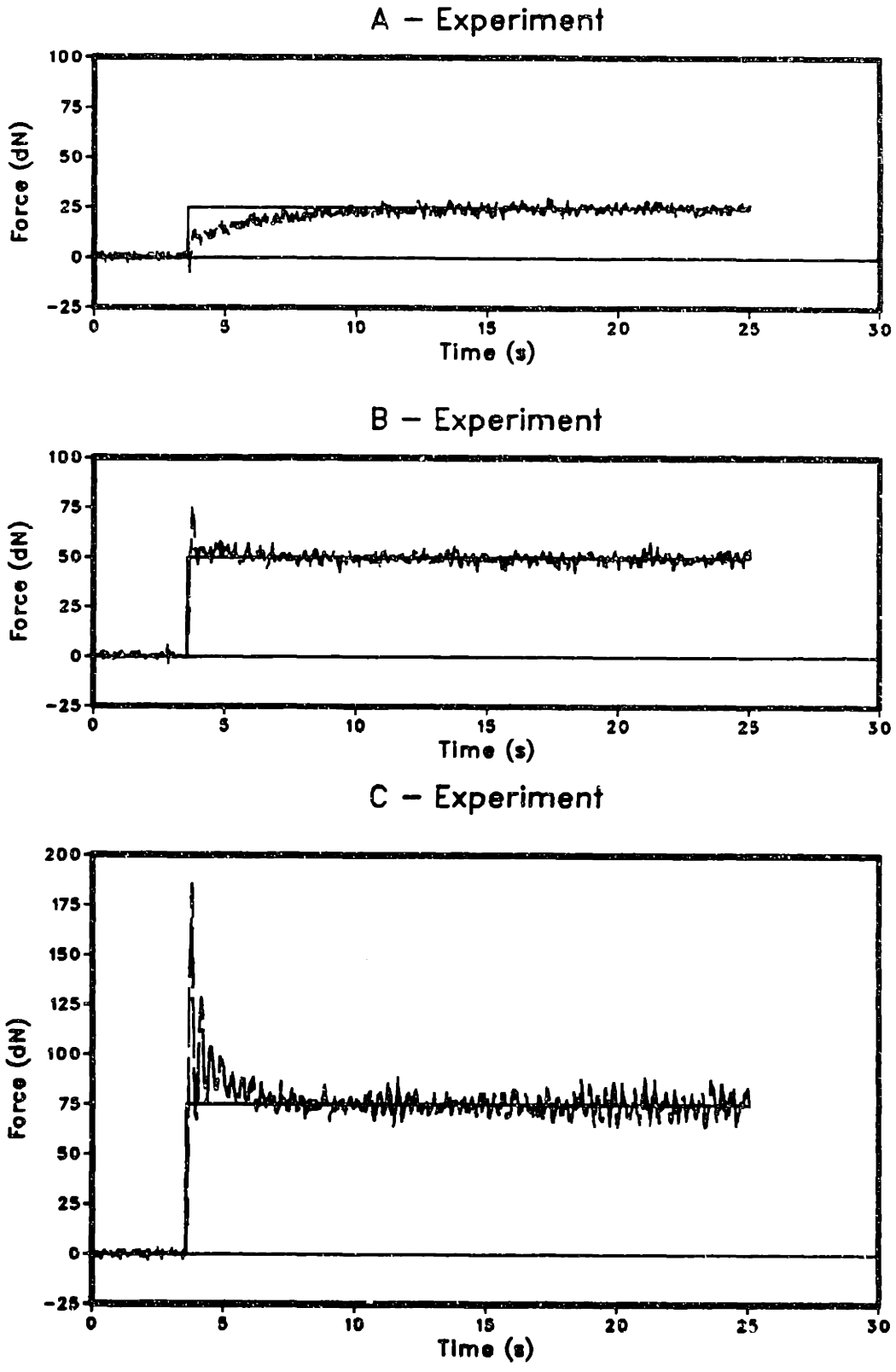

Figure 34. Step response of PI controller with linear feedforward compensation: (K 0.3, T_1 20)

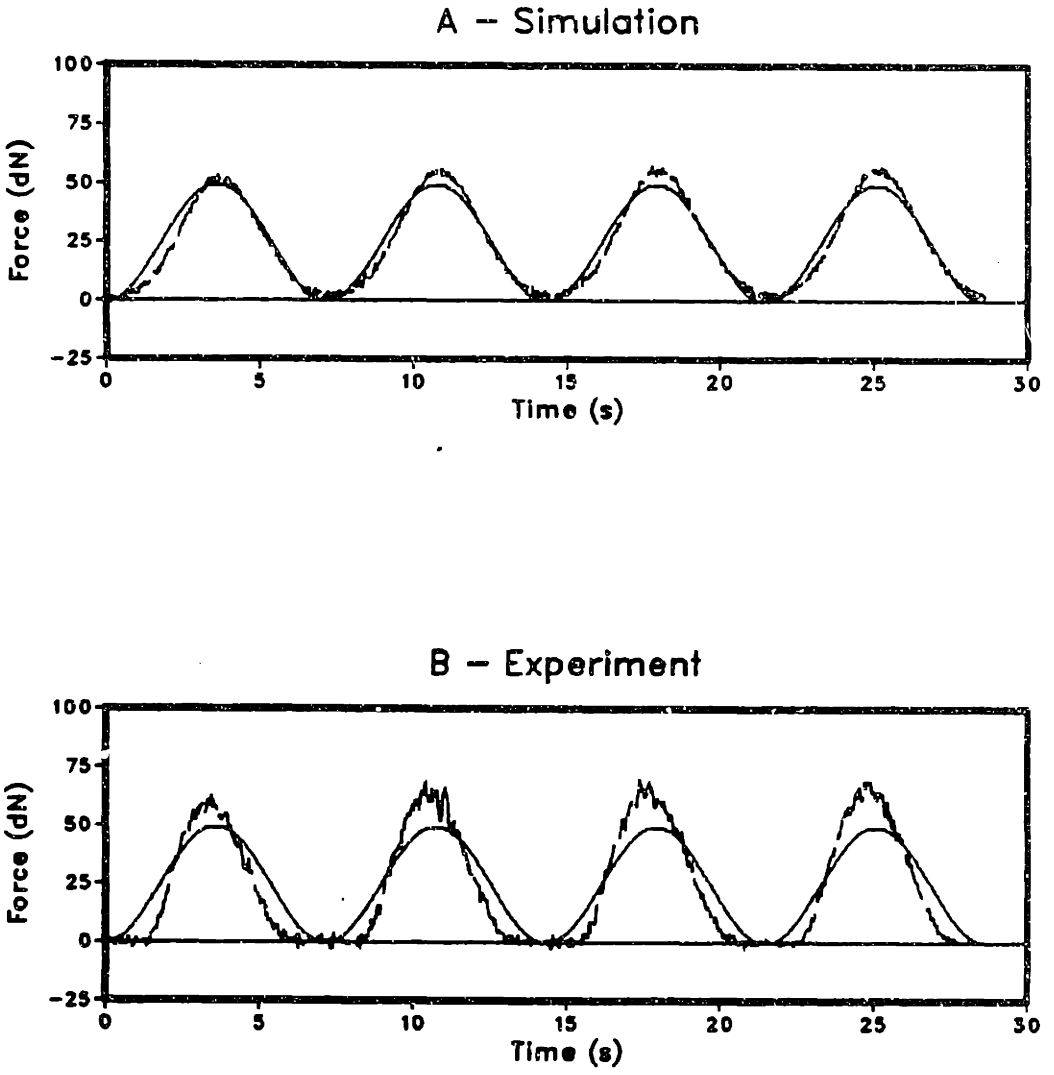

Figure 35. Sinusoidal response of PI controller with linear feedforward compensation: 0.14 Hz, A - (K 0.3, T_i 20, a 0.011, b 0.17) B - (K 0.3, T_i 20)

where r is the desired force and $R(r_k, 0)$ is displacement (again, the notation is for convenience). Thus, the linear gain, R, shown in Figure 33, can be replaced by the nonlinear function of the input $R(r_k, 0)$.

The controller gain, K, can be scheduled to provide stability at high force levels. One way to do this is to divide K by an estimate of the plant stiffness Φ_k. The plant stiffness as a function of force is given by equation (29). Using this equation and scheduling gain on the reference force profile yields

$$\Phi_k = ar_k + b \tag{35}$$

where Φ_k is the estimate of the actual plant stiffness P_a at time k. So, the overall gain of the closed loop system is KP_a/Φ. The block diagram for the system with nonlinear feedforward compensation and the gain scheduling is shown in Figure 36. This gain schedule will help reduce oscillations at high force levels because Φ_k increases as the reference force, r_k, increases. However, the error between the desired closed loop gain, K, and the actual closed loop gain, KP_a/Φ, increases with tracking error. So, if the tracking error is large, then other undesirable effects may be caused by the gain schedule.

Figure 37 illustrates the step responses to different force levels. Note the increased uniformity of these responses compared with the step responses in Figure 34. The improvement is mainly due to replacing the constant R by $R(r_k, 0)$ in the feedforward compensation.

The sinusoidal response shows a more significant improvement. Figure 38 and Figure 39 show the response to three 0.14 Hz sinusoids of increasing amplitude. Like the step response, the tracking was improved by the use of $R(r_k, 0)$ in place of the constant R. Also, stability was improved at high force levels because of the gain schedule.

Figure 39 shows that the tracking error begins to degrade at 400 dN. The error, shown at the top of each curve, is integrated. Undershoot indicates that the system model is stiffer than the actual plant. The precomputed feedforward compensation and the closed loop gain are therefore lower than desired. As the input cycles back to 0 dN force, the model improves and the closed loop gain increases. This makes the integrated error more significant causing the undershoot observed at low forces in Figure 39. This is one example of integrator windup.

The major limitation of this control architecture (shown in Figure 36) is poor disturbance rejection properties. The controller's inability to track a sinusoid while rejecting a -5% ramp is illustrated in Figure 40. Of the three signals, e, Φ, and u_{ff}, used to compute the

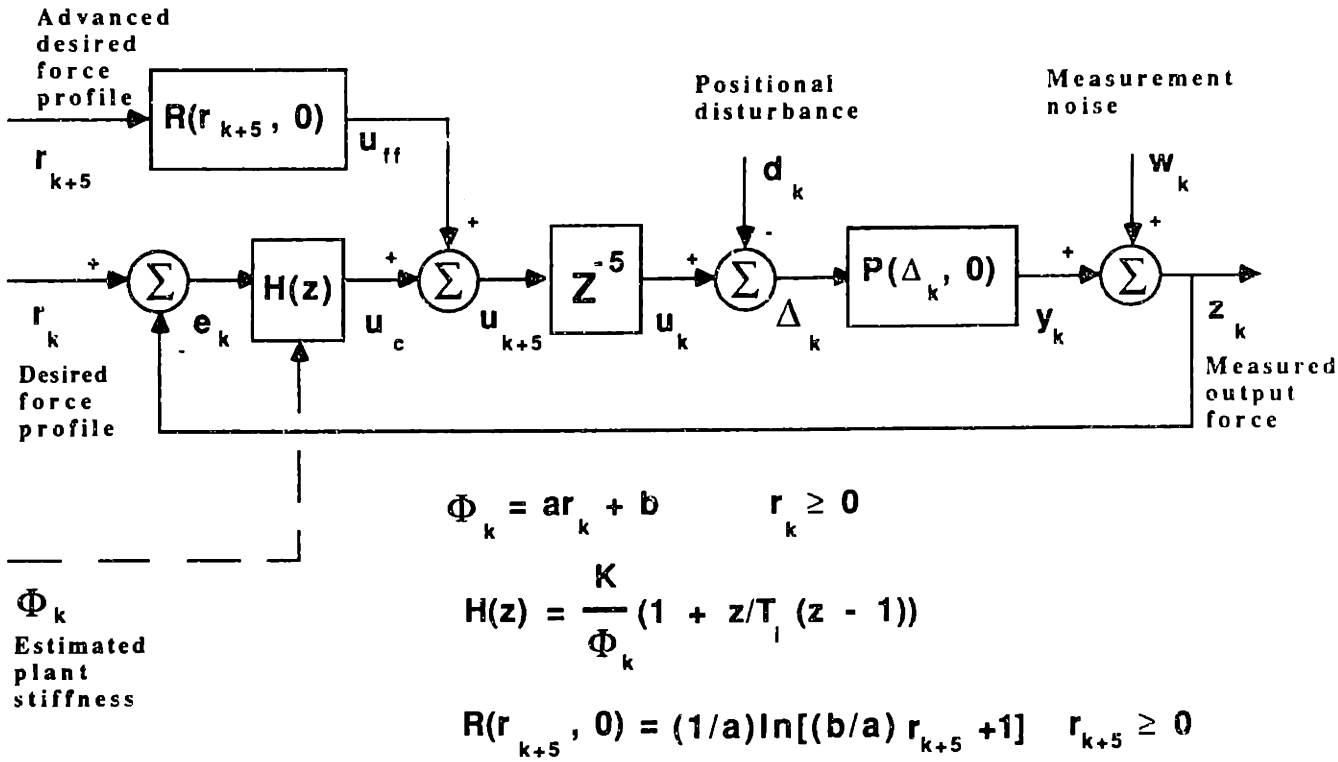

Figure 36. Block diagram of PI controller with nonlinear feedforward compensation and gain scheduling

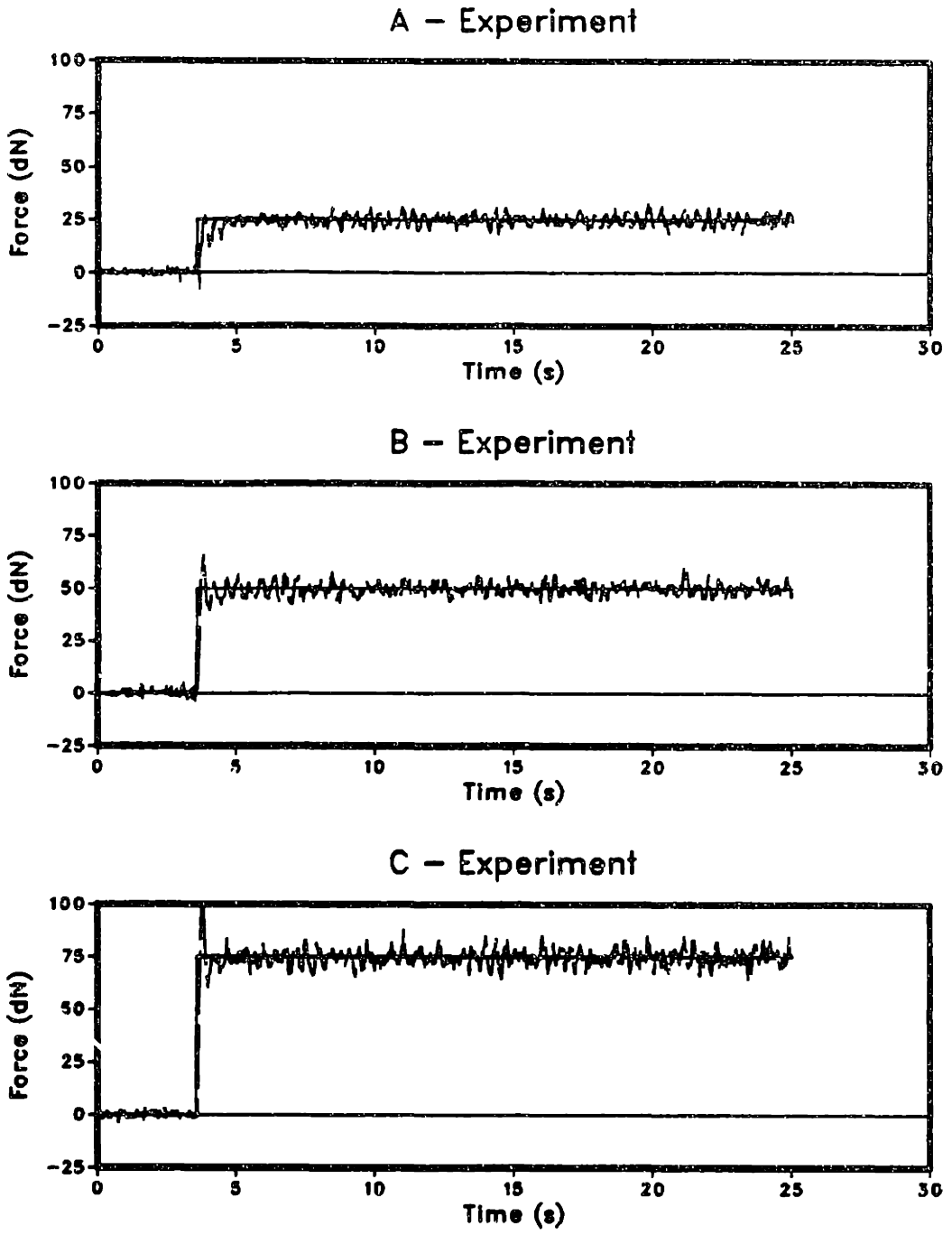

Figure 37. Step response of PI controller with nonlinear feedforward compensation and gain scheduling: (K 0.25, T_1 10, a 0.012, b 0.2)

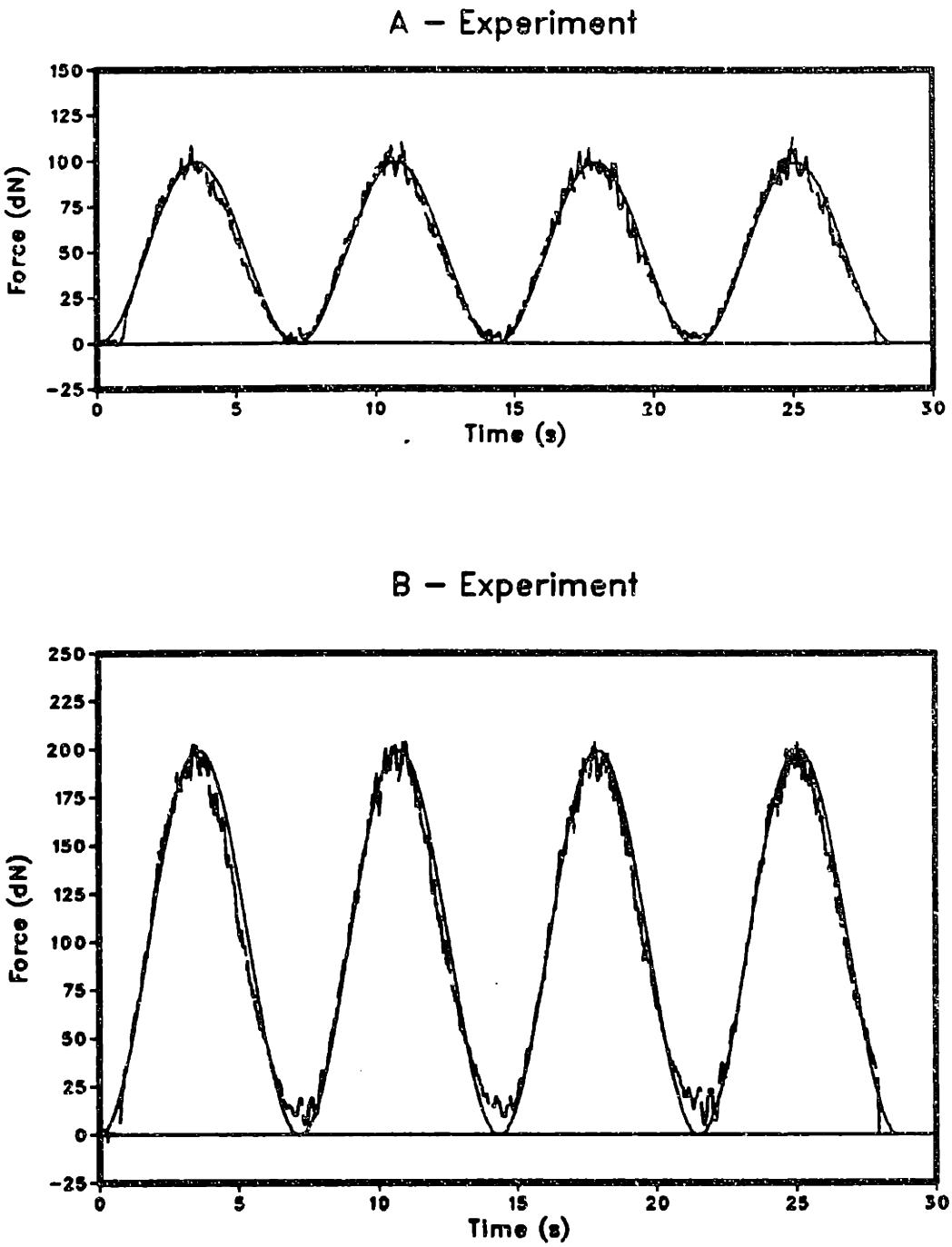

Figure 38. Sinusoidal response of PI controller with nonlinear feedforward compensation and gain scheduling (100 & 200 dN max.): (0.14 Hz, K 0.25, T_i 10, a 0.012, b 0.2)

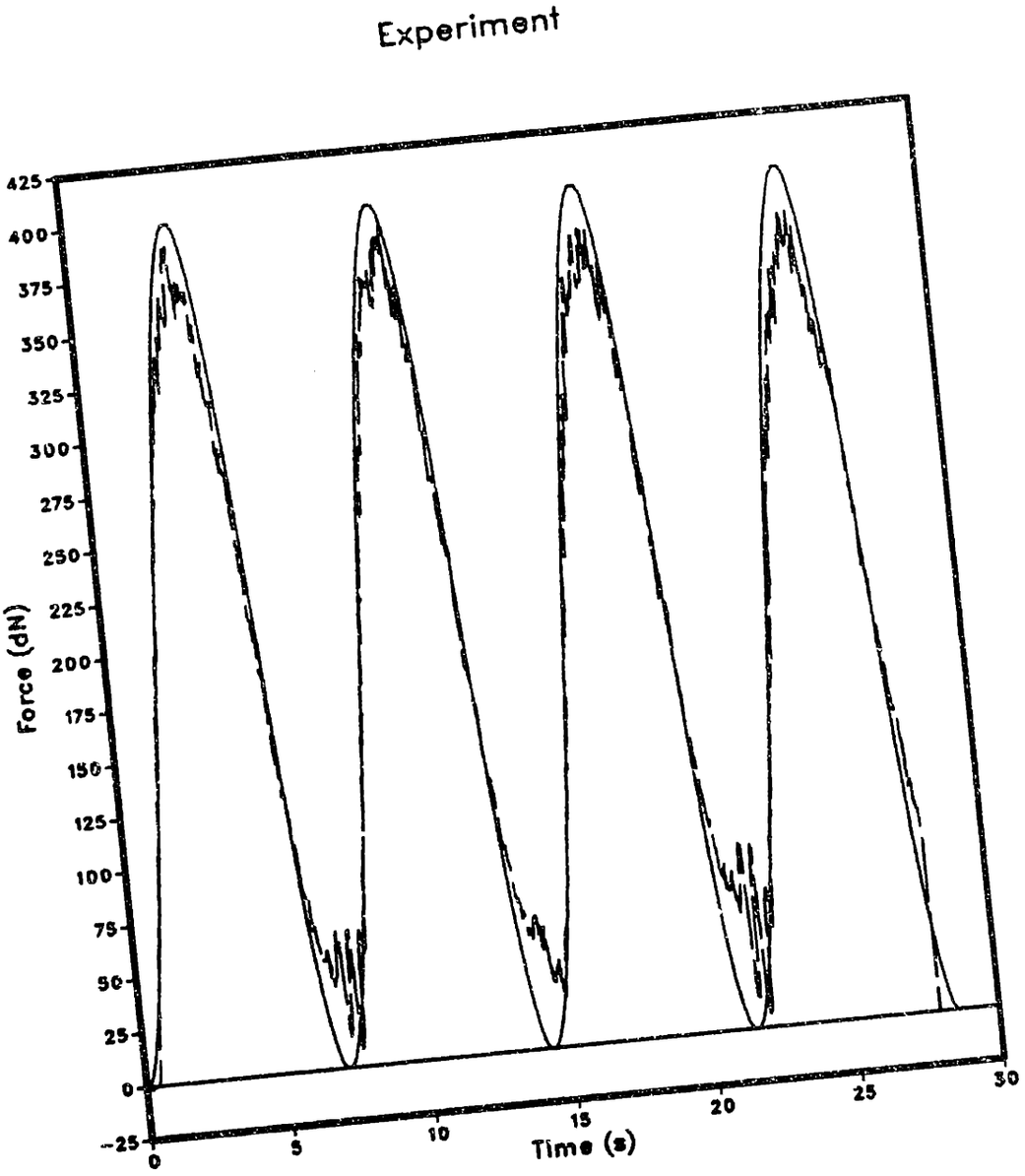

Figure 39. Sinusoidal response of PI controller with nonlinear feedforward compensation and gain scheduling (400 dN max.): (0.14 Hz, K 0.25, T_1 10, a 0.012, b 0.2)

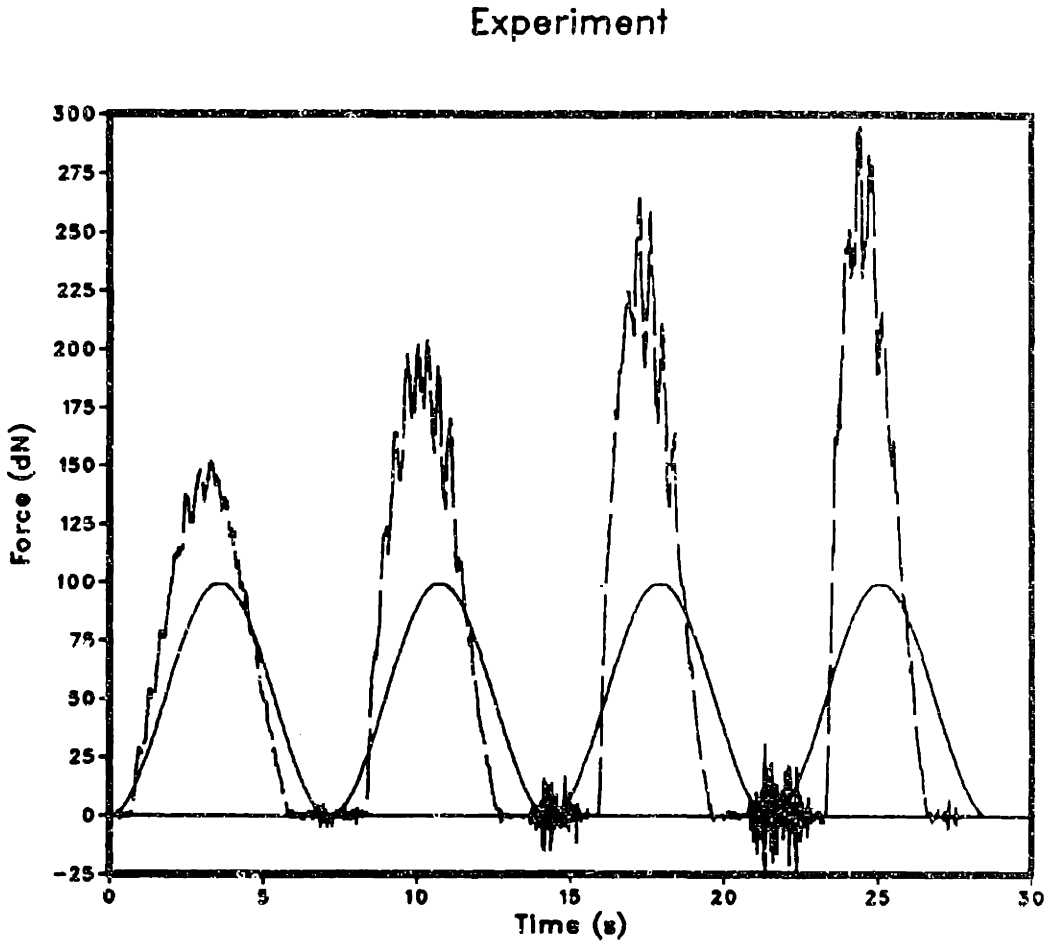

Figure 40. PI controller with nonlinear feedforward compensation and gain scheduling rejecting a -5% ramp: (0.14 Hz, K 0.25, T_i 10, a 0.012, b 0.2)

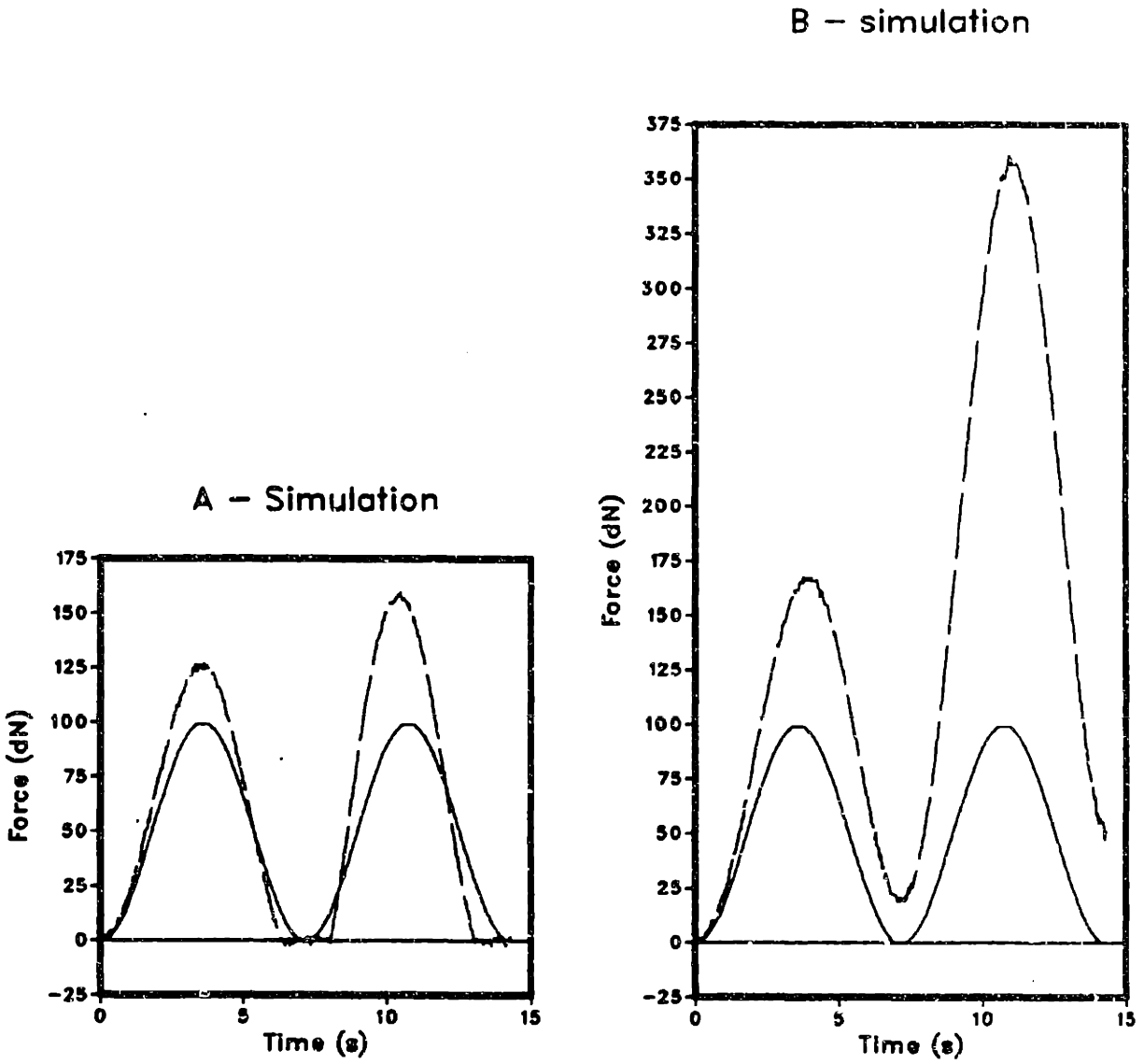

Figure 41. Effect of the integrator in rejecting a -5% ramp: (0.14 Hz, K 0.25, T_1 10, a 0.011, b 0.17)

control signal, u_{k+5}, two are functions of the input only. These signals, u_{ff} and Φ, can be considered open loop compensation. In general, open loop compensation tends to degrade the disturbance rejection properties of a controller.

Consider the nonlinear function $R(r_k, 0)$. This function calculates the estimated displacement from the nominal surface of the workpiece necessary to achieve the desired force. As the error between the actual and nominal contour of the workpiece increases, the accuracy of this estimate decreases. Also, the accuracy of the system stiffness estimate, Φ, decreases as the tracking error increases. The PI closed loop compensator does help the controller track the disturbance. This is shown in Figure 41. This test was performed using a simulation to protect the hardware. If the ramp in this simulation leveled out to 0° slope, then the tracking error would have been attenuated. The disturbance rejection properties of this controller are not adequate for automated grinding.

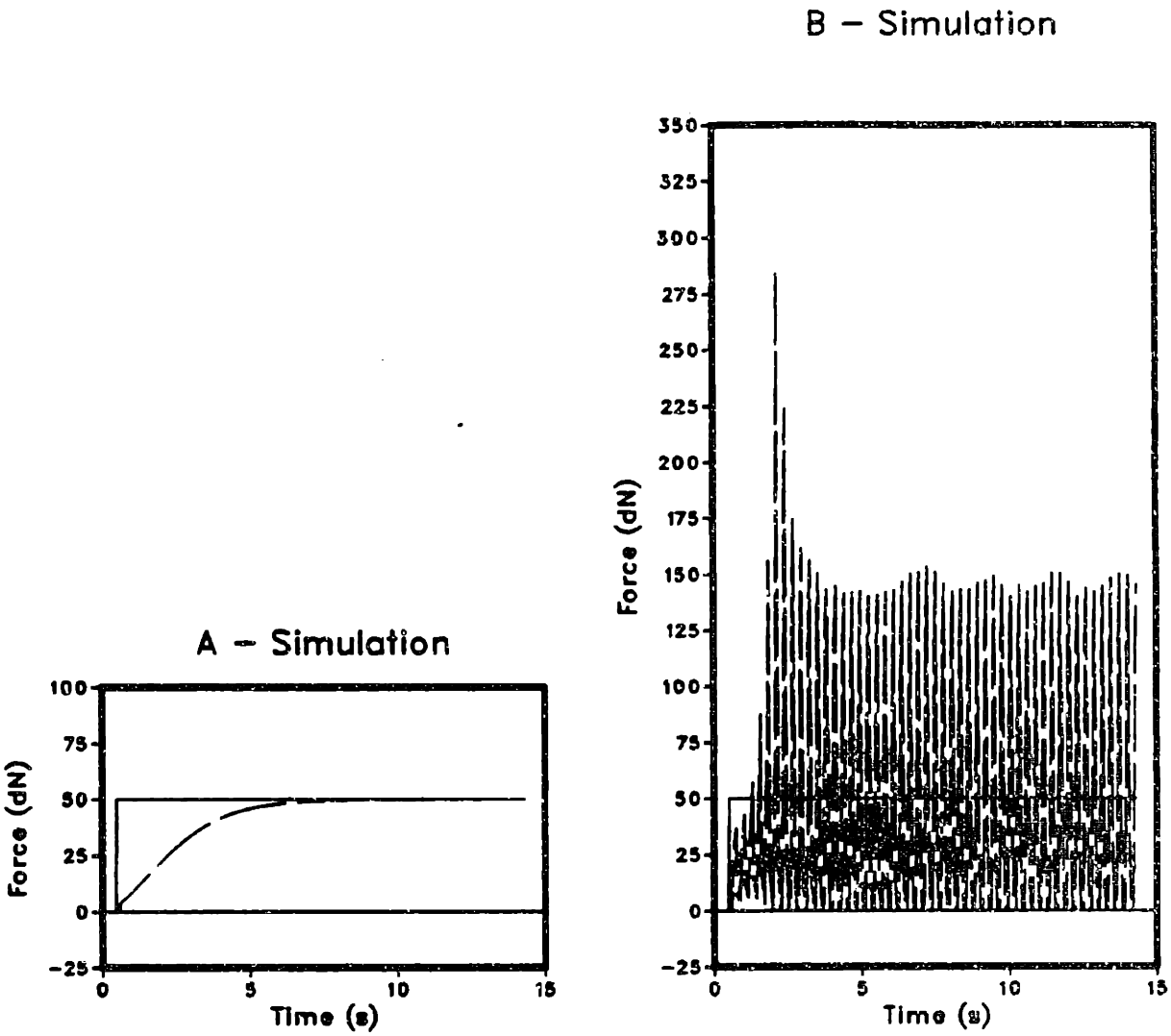

Figure 42. Step response comparison for gain scheduled on input and output: (K 0.25, T_1 10, a 0.011, b 0.17) A - gain scheduled system B - model reference adaptive system

6.7 MODEL-REFERENCE ADAPTIVE SYSTEM

In the previous controller using gain scheduling, the gain was a function of the input only. In general, controller gains can be functions of any available measurement. Controliers that adjust gains in this way generalize to the class of model-reference adaptive systems. For systems in which the plant characteristics change slowly compared to the system response time, this type of controller can compensate for parameter changes. A typical application is systems with aging components. In the case of a nonlinear compliance, the purpose is to compensate for the changing compliance of the plant. This requires the controller parameters to be updated at a rate that is at least of the same order of magnitude as the inverse of the system response time. Closed loop adjustment of controller parameters at this high rate tends to create a limit cycle.

For this plant, no algorithm of this type was found that could adjust the gain rapidly enough to insure stability problem at high forces. The simplest algorithm

$$\Phi_k = ay_k + b \tag{36}$$

illustrates the general result. This estimate, Φ_k, of the system stiffness, simply replaces the gain scheduled estimate shown in Figure 36. In Figure 42, the response of a gain scheduled controller is compared with the response of this model-reference adaptive controller. Because

of the oscillatory response, a model-reference adaptive controller was not implemented in the laboratory. In both cases, the feedforward compensation was not used and noise was removed from the output signal. In summary, no method was found to adjust the gain, closed loop, rapidly enough to be useful.

6.8 NONLINEAR CONTROL

The controllers considered so far are inadequate for an automated grinding system. In this section, a nonlinear design able to meet the objectives stated in the beginning of Section 6 is proposed. The compensator is derived in a general form. In this form, the nonlinear controller can be applied to any plant that can be modeled as a time delay followed by an invertible compliance. The time delay must be modeled as an integer multiple of the sampling period and the compliance must be modeled as a monotonic function of deflection. The controller was implemented on the PUMA robot system and the results are shown in Section 6.8.9.

For this system, the time delay in the IBM PC-AT and VAL-II were combined, yielding a delay of 5 sampling periods (0.14 s). It is also assumed that the desired force, r_k, is known a priori.

6.8.1 Nonlinear Control Design

This section describes the design of a nonlinear controller. The derivation is informal; justifications for the steps taken are made by examples. To begin, it is useful to list the major assumptions that are addressed in the following subsections.

- The purpose of the controller is to track a desired input force signal.
- The time delay (z^{-n}) is the dominant dynamic effect. It is assumed that the difference between the actual time delay and the model (integer multiple of the sampling period) is negligible.
- The plant compliance P_a is generally nonlinear and is the source of modeling errors. These modeling errors can also cause unstable behavior.
- When displacement commands reach the compliance, they are corrupted by positional disturbances. These disturbances must be rejected.

- Feedback is provided by measurements of the output force. These measurements are corrupted by noise.

6.8.2 Invertible Compliance Model

The stiffness model (P) is assumed to be monotonic function of displacement. P is therefore an invertible function. Suppose the nonlinear stiffness model is given by

$$v = P(q_2, q_1) \tag{37}$$

where v is the change in force when the displacement changes from q_2 to q_1. Consider the case when the stiffness is displaced a distance q_2 from the relaxed position ($q_1 = 0$). The resulting change in force is given by

$$v_2 = P(q_2, 0). \tag{38}$$

The displacement caused by changing the force from 0 to v_2 is given by

$$q_2 = R(v_2, 0). \tag{39}$$

Thus, R is defined to be the inverse of P. In general,

$$q = R(v_2, v_1) \tag{40}$$

where q is the change in displacement caused by a change in force from v_1 to v_2.

6.8.3 Alternative Form for Feedforward Compensation

In Section 6.4, the plant was inverted in the feedforward path. The idea was to anticipate the desired force 5 sampling periods in the future. The equation was

$$u_{ff} = R(r_{k+5}, 0) \tag{41}$$

where r_{k+5} is the advanced desired force and u_{ff} is the feedforward compensation (displacement). An alternative form for the inverted plant is now derived. Let n be the time delay of the plant. Then, in general

$$u_{k+n} = \int_0^v df/P(f) \qquad (v = r_{k+n}) \tag{42}$$

or

$$u_{k+n} = R(r_{k+n}, 0). \tag{43}$$

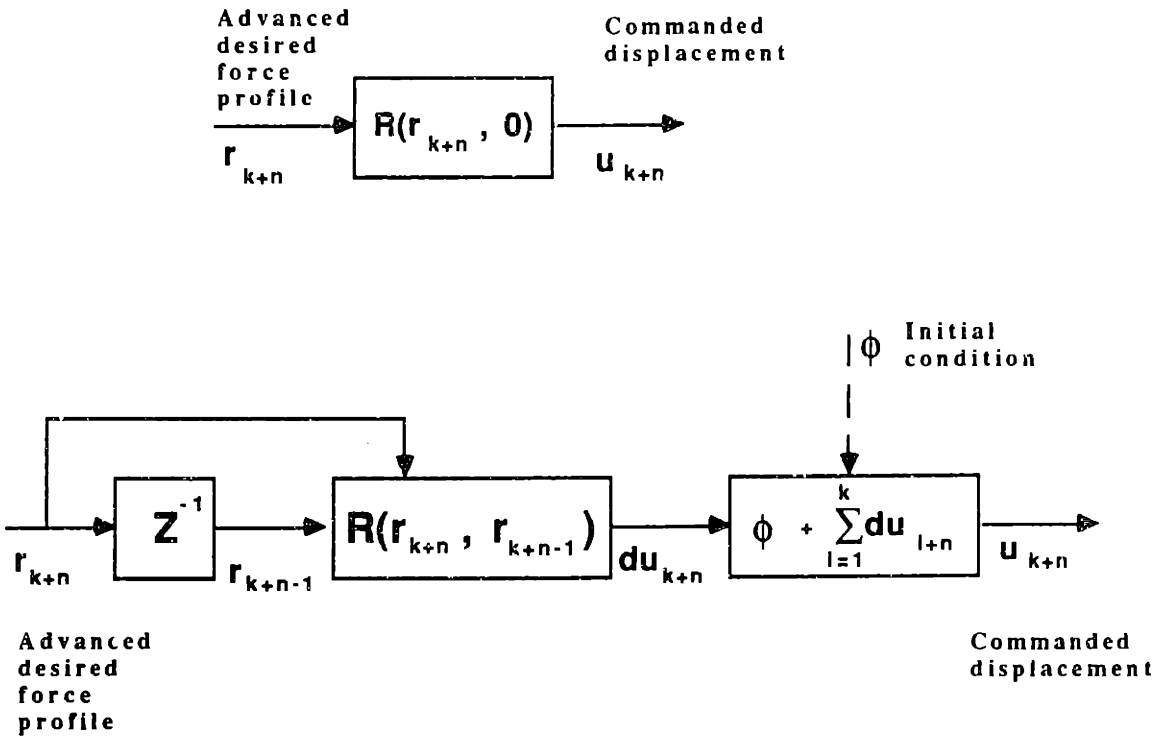

Figure 43. Model of inverted plant

Thus, the feedforward displacement is found by integrating the reciprocal of the the nonlinear stiffness from 0 to the desired force. Let

$$du_{k+n} = u_{k+n} - u_{k+n-1} \tag{44}$$

then

$$du_{k+n} = R(r_{k+n}, r_{k+n-1}) \tag{45}$$

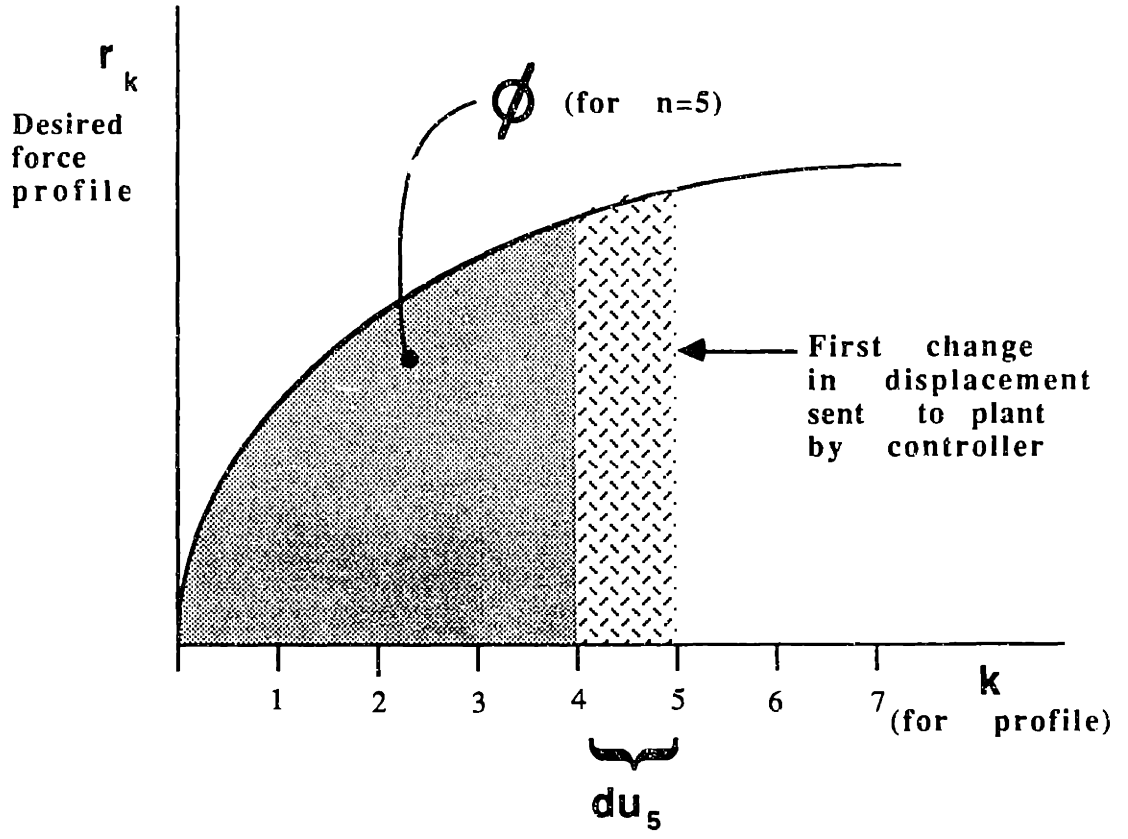

Figure 44. Initial condition for alternative form of feedforward compensation

where du_{k+n} is the commanded change in displacement. In particular, note that

$$u_n = u_{n-1} + du_n. \tag{46}$$

Since the input signal starts with r_n (because it is advanced by n) u_{n-1} must be determined as an initial condition. Let

$$\phi = R(r_{n-1},\ 0) \tag{47}$$

be the initial condition (see Figure 44). The inverted plant model may be represented as shown in Figure 43. Both forms shown in Figure 43 are equivalent. The second form of open loop control is summarized as

$$du_{k+n} = R(r_{k+n},\ r_{k+n-1}) \tag{48}$$

$$u_{k+n} = \phi + \sum_{i=1}^{k} du_{i+n}$$

At any time k, u_{k+n} is the commanded displacement that will reach the compliance at the future time k+n if the plant is purely a n-step time delay.

6.8.4 Open Loop Control

The inverted plant given by equation (48) may be used as an open loop controller. This was the motivation for the nonlinear feedforward compensation discussed in Section 6.4. However, as also discussed in Section 6.4, open loop compensation is not robust to modeling errors or disturbances. The nonlinear control law is based upon the second form of open loop control given by equation (48). The robustness of the non-

linear control law is shown, in part, by comparison with open loop control.

Figure 45 and Figure 46 illustrate how the compliance model given by equation (29) on page 87 changes with the parameters a and b. The response of open loop compensation when the plant is stiffer than the model is shown in Figure 47 (the nonlinear controller reduces to open loop compensation given by equation (48) when K = 0). For the case of a stiff model, open loop compensation is shown in Figure 48, plot A.

6.8.5 A Hypothetical Example

The following hypothetical example will serve to illustrate the reasoning behind some of the steps that were taken in the design of the nonlinear control law. For this example assume that the following is true:

- The compliance model (P) is an exact representation of the actual compliance (P_a),
- There is no measurement noise ($w_k = 0$, $z_k = y_k$),
- Initial conditions are $y_0 = r^*$ and $d_k = 0$,
- The desired force is $r_k = r^*$ for all k.

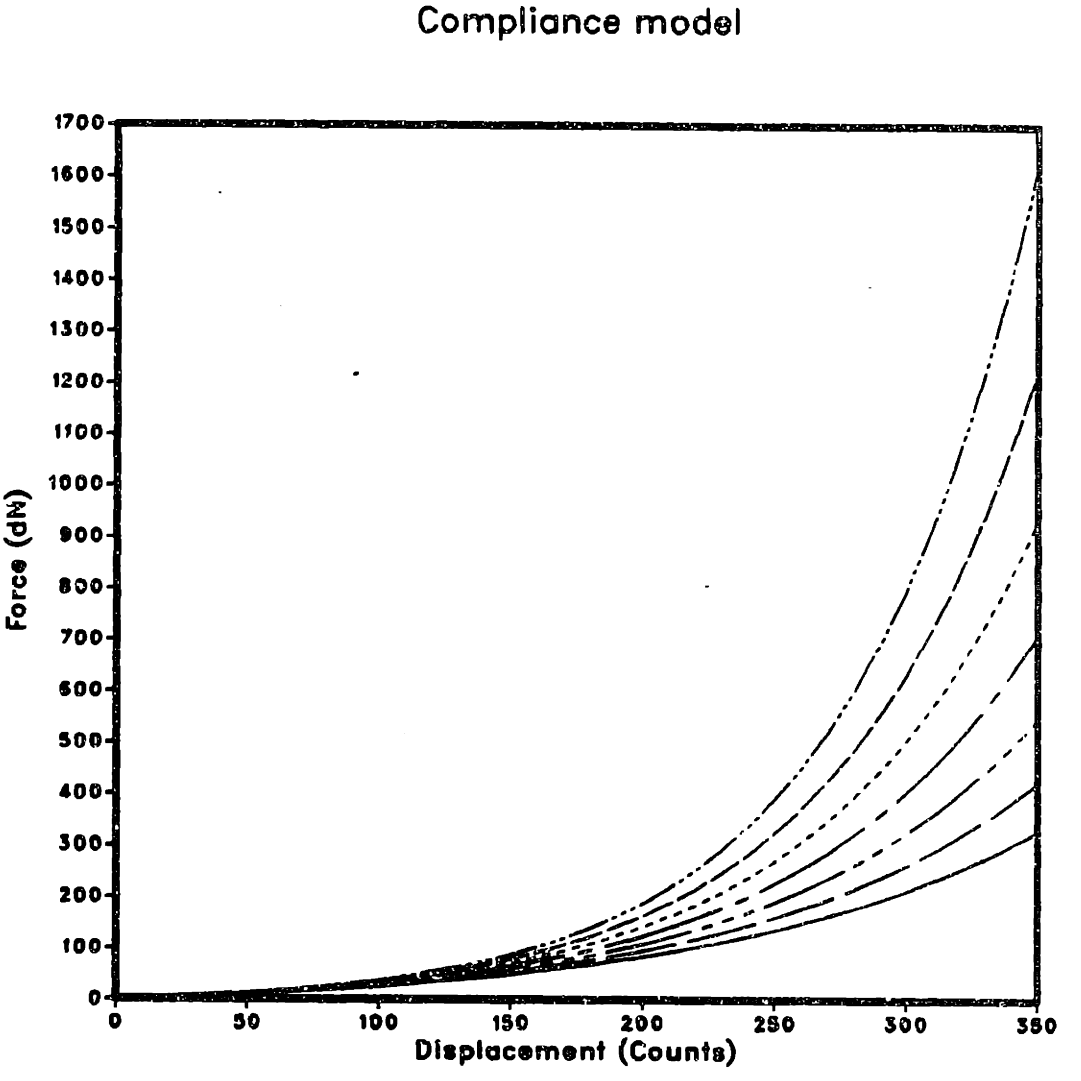

Figure 45. Effect of changes in parameter (a) on the compliance model: (b - 0.17 all plots), (a - 0.14, 0.13, 0.12, 0.11, 0.10, 0.09, 0.08 in order from top to bottom) (1 count = 0.03125 mm)

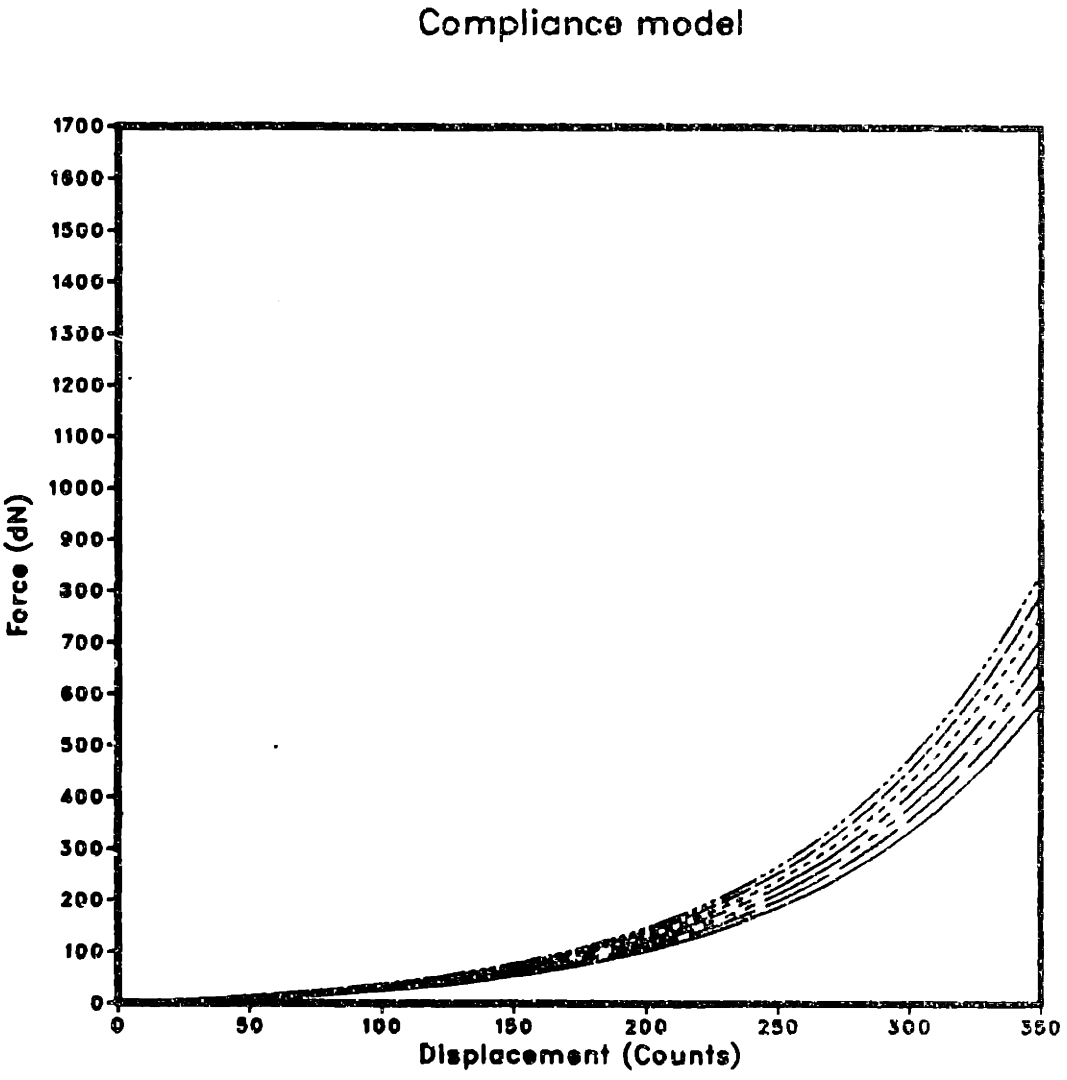

Figure 46. Effect of changes in parameter (b) on the compliance model: (a - 0.011 all plots) (b - 0.20, 0.19, 0.18, 0.17, 0.16, 0.15, 0.14 in order from top to bottom) (1 count = 0.03125 mm)

In summary, the system is at steady state, under ideal conditions, with no force error. At time k1 there is an ideal step disturbance $d_{k1} = -1$.

Two possible closed-loop controller designs are now proposed that lead up to the final design (Design #3). This example will be used to illustrate some of the properties of the proposed designs. Experimental results are presented in Section 6.8.9 for design #3.

6.8.6 Design #1 - The Stability Problem

The purpose of this design is to illustrate that the time delay causes a stability problem. Consider the use of the open loop controller given by equation (48). Referring to the example, d_{k1} will cause a steady state error. Under the conditions stated, it is possible to calculate the change in displacement necessary to cancel the disturbance in n sample periods. The correction (calculated at time k1) is given by:

$$du_{k1+n} = R(r^*, y_{k1}) = -d_{k1} = 1. \tag{49}$$

However, this correction is desired at time k1 only. A controller of the form

$$du_{k+n} = R(r_{k+n},\ y_k) \tag{50}$$

$$u_{k+n} = \phi + \sum_{i=1}^{n-1} du_{k+i}$$

is not acceptable; it will either become unstable or lead to a limit cycle. This is because the controller makes corrections n times prior to feedback.

The major source of unstable behavior is the time delay. At any time k there are always n-1 commanded displacements that have already been sent by the controller, but have not affected the plant compliance. In order to compensate for the time delay, the controller will be provided with a memory.

6.8.7 Design #2 - Use of Memory to Solve the Stability Problem

The idea behind this design is to send the commanded displacement, du_{k+n}, based on an estimate of what the measured force will be n-1 sampling periods in the future. This controller is derived in general, and then an example will be considered.

At any time k, the net deflection of the compliance, Δ_k, may be estimated from the measured output force, z_k, by

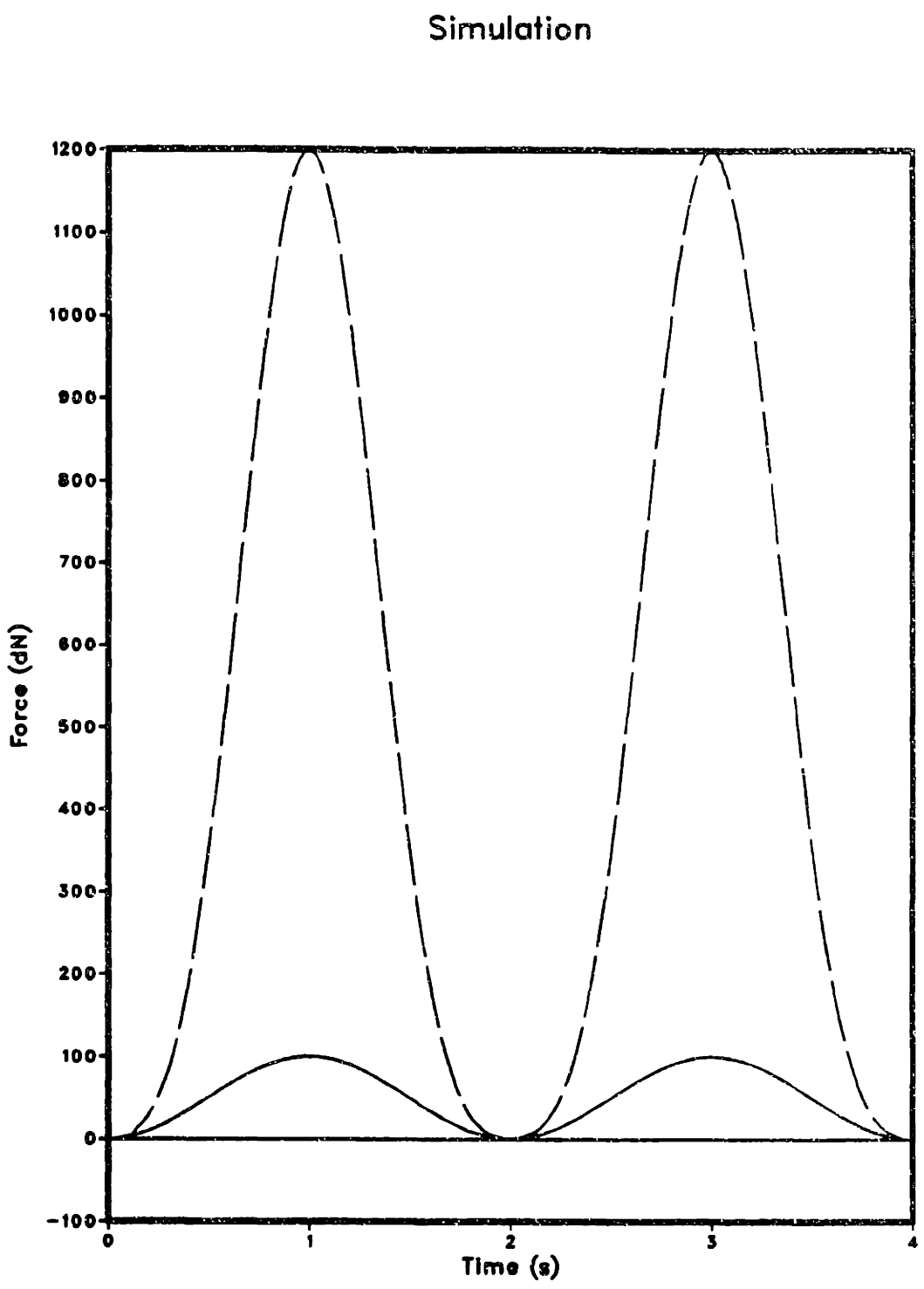

Figure 47. Nonlinear control when plant is stiffer than model (k = 0): actual compliance - (a 0.02, b 0.2) model compliance - (a 0.01, b 0.1)

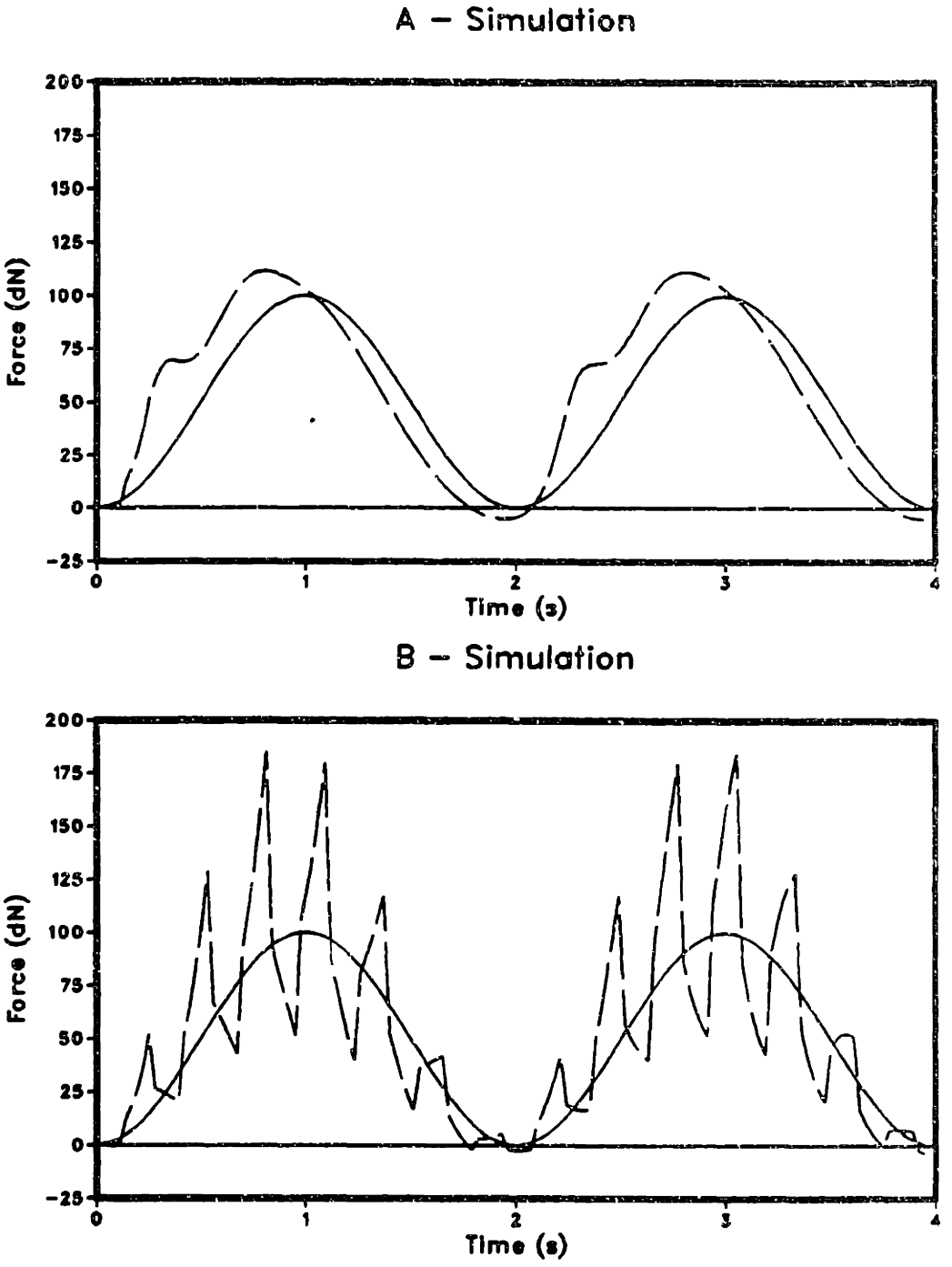

Figure 48. Nonlinear control when plant is stiffer than model A - (K = 0.14), B - (K = 1): actual compliance - (a 0.02, b 0.2) model compliance - (a 0.01, b 0.1)

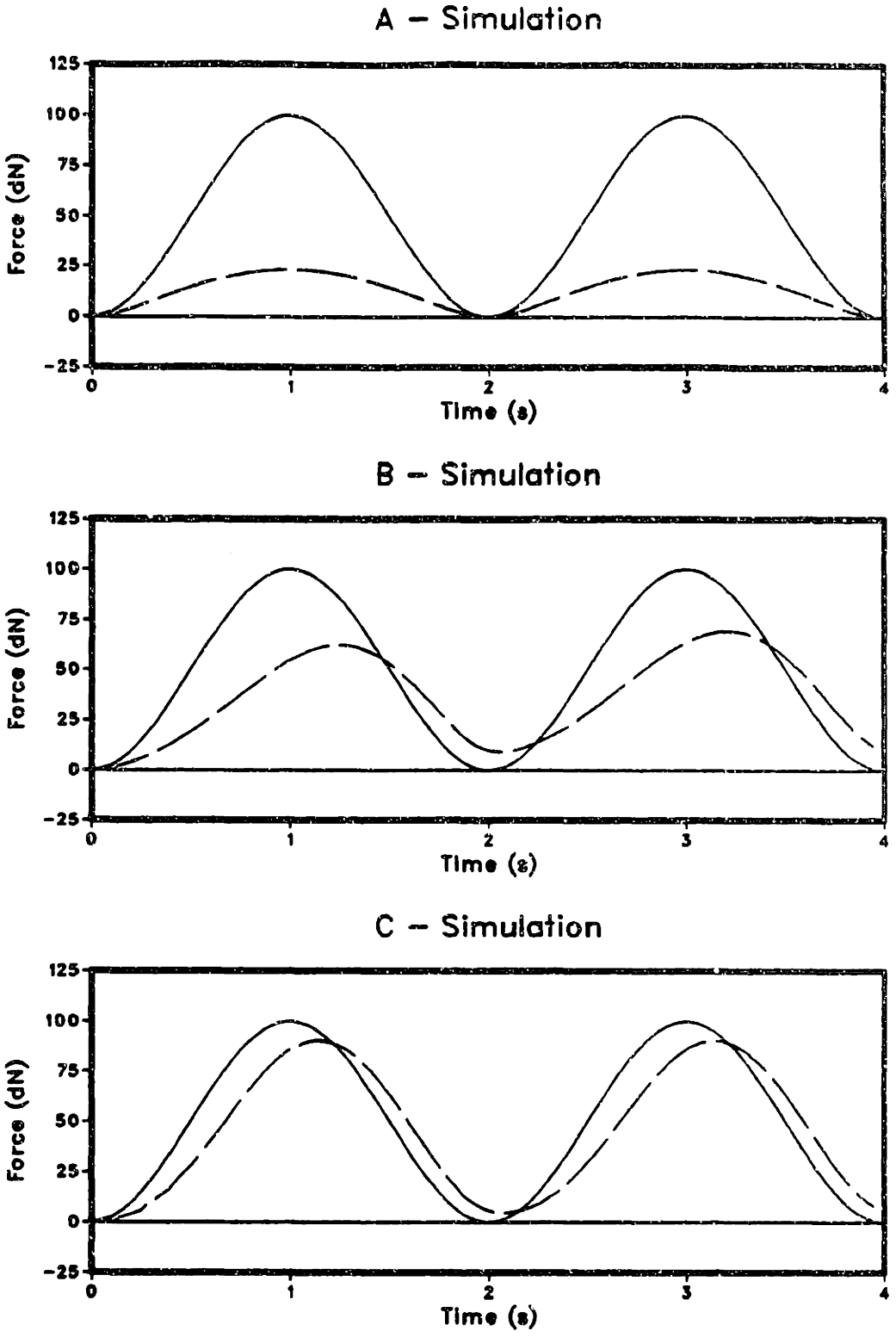

Figure 48. Nonlinear control when model is stiffer than plant: actual compliance - (a 0.02, b 0.2) model compliance - (a 0.01, b 0.1) A - (k = 0) B - (k = 0.14) C - (k = 1)

$$\Lambda_k = R(z_k, 0) \tag{51}$$

where Λ_k is defined to be an estimate of Δ_k. In the same way, an estimate of the future deflection Δ_{k+n-1} can be defined as

$$\Lambda_{k+n-1} = \Lambda_k + du_{k+1} + \ldots + du_{k+n-1}. \tag{52}$$

Thus, the estimate is formed by adding the next n-1 commanded changes in displacement that have already been sent by the controller to the plant. Further, the estimated future force, Ψ_{k+n-1}, is given by

$$\Psi_{k+n-1} = P(\Lambda_{k+n-1}, 0). \tag{53}$$

Using this estimated future force, the second controller is given as

$$du_{k+n} = R(r_{k+n}, \Psi_{k+n-1}) \tag{54}$$

$$u_{k+n} = \phi + \sum_{i=1}^{n-1} du_{k+1}.$$

Considering the example again, because there are no modeling errors the estimated deflection at time k is simply the actual deflection. That is

$$\Lambda_k = \Delta_k = u_k - d_k. \tag{55}$$

Therefore, at time k1 the commanded change in displacement, du_{k1+n}, is

$$du_{k1+n} = R(r^*, \psi_{k1+n-1}) = -d_{k1} = 1.$$

since $du_{k1+1} = du_{k1+2} = \ldots = du_{k+n-1} = 0$. So, this commanded displacement is the same as given by design #1. The improvement is illustrated by considering the commanded displacement at time k1+1. Because of the time delay, the estimated deflection, $\Delta_{(k1+1)}$, is the same as at time k1. The estimated future deflection, $\Lambda_{(k1+1)+n-1}$, is given by

$$\Lambda_{(k1+1)+n-1} = \Delta_k + du_{(k1+1)+n-1} = u_{k1} \tag{56}$$

Therefore,

$$\psi_{(k1+1)+n-1} = P(u_{k1}, 0) = r^* \tag{57}$$

and

$$du_{(k1+1)+n} = R(r^*, r^*) = 0 \tag{58}$$

as desired. The memory prevents the controller from compensating multiple times for the same error.

In practice, however, this controller is not robust to modeling errors. Figure 48, plot B, shows this controller tracking a sinusoid when the plant is much stiffer than the model (the nonlinear controller reduces to this design for K = 1). The controller is too aggressive. The opposite case is shown in Figure 49, plot C; in this case the model is much stiffer than the plant. A model that is too stiff only causes tracking errors. Thus, it is desirable to have

$$P(\Delta, 0) \geq P_a(\Delta, 0) \quad \text{for all } \Delta. \tag{59}$$

6.8.8 Design #3 - Reducing the Closed Loop Gain

The second design was too aggressive when the plant was stiffer than the model. In addition to this problem, there will generally be noise in the measured force signal (the actual noise will vary depending of the grinder, grit size, disk out-of-round, and other factors). The proposed solution is to reduce the closed loop gain. Replacing Ψ_{k+n-1} by $K\Psi_{k+n-1}$ in design #2, however, is not desirable because a steady state error will result. Consider the example problem without the disturbance. The system is in equillibrium when

$$du_{k+1} = du_{k+2} = \ldots = du_{k+n} = 0 \tag{60}$$

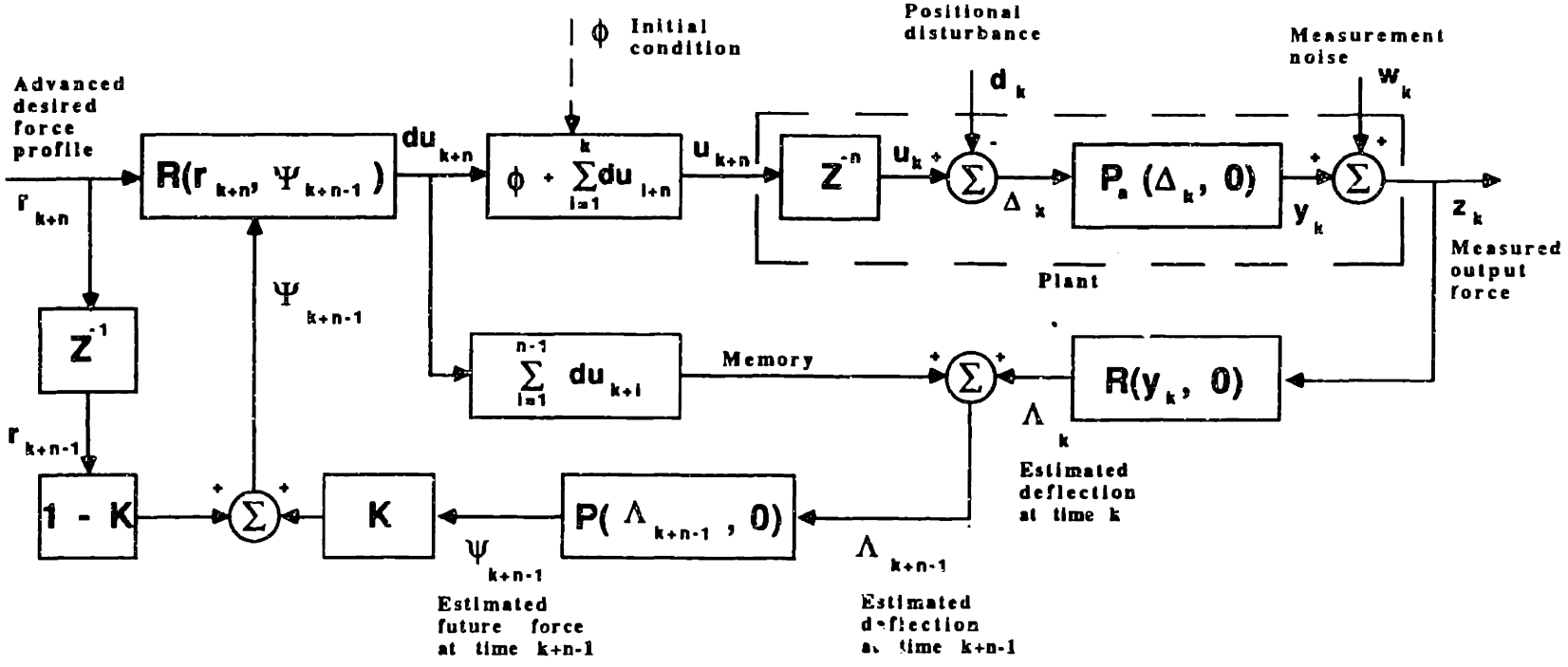

Figure 50. Block diagram of nonlinear controller

thus,

$$du_{k+n} = R(r^*, k\Psi_{k+n-1}) = 0. \tag{61}$$

Therefore,

$$r^* \neq y_k, \tag{62}$$

which implies there is a steady state error.

The nonlinear controller used in this work is given by

$$du_{k+n} = R(r_{k+n}, \Psi_{k+n-1}) \tag{63}$$

$$u_{k+n} = \phi + \sum_{i=1}^{n-1} du_{i+n}.$$

where,

$$\Psi_{k+n-1} = (1 - K) r_{k+n-1} + K\Psi_{k+n-1}$$

and

K is the feedback controller gain.

For the example problem without the disturbance, this design will not have a steady state error. As before, at steady state

$$du_{k+n} = R(r^*, k\Psi_{k+n-1}) = 0. \tag{64}$$

Therefore,

$$(1 - K)r^* + K\psi_{k+n-1} = r^*, \tag{65}$$

and

$$\psi_{k+n-1} = y_k = r^*. \tag{66}$$

In general, the choice of the value of K depends on the modeling errors, the measurement noise, the expected positional disturbances, and the specifications for the system. For example, consider Figure 48, plot A, and Figure 49, plot B. The lower value of K decreased the oscillations for the case when the plant is stiffer then the model, but increased the tracking error for the case when the model is stiffer than the plant. Therefore, there is a performance trade-off that must be made in the choice of K.

For the actual laboratory system in this work, K was chosen by trial and error. A sinusoidal input was tried and K was increased until the tracking error was removed. Then, K was increased further until the magnitude of the output noise became unacceptable. The range of acceptable values for K was found to be $0.1 < K < 0.2$. The value of 0.14 was chosen as the best compromise.

This controller will have a steady state error to a step input if there is a modeling error. The effect of a modeling error on a step

response is shown in Figure 51. However, for the system used in this work, it was possible to model the compliance well enough so that the steady state errors were of the same order of magnitude as the noise.

This controller is an integrating controller. As was discussed for the PI controller, if there is no initial contact and there is a nonzero desired force then this controller continues to move the end effector of the robot until contact is made with the workpiece (the controller seeks a force).

For the current system, P and R must be defined in general so that the controller will operate properly for positive and negative forces. $P(\Delta, 0)$ is given by

$$\begin{aligned} &(b/a)\,(\exp(a\Delta) - 1) && \Delta \geq 0 \\ &-(b/a)\,(\exp(-a\Delta) - 1) && \Delta < 0. \end{aligned} \tag{67}$$

$R(v_2, v_1)$ is given by

$$\begin{aligned} &(1/a)\ln[(av_2 + b)/(av_1 + b)] && v_2, v_1 \geq 0 \\ &(1/a)\ln[(b - av_2)/(b - av_1)] && v_2, v_1 < 0 \\ &(1/a)\ln[(av_2 + b)(b - av_1)/b^2] && v_2 \geq 0, v_1 < 0 \\ &(1/a)\ln[(b - av_2)(b - av_1)/b^2] && v_2 < 0, v_1 \geq 0. \end{aligned} \tag{68}$$

The controller equations, for the PUMA robot, are summarized as

$$
\begin{aligned}
u_{k+5} &= \phi + \sum_{i=1}^{n-1} du_{i+5} \\
du_k &= R(r_{k+5}, \Psi_{k+4}) \\
\Psi_{k+4} &= (1 - K)\, r_{k+4} + K\Psi_{k+4} \\
\psi_{k+4} &= P(\Lambda_{k+4}, 0) \\
\Lambda_{k+4} &= \Lambda_k + du_{k-4} + du_{k-3} + du_{k-2} + du_{k-1} \\
\Lambda_k &= R(z_k, 0), \\
\phi &= du_1 + du_2 + du_3 + du_4.
\end{aligned}
\tag{69}
$$

A final point is that the controller was initialized open loop ($K = 0$) for 5 sampling periods (0.14 s) to allow feedback to start. This was done because the experiments were always started at a known initial condition.

6.8.9 Nonlinear Controller - Experimental Results

The step response for this controller is shown in Figure 52. The response is fast (rise time $\approx$ 0.1 s) and there is little overshoot (overshoot $\approx$ 5%). Comparison with Figure 37 shows that there is more steady state noise, and the output is slightly biased. The bias is due to the modeling error for the compliance. This is an area for improve-

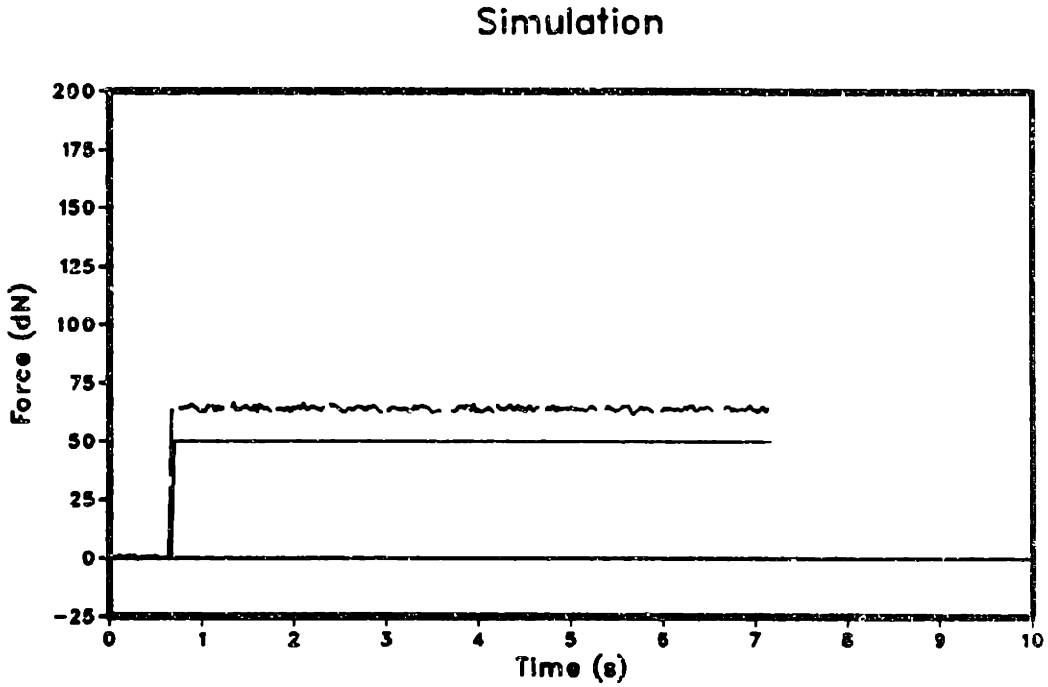

Figure 51. Effect of modeling errors on step response: model(a 0.011, b 0.17), plant(a 0.014, b 0.17)

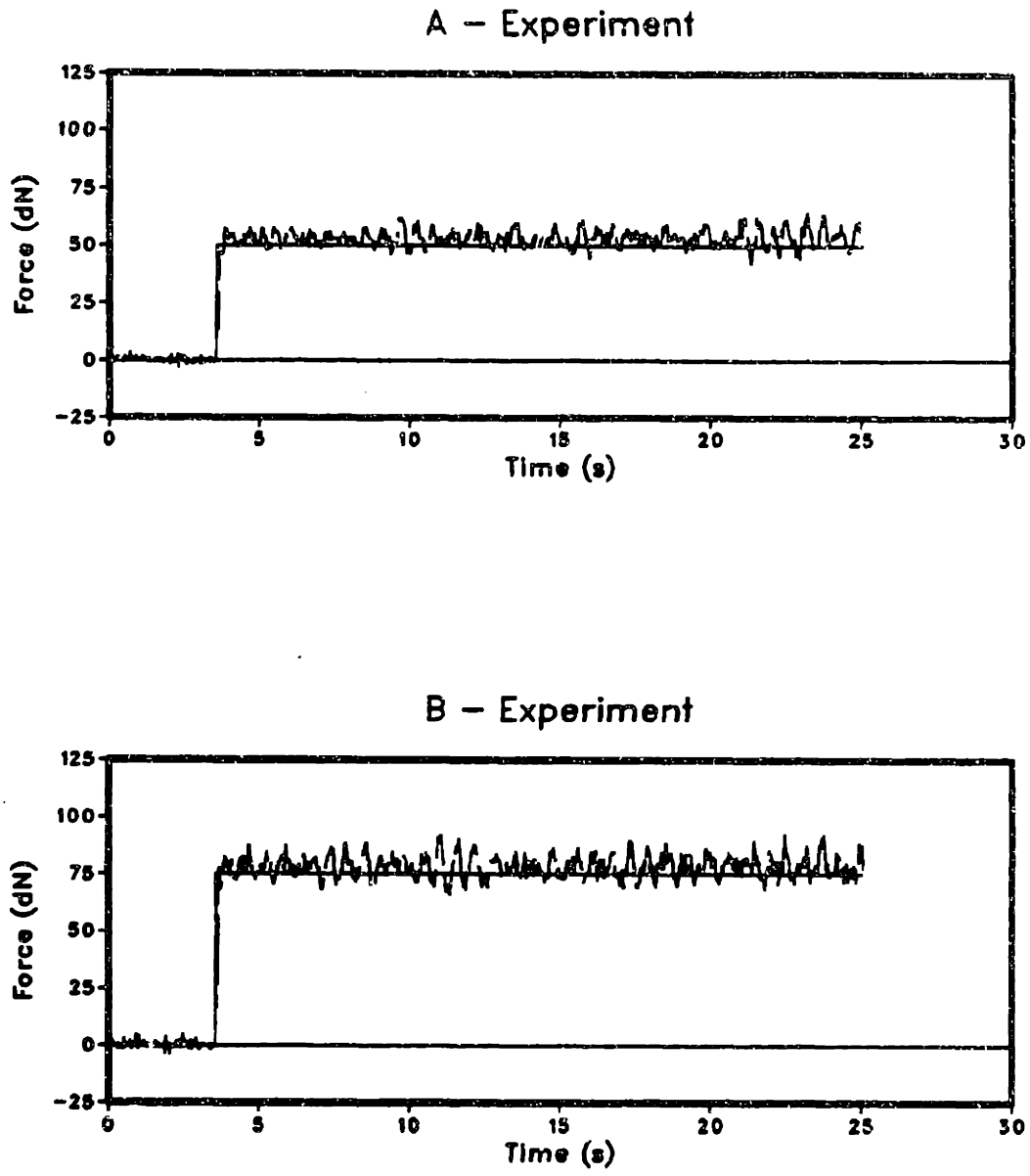

Figure 52. Step response of nonlinear controller: (K 0.14, a 0.012, b 0.2)

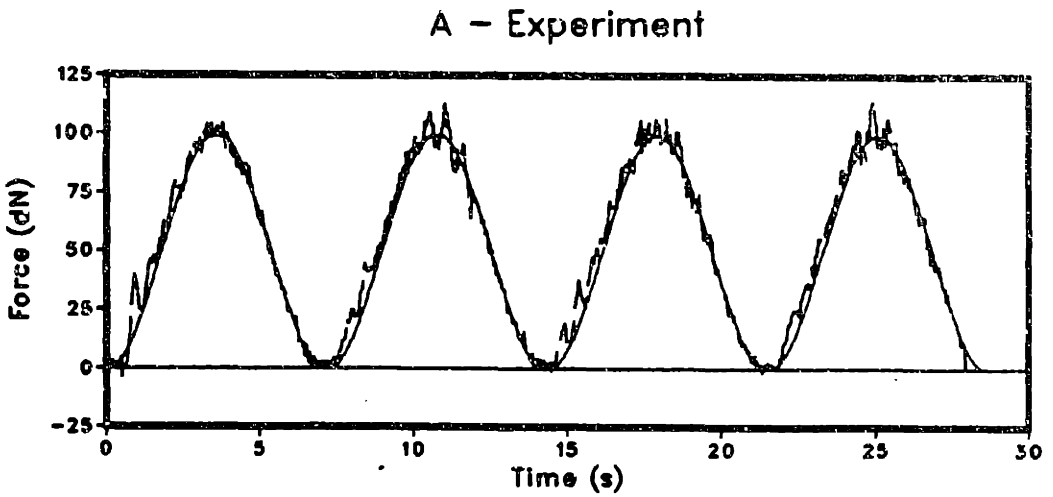

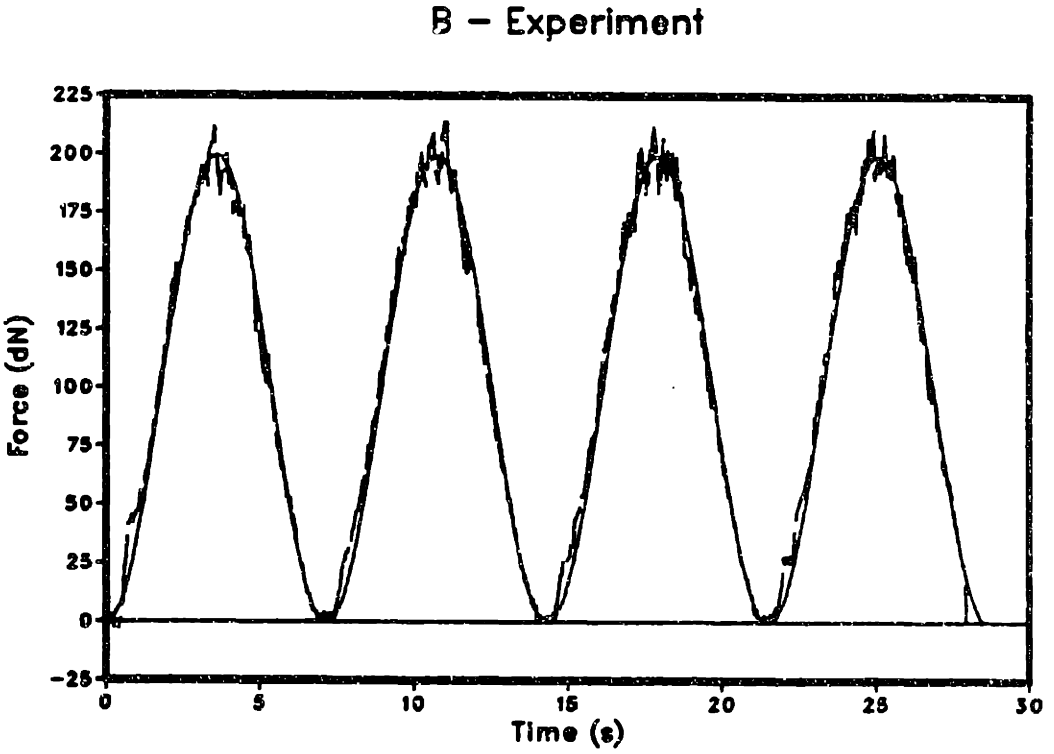

Figure 53. Sinusoidal response of nonlinear controller (100 & 200 dN max.): (0.14 Hz, K 0.14, a 0.011, b 0.17)

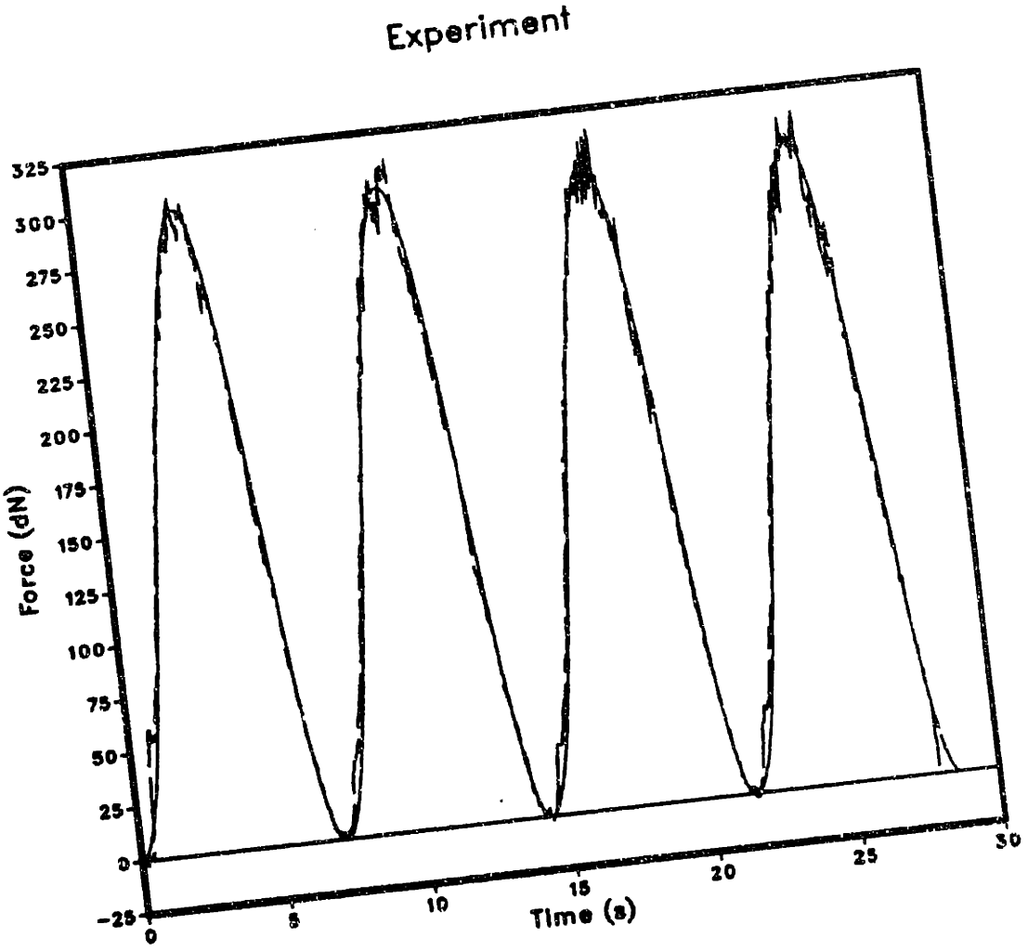

Figure 54. Sinusoidal response of nonlinear controller (300 dN max.): (0.14 Hz, K 0.14, a 0.011, b 0.17)

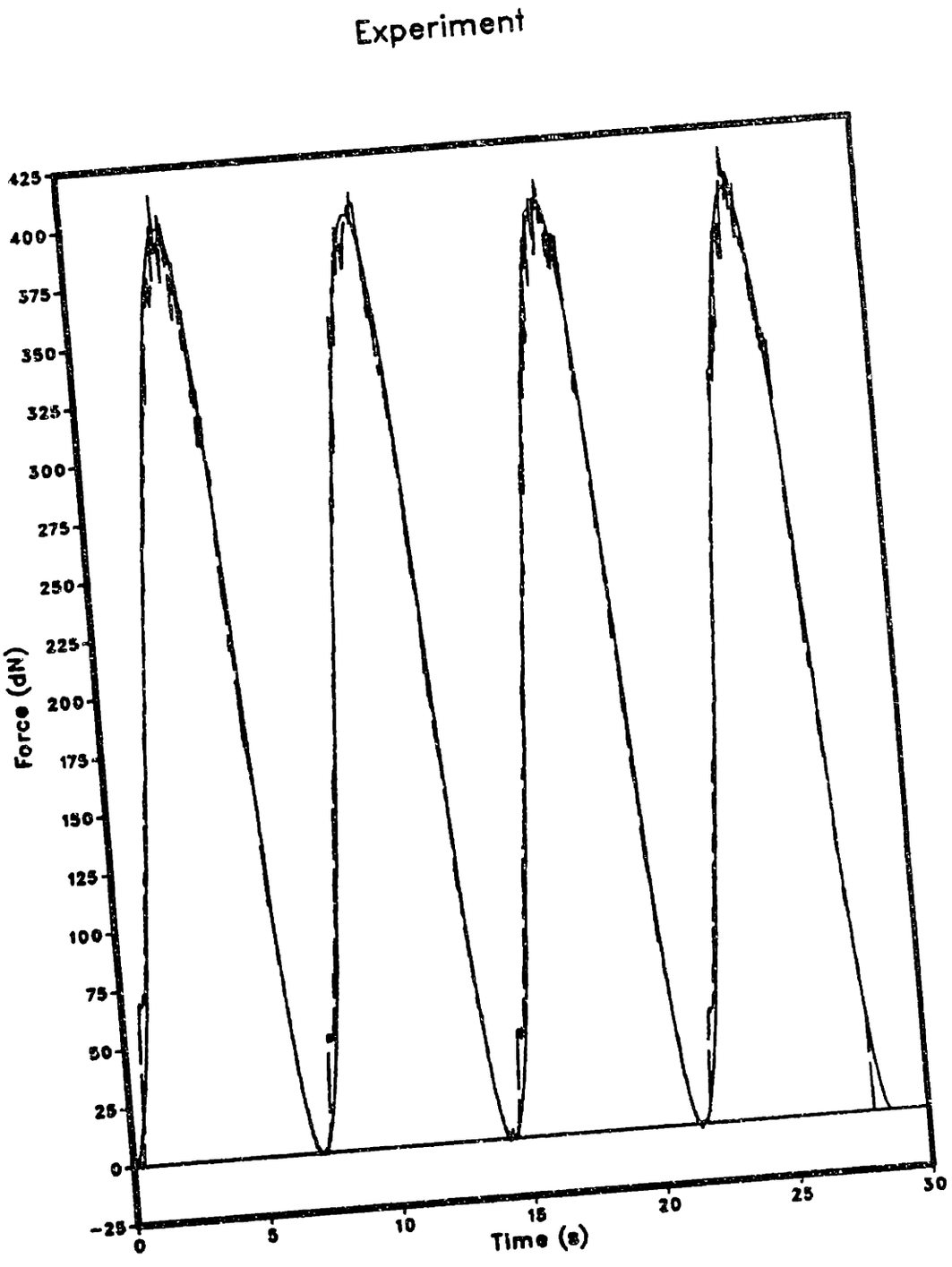

Figure 55. Sinusoidal response of nonlinear controller (400 dN max.): (0.14 Hz, K 0.14, a 0.011, b 0.17)

ment, but the difference between this response and the response in Figure 37 is not considered significant.

Figure 53, 54, and 55 show the sinusoidal response of the controller. There is no phase lag and the response remains stable up to 400 dN of commanded force. Higher forces were not tried in order to protect the hardware. Tracking at high forces is better than the previous design, for which tracking deteriorated at 325 dN. Figure 56 shows the response to offset sinusoids. The controller is able to catch up to the input and continue tracking.

The ability to track a sinusoid while rejecting a -5% ramp disturbance is illustrated in Figure 57, 58, and 59. Disturbance rejection is one of the most important improvements over the previous controllers. Although there are some oscillations on the rising edge of the output force, the controller remains stable up to 400 dN. Like a PI controller, this controller always has a positive steady state error rejecting a negative ramp and a negative steady state error rejecting a positive ramp. The controller rejecting a +5% ramp is shown in Figure 60. Plot A clearly shows the negative steady state error while regulating a constant force. A 400 dN sinusoidal input, tracking a +5% ramp, is shown in Figure 61. Positive ramps cause steady state errors, but do not cause oscillations. Negative ramps during a rising input signal are the hardest to reject. This situation causes some oscillation. Figure 62,

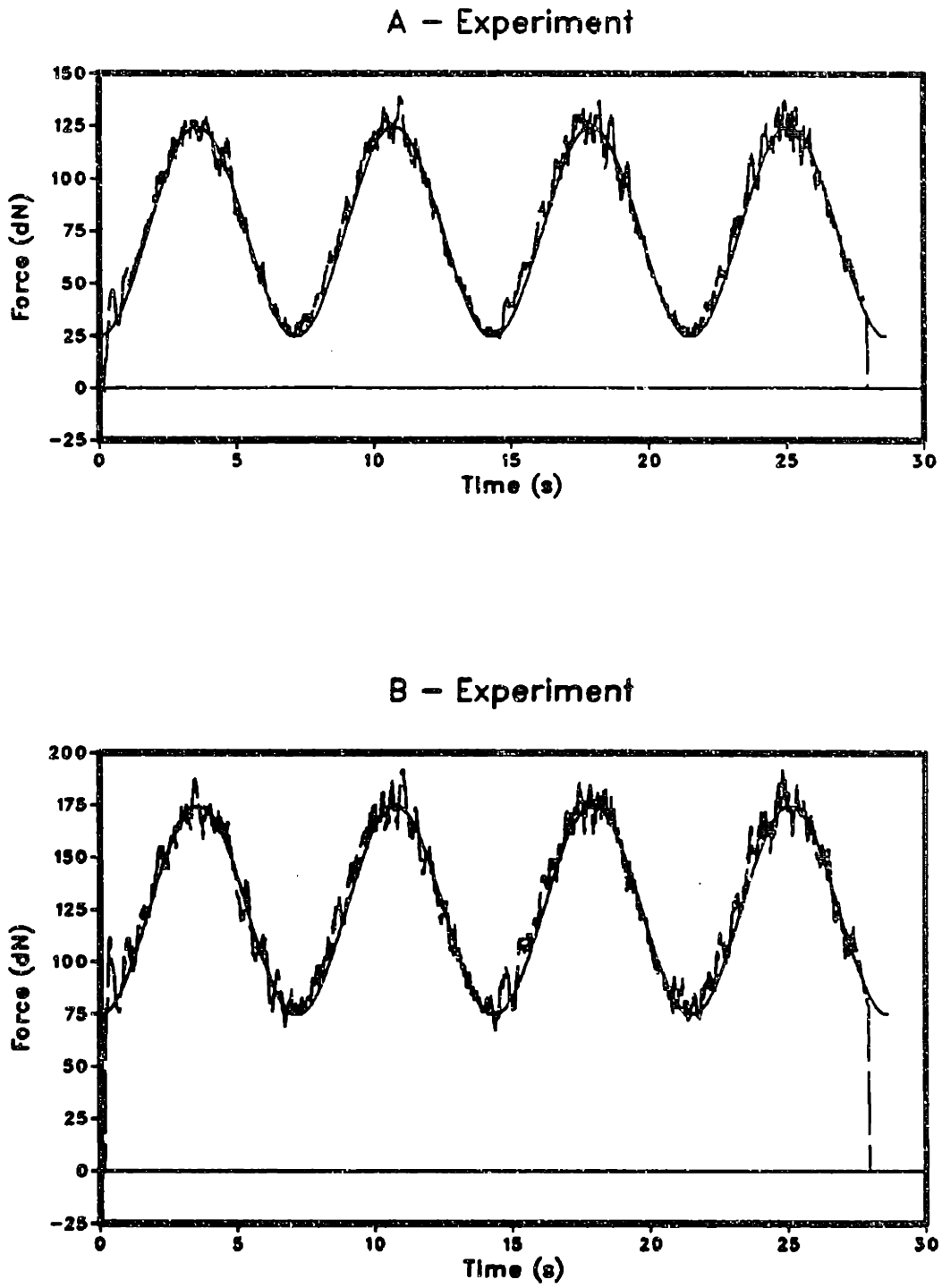

Figure 56. Response on nonlinear controller to offset sinusoids: (0.14 Hz, K 0.14, a 0.012, b 0.2)

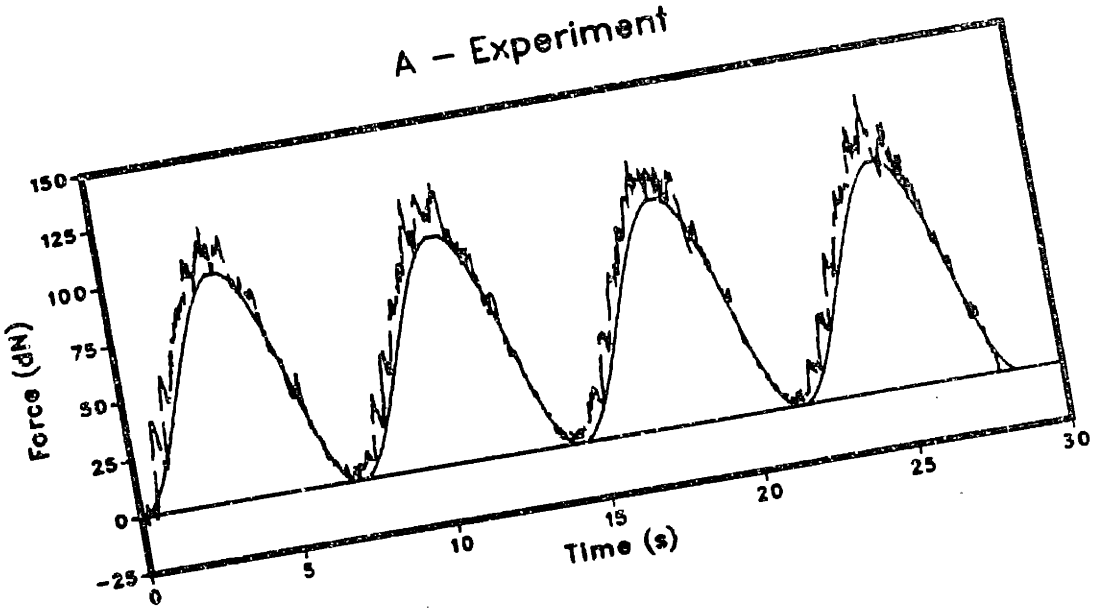

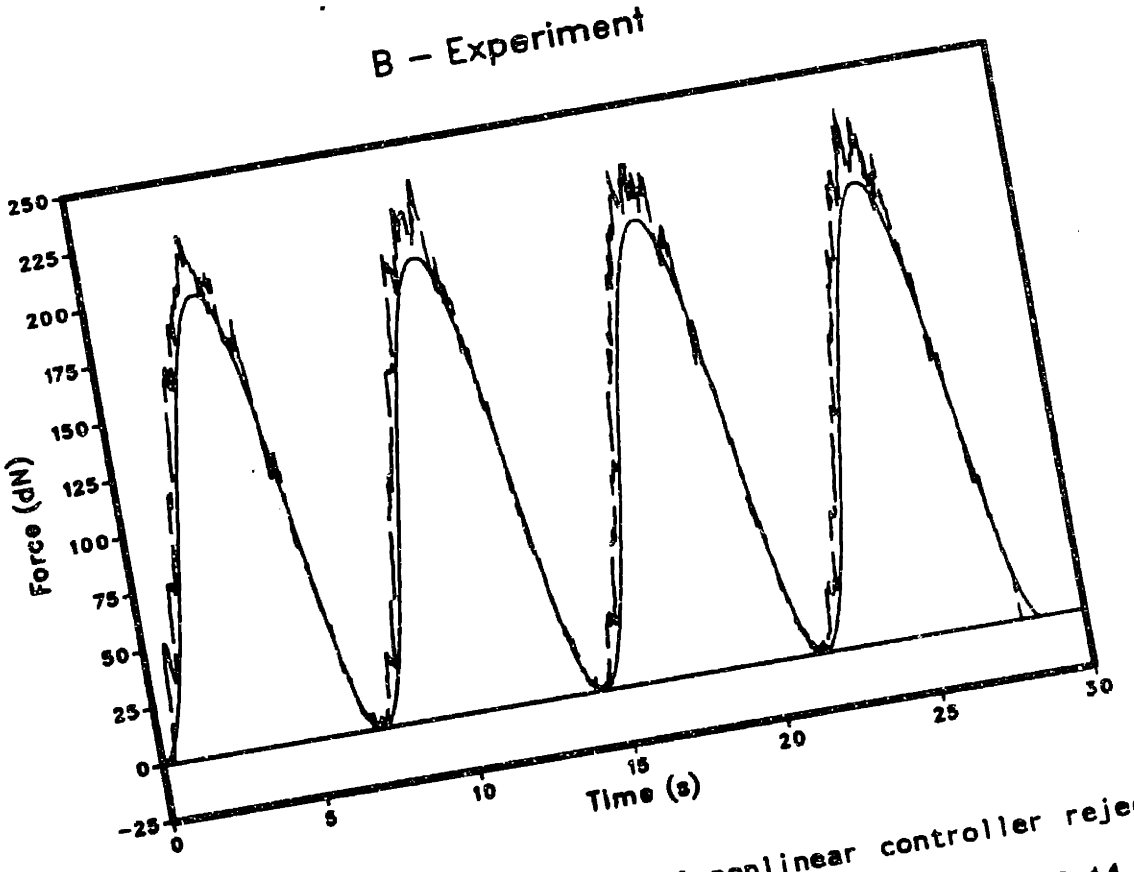

Figure 57. Sinusoidal response of nonlinear controller rejecting a -5% ramp disturbance (100 & 200 dN max.): 0.14 Hz, A - (K 0.14, a 0.012, b 0.2) B - (K 0.14, a 0.011, b 0.17)

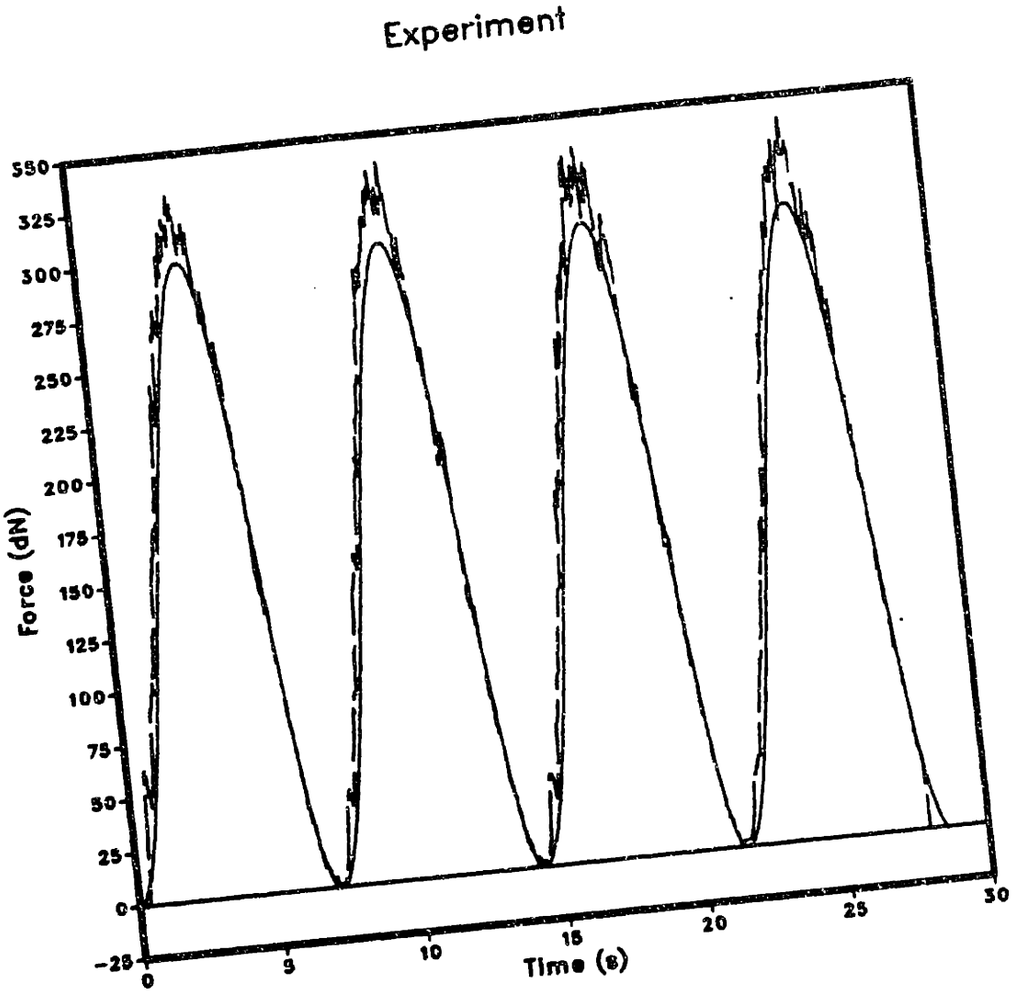

Figure 58. Sinuscidal response of nonlinear controller rejecting a -5% ramp disturbance (300 dN max.): (0.14 Hz, K 0.14, a 0.011, b 0.17)

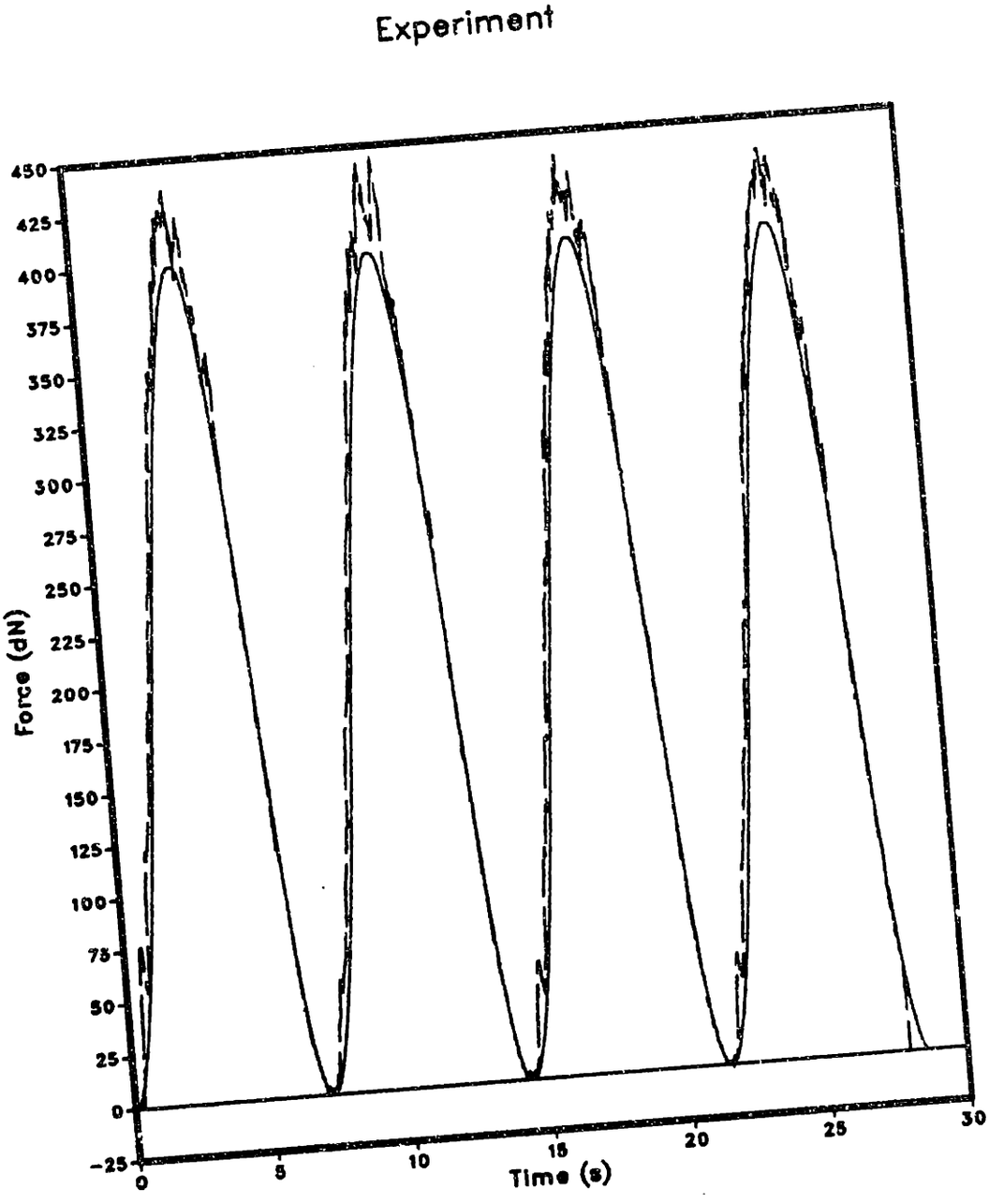

Figure 59. Sinusoidal response of nonlinear controller rejecting a -5% ramp disturbance (400 dN max.): (0.14 Hz, K 0.14, a 0.011, b 0.17)

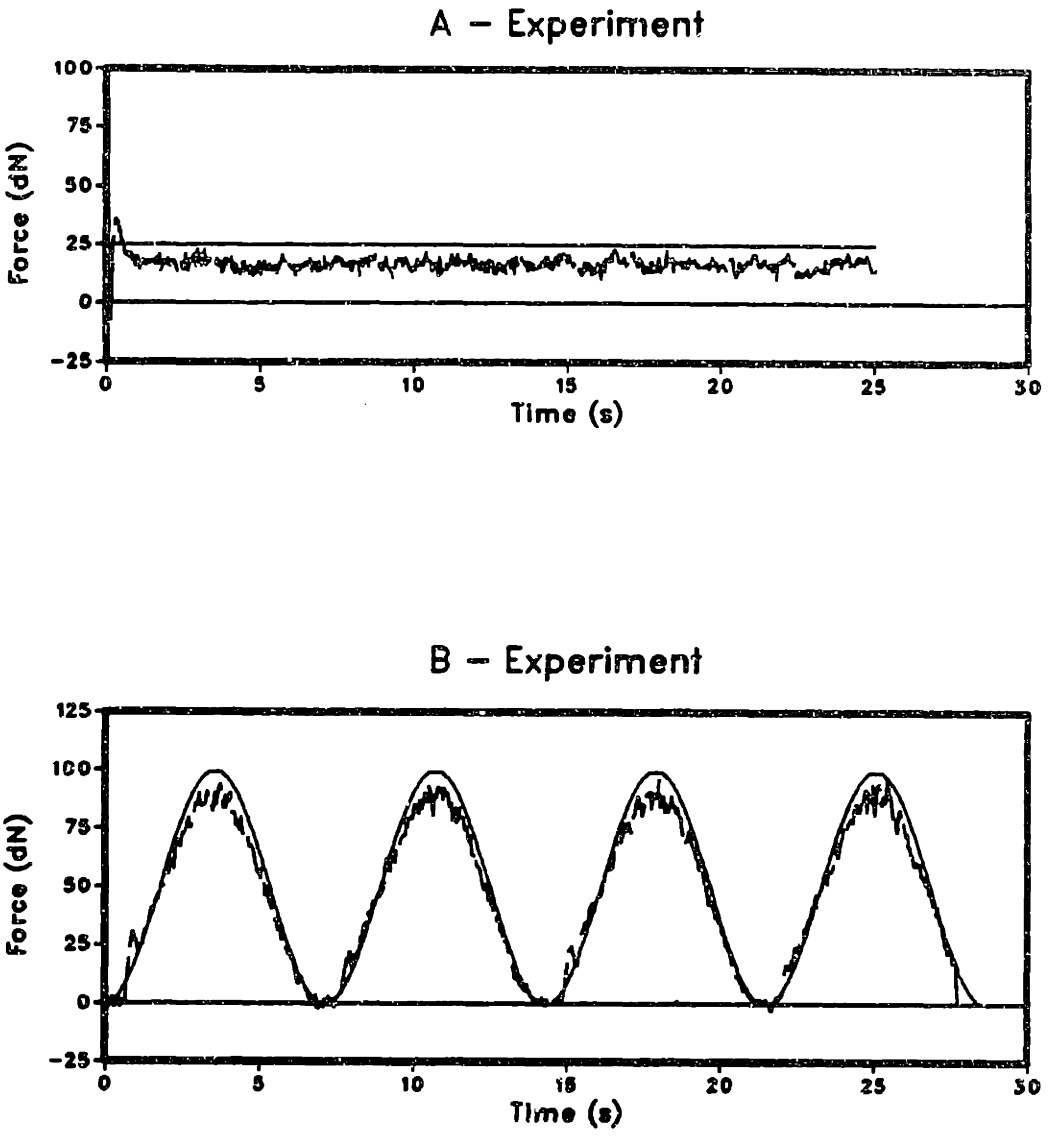

Figure 60. Step and sinusoidal (100 dN max.) response on nonlinear controller rejecting a +5% ramp disturbance: (K 0.14, a 0.012, b 0.2) A - regulating 25 dN B - tracking 0.14 Hz sinusoid

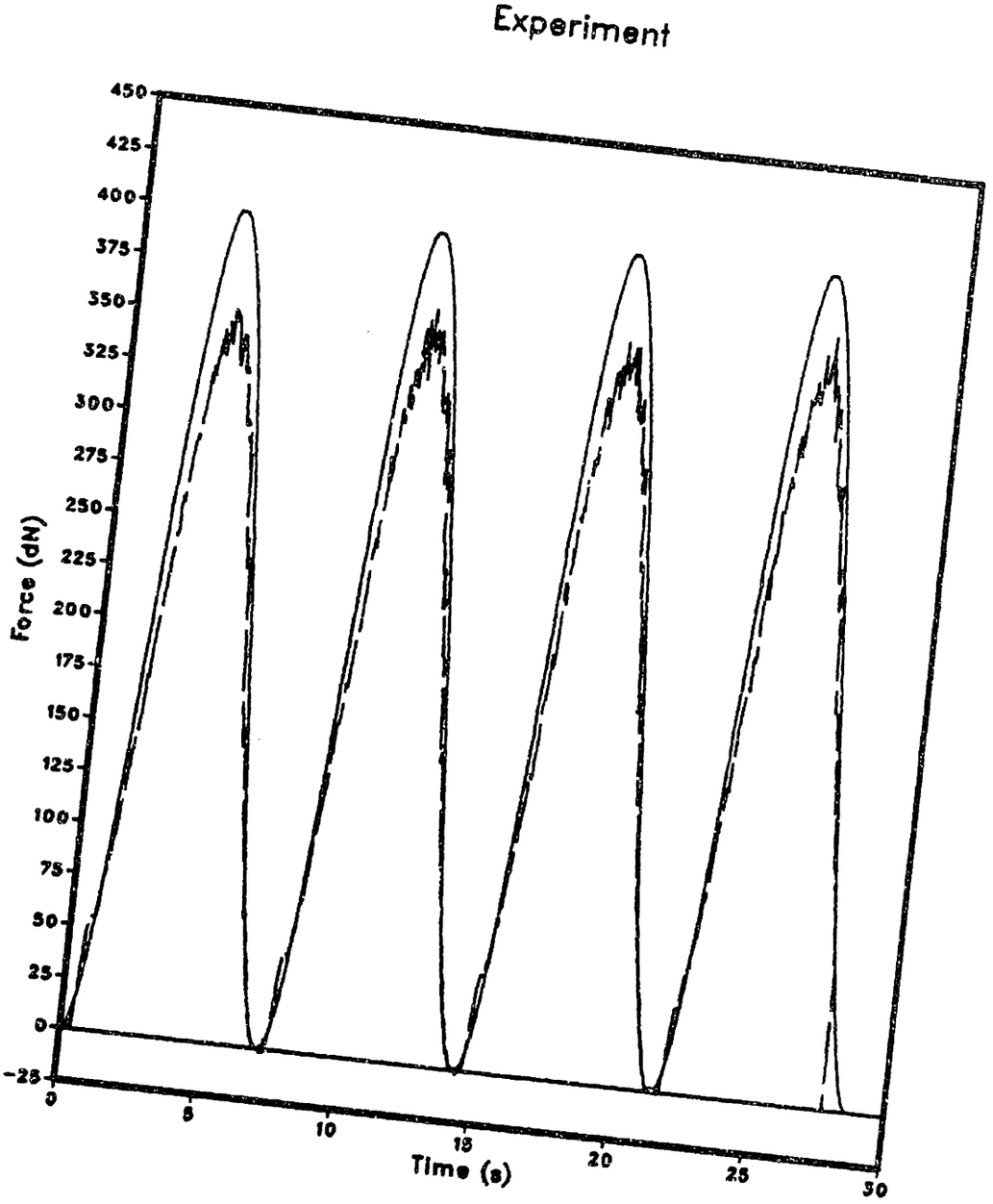

Figure 61. Sinusoidal response of nonlinear controller rejecting a +5% ramp disturbance (400 dN max.): (0.14 Hz, K 0.14, a 0.012, b 0.2)

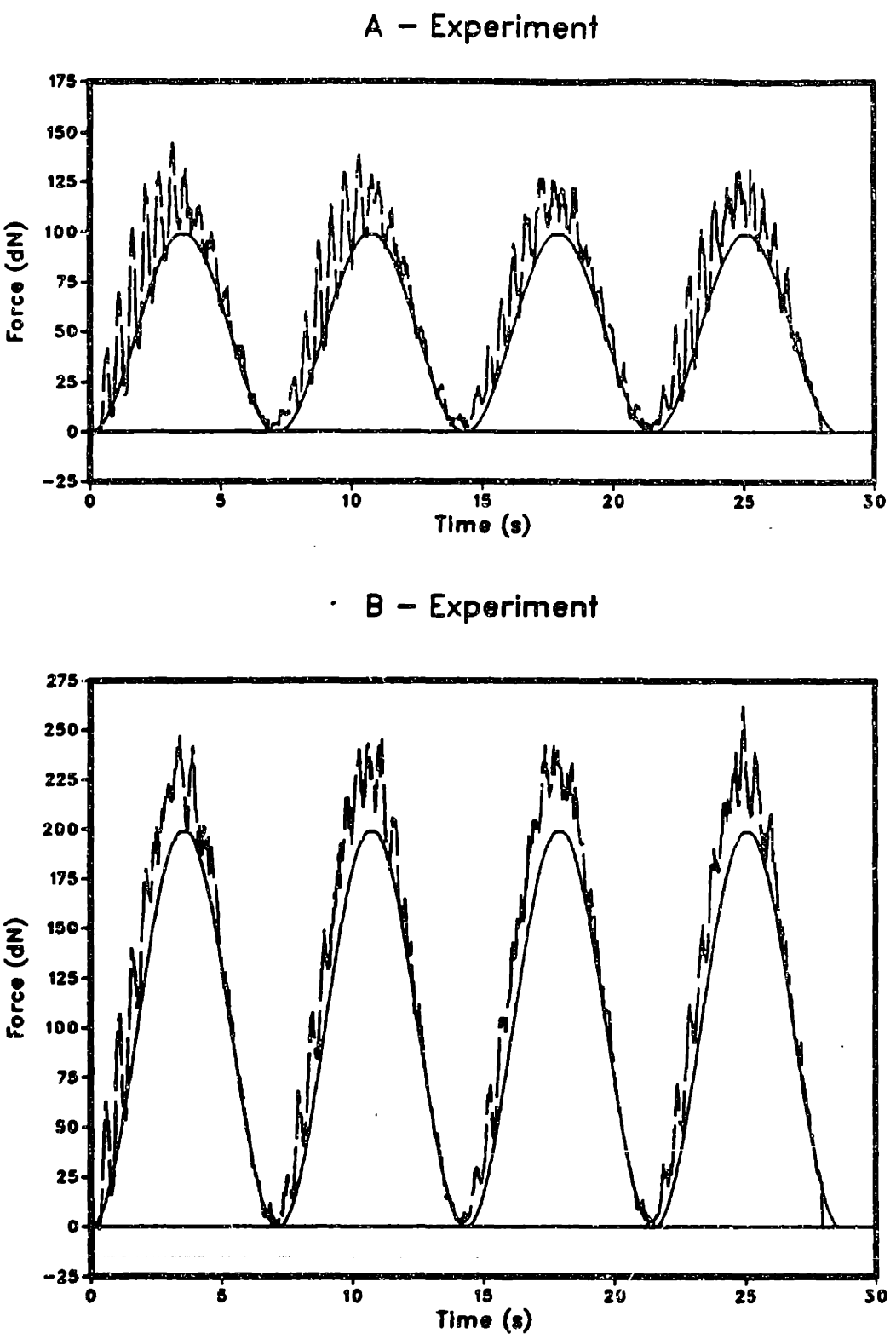

Figure 62. Sinusoidal response of nonlinear controller rejecting a -10% ramp disturbance (100 & 200 dN max.): 0.14 Hz, A - (K 0.14, a 0.011, b 0.17) B - (K 0.14, a 0.012, b 0.2)

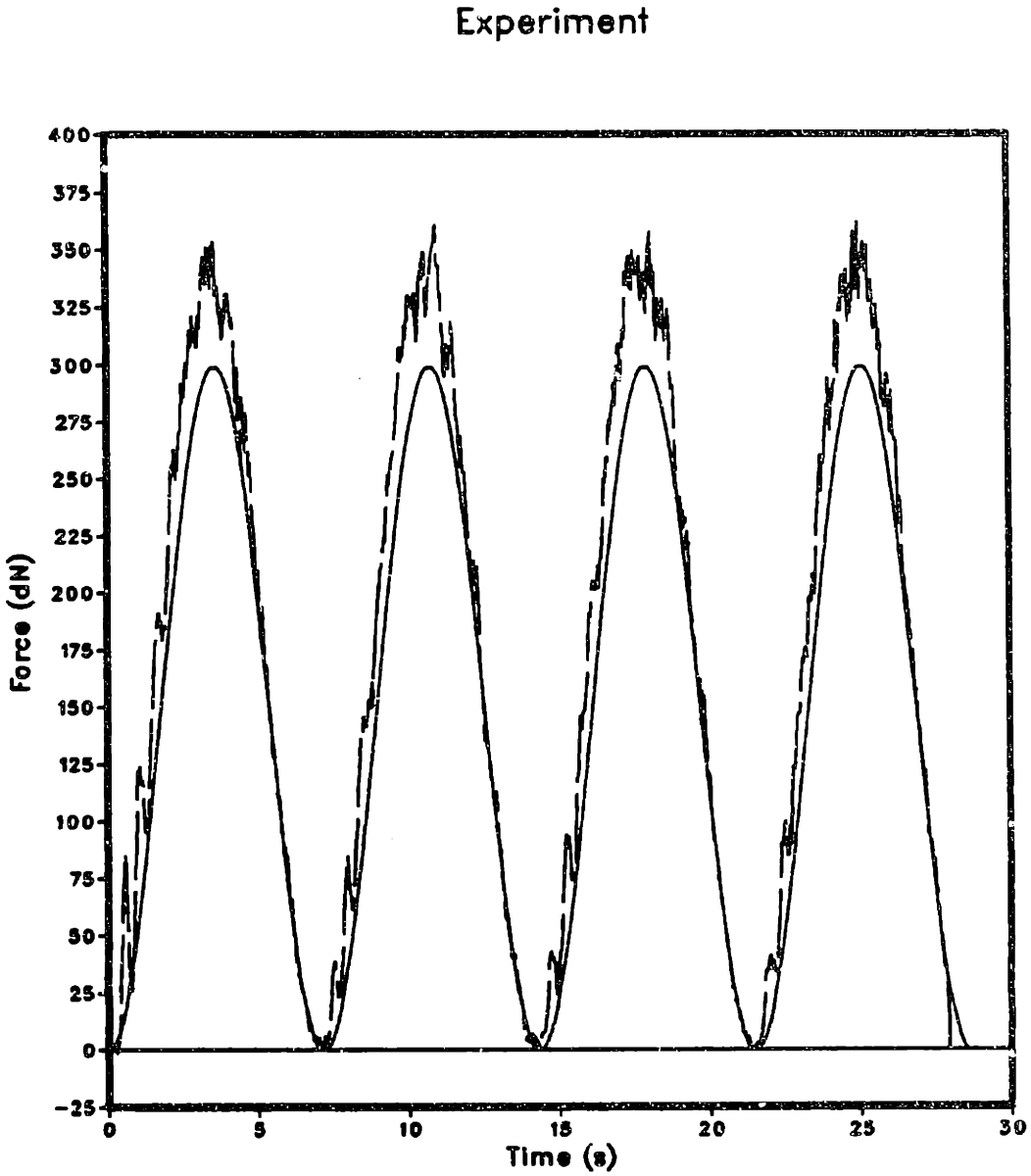

Figure 63. Sinusoidal response of nonlinear controller rejecting a -10% ramp disturbance (300 dN max.): (0.14 Hz, K 0.14, a 0.012, b 0.2)

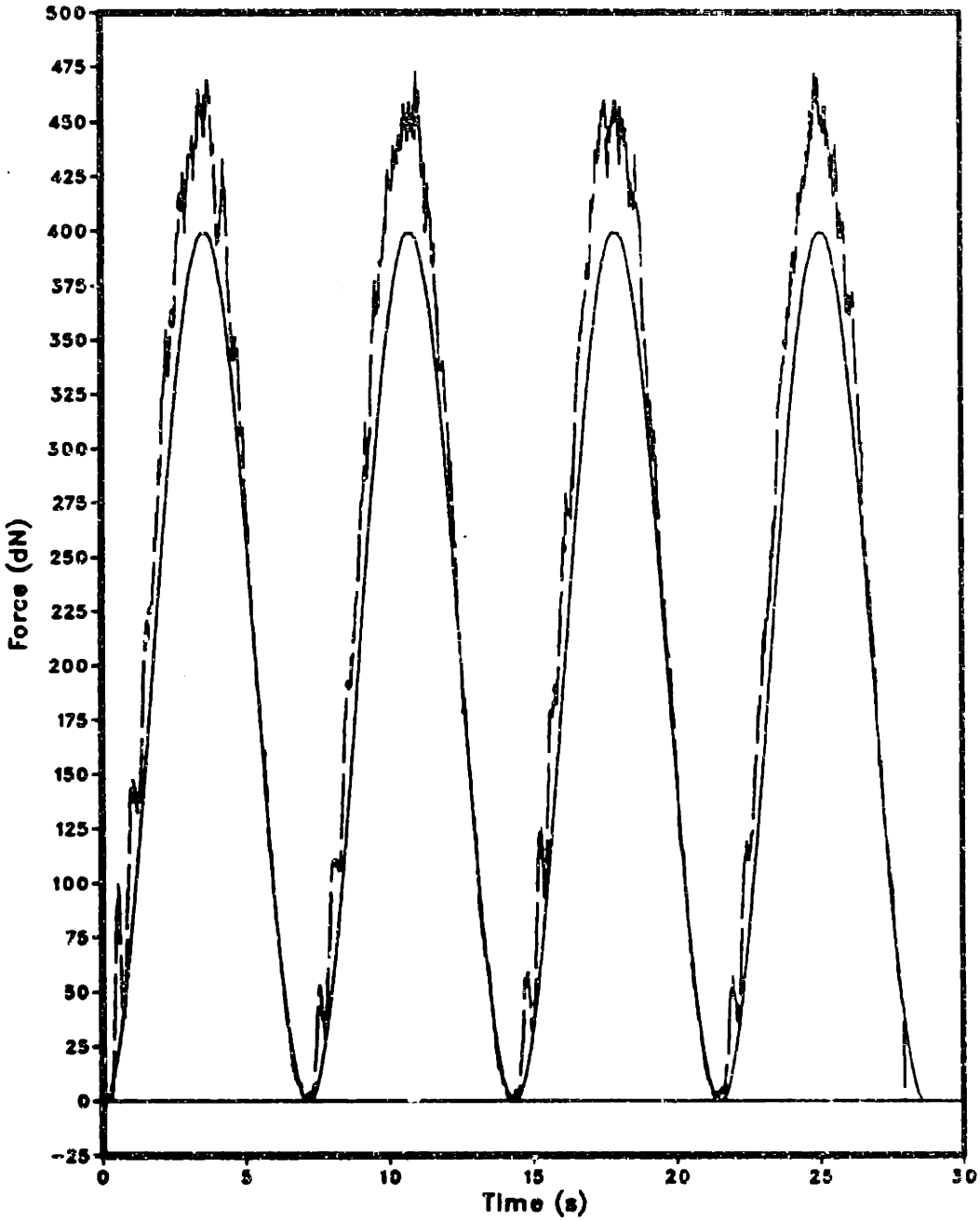

Figure 64. Sinusoidal response of nonlinear controller rejecting a -10% ramp disturbance (400 dN max.): (0.14 Hz, K 0.14, a 0.012, b 0.2)

63, and 64 illustrate the controller tracking a sinusoid while rejecting a -10% ramp. The oscillations and tracking error increase on the rising edge, but the controller remains stable up to 400 dN. A -15% ramp is shown in Figure 65, 66, and 67. Although there are large force variations in the force response, the positional movements of the robot were small. No high frequency shaking was observed.

The response of the controller for increasing input frequency is illustrated in Figure 68, 69, and 70. These plots show the responses for sinusoids of frequency 0.28, 0.56, 1.12, and 2.23 Hz. There is no significant phase lag until 2.23 Hz. The magnitude response tends to be high for input frequencies above 0.56 Hz; this is another area for improvement.

The ability of the controller to reject the complex disturbance shown in Figure 23 was tested. This contour was two wells in a sequence. The second well was deeper then the first. The robot is shown starting down the second well in Figure 23. The oscillations shown in the middle of Figure 71 occured when the robot was negotiating the first rising edge. Then as the disk crossed the peak in the middle and began down the steeper well, a negative steady state error began. The rise of the second well was more than a 15% grade. At the end of the experiment the contour contacted the center of the disk. The compliance model is not valid for this type of contact. This caused the

three force peaks at the end of the experiment. The sinusoidal response is shown in Figure 72. The force peaks at the end are more pronounced. Although it is difficult to tell from the figure, the tool-z motion of the robot was small. Contact in the center caused the force to rise quickly. In response, the robot would pull back about 1 cm. (sometimes losing contact), and then continued trying to track the input force profile.

This controller had stable responses for a wide range of inputs. The controller was able to track a sinusoid with a peak force of 400 dN. Disturbance rejection properties are significantly better then previously tested controllers. Steady state errors occur for first order disturbances. Steady state errors also occur if there are modeling errors.

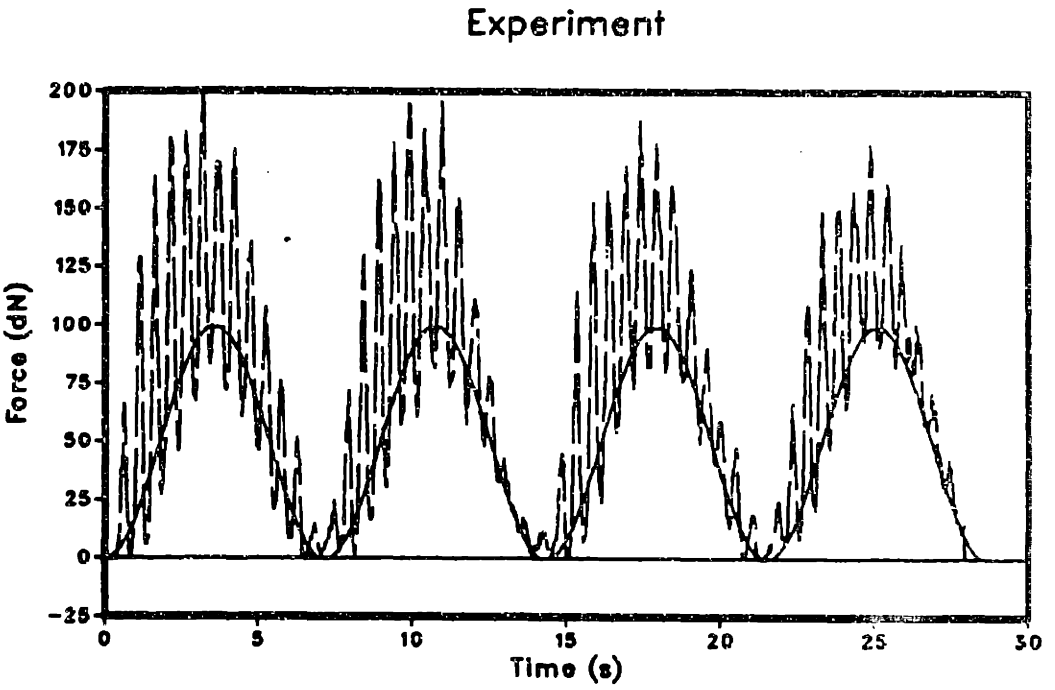

Figure 65. Sinusoidal response of nonlinear controller rejecting a -15% ramp disturbance (100 dN max.): (0.14 Hz, K 0.14, a 0.012, b 0.2)

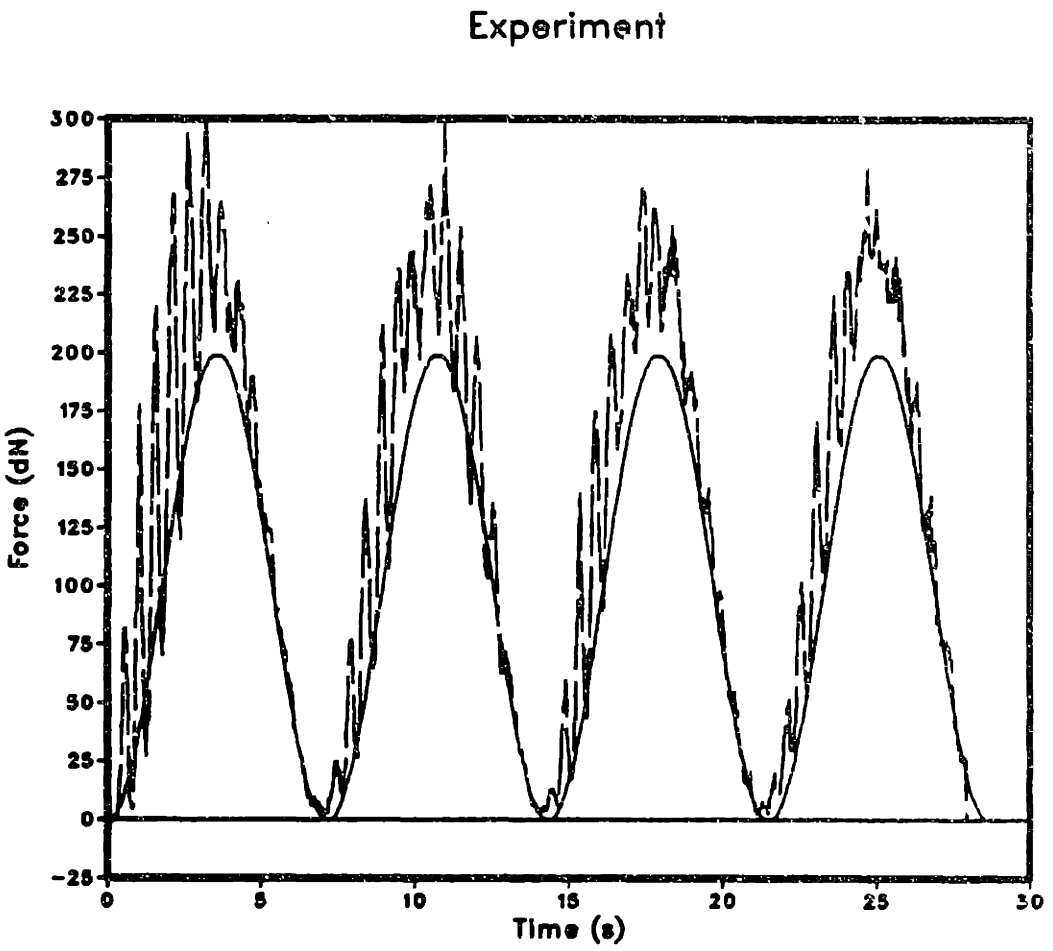

Figure 66. Sinusoidal response of nonlinear controller rejecting a -15% ramp disturbance (200 dN max.): (0.14 Hz, K 0.14, a 0.012, b 0.2)

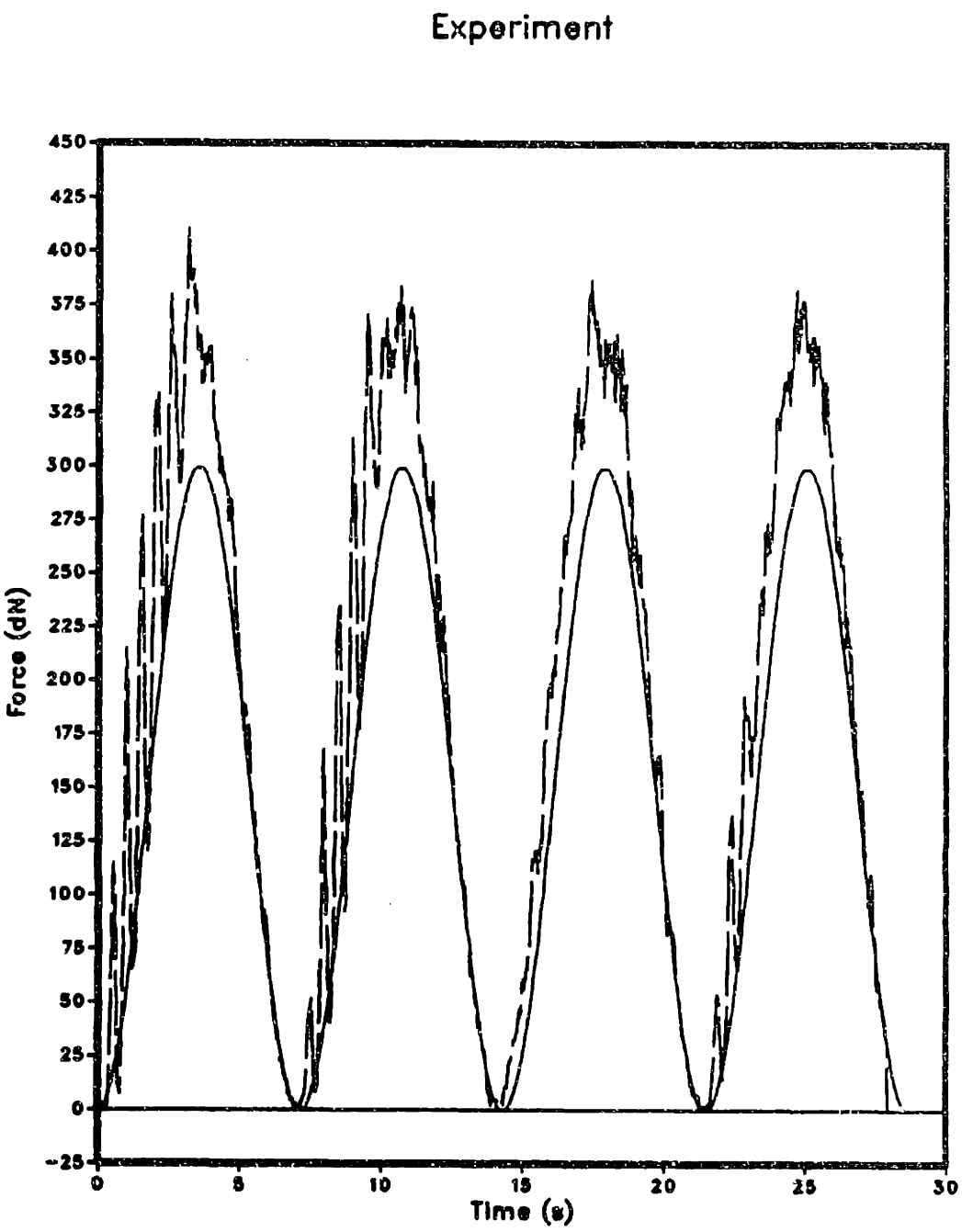

Figure 67. Sinusoidal response of nonlinear controller rejecting a -15% ramp disturbance (300 dN max.): (0.14 Hz, K 0.14, a 0.012, b 0.2)

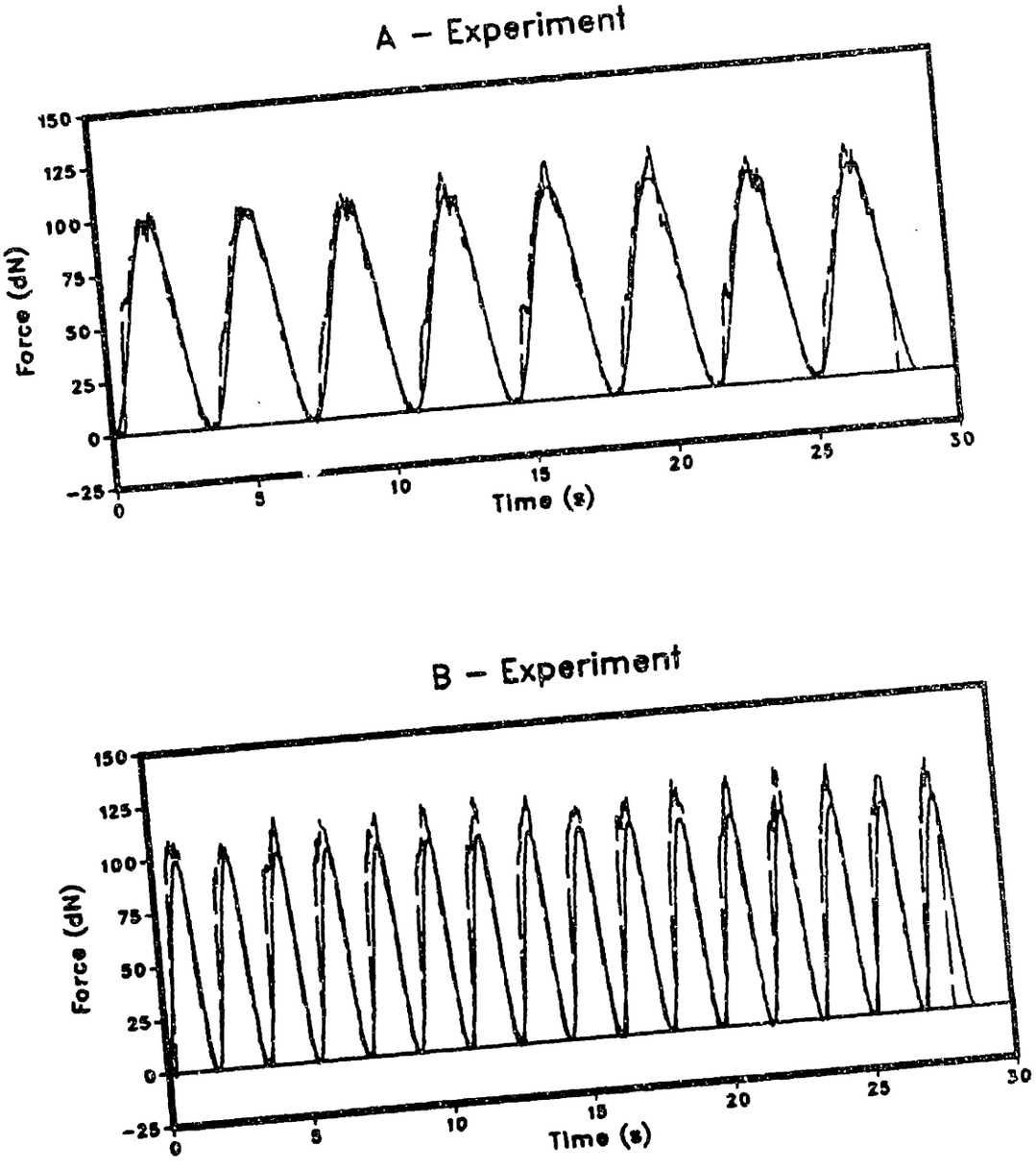

Figure 68. Response of nonlinear controller to 0.28 Hz and 0.56 Hz sinusoids: (K 0.14, a 0.012, b 0.2) A - 0.28 Hz B - 0.56 Hz

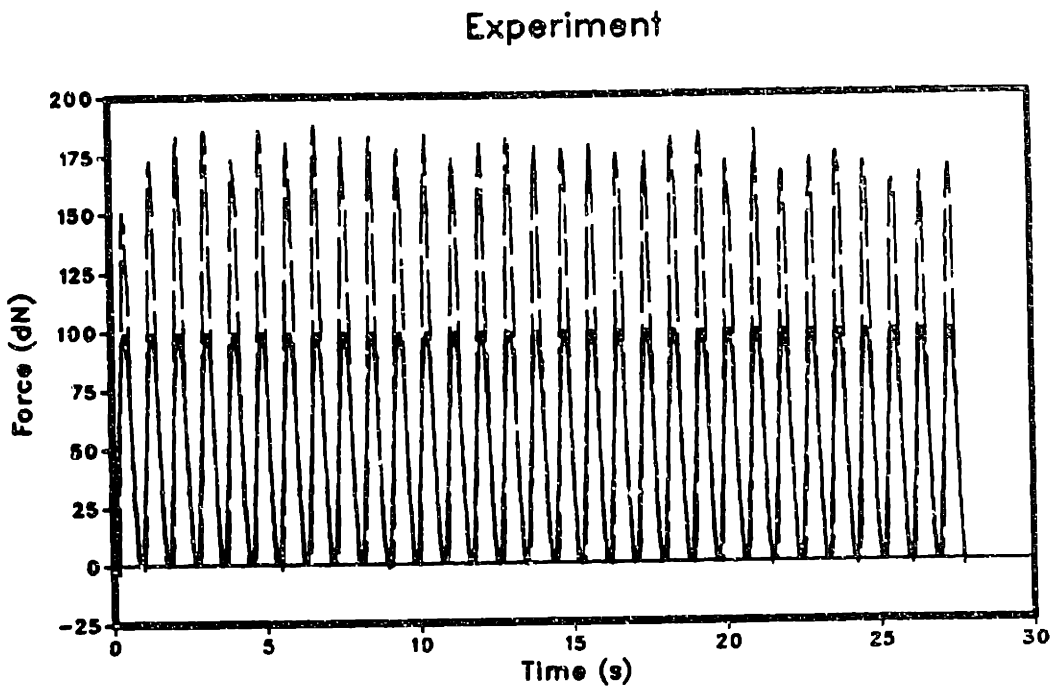

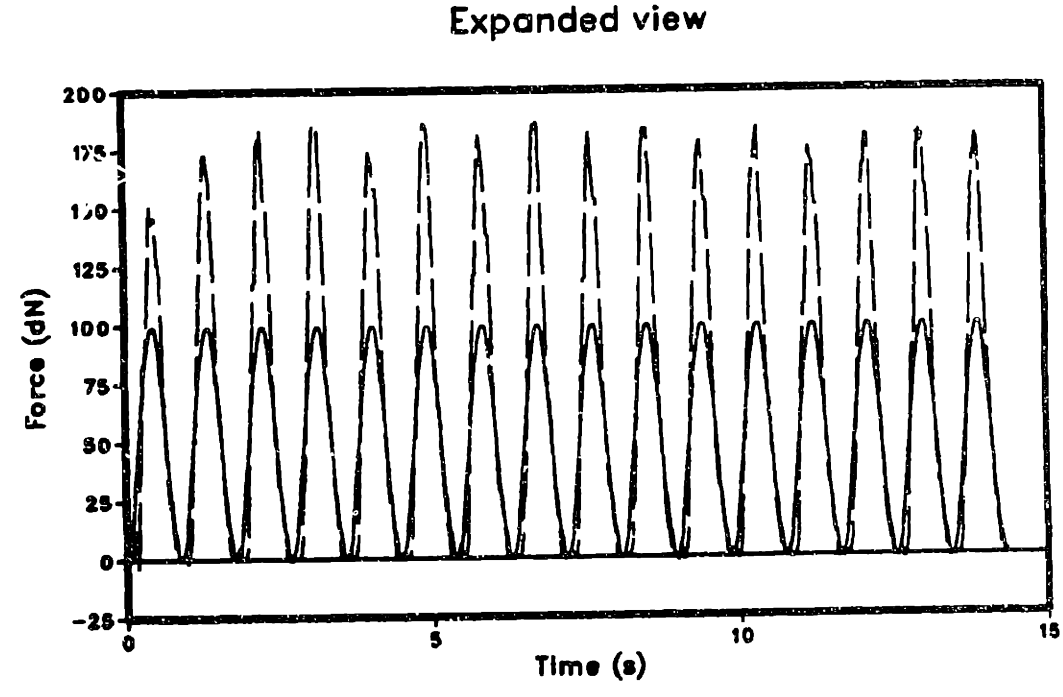

Figure 69. Response of nonlinear controller to 1.12 Hz sinusoid: (1.12 Hz, K 0.14, a 0.012, b 0.2)

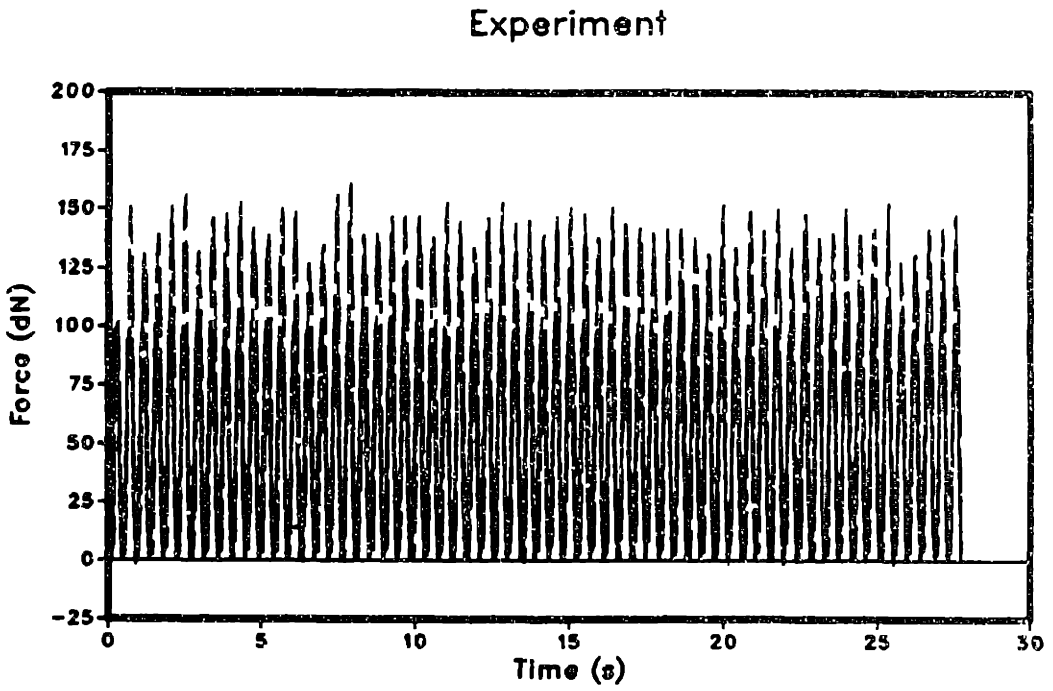

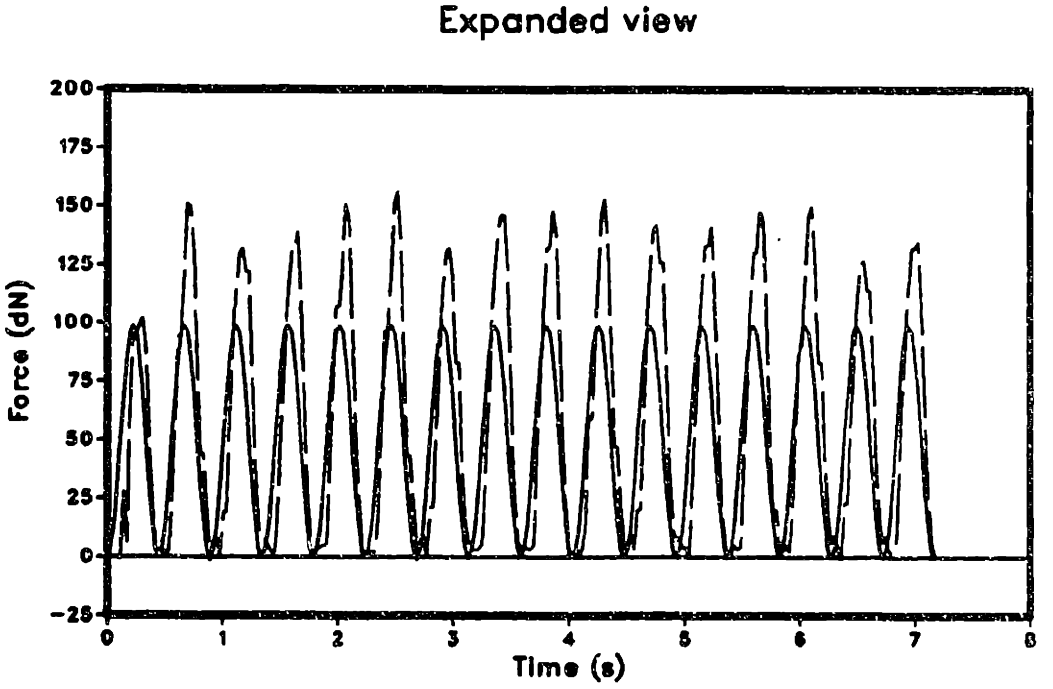

Figure 70. Response of nonlinear controller to 2.23 Hz sinusoid: (2.23 Hz, K 0.14, a 0.012, b 0.2)

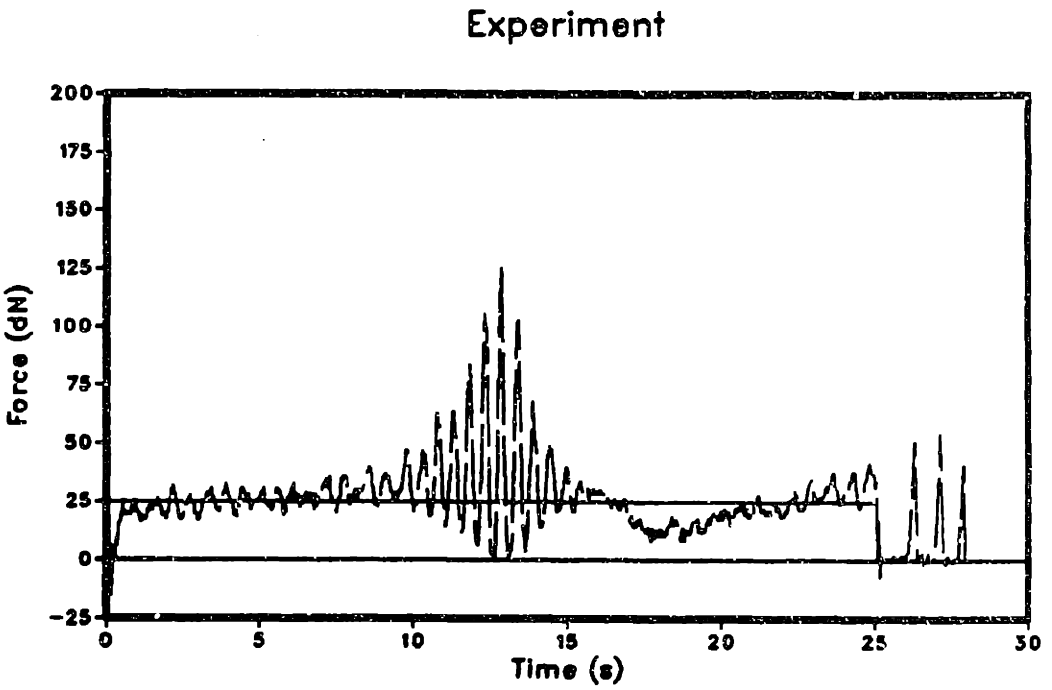

Figure 71. Nonlinear controller regulating 25 dN force while rejecting complex disturbance: (K 0.014, a 0.0.2, b 0.2)

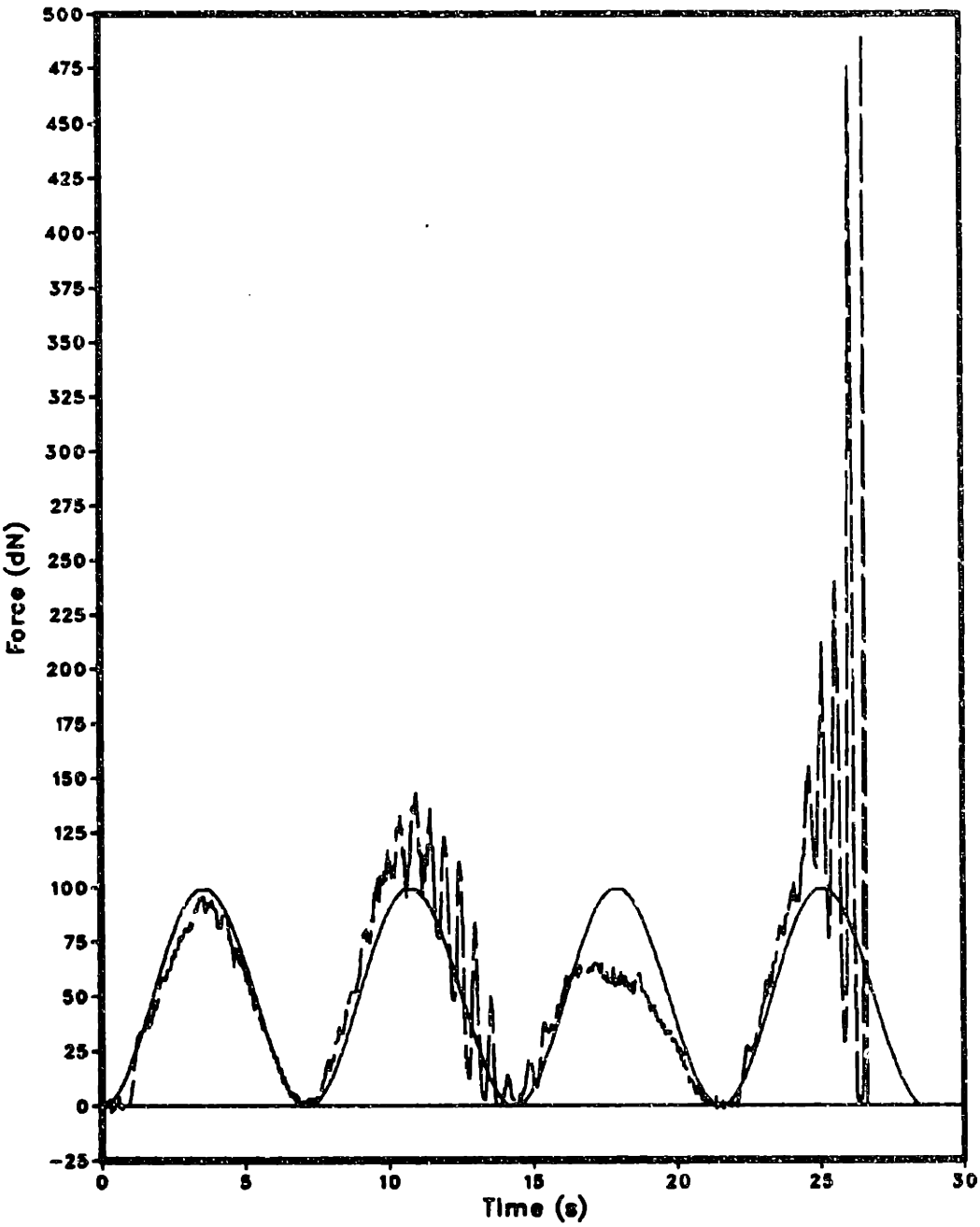

Figure 72. Nonlinear controller tracking sinusoid while rejecting complex disturbance: (0.14 Hz, K 0.014, a 0.0.2, b 0.2)

7.0 CONCLUSIONS AND RECOMMENDATIONS

7.1.1 Conclusions

A time delay is the dominant dynamic characteristic of the PUMA robot and VAL-II up to a bandwidth of 10 Hz. This was established by estimating the frequency response that relates output displacement to input displacement during experiments without workpiece contact. The error between the magnitude response of this time delay model and the actual magnitude response began to increase for frequencies greater than 3 Hz. The actual magnitude response began attenuating as frequency increased. The most likely cause of this attenuation is saturation of the servo drivers. Despite the additional dynamics above 3 Hz, the time delay remained the dominant characteristic. It was also found that geometric and drive train nonlinearities had little effect on the frequency response for the range of inputs tested.

The frequency response was also estimated in experiments with workpiece contact and the results compared with the noncontact case. In these experiments, the frequency response related output force to input displacement. The frequency response remained essentially the same as in the noncontact case. The only difference was that the magnitude

response for frequencies above 3 Hz attenuated more rapidly. This difference was not found to be significant.

The compliance of the PUMA robot with the grinding disk and rubber backing attached was also experimentally determined. The compliance model was combined with the results of the frequency response experiments to form an integrated model of the plant. This model was used to design a force control law.

A number of designs for a force control laws, including proportional and PI controllers, were presented along with experimental and simulated results. Overall, the best performance was achieved using a nonlinear force control law. This nonlinear design is derived for the class of systems that can be described as a time delay followed by a compliance (where the compliance is capable of being modeled as a monotonic function of displacement). The nonlinear controller was able to track a wide range of inputs up to a maximum force of 400 dN. The closed loop system remained stable. Also, the ability of this controller to reject positional disturbances was found to be better than the other controllers tested. The response to some inputs, however, requires improvement. Specifically, the peak magnitude was higher than the reference force for sinusoidal inputs above 0.5 Hz. In addition, the sinusoidal response began to lag the input for frequencies above 2.0 Hz.

7.1.2 Recommendations

The time delay model is valid for the PUMA arm and VAL-II controller. It may be a valid model for other robots, but not all robots[5]. The frequency response of any robot system should be estimated before implementating a force control law. If the dynamics of the robot and controller are similar to those of the PUMA, then a force controller similar to the one described herein may be valid.

A more rigorous analysis of the nonlinear controller should be performed. The stability of the nonlinear controller was tested by experiments and simulations. Although the controller remained stable for a wide range of conditions, a more careful analysis should be performed to determine the limits of stability. Also, the robustness of the controller to disturbances and parameter variations should be determined.

The nonlinear controller displayed a steady state error during ramp disturbances and modeling errors. Based on laboratory experience, the steady state error caused by an inaccurate compliance model is small (on the order of output noise). However, when grinding on a regular basis, the disk compliance will change as it wears. This may cause a problem, if so it may be beneficial to design a system that estimates the compliance model parameters before each pass. This is a good application for a model reference adaptive system.

The disturbance rejection properties of the controller may be improved. Certainly positional disturbances should be avoided as much as possible by accurately setting up, aligning, and measuring the workpiece. An accurate nominal contour will always improve the force control results (compared to an inaccurate contour). However, some positional disturbances will always exist. The ability to reject those that do occur is dependent on the accuracy of the estimated future force, Ψ_{k+n-1}. Currently, Ψ_{k+n-1} is a function of the measured output and the system states. It may be possible to improve this estimate by additionally considering the time derivatives of the input and output. The idea is to try and estimate the rate of change of the positional disturbance and use this information to improve Ψ_{k+n-1}.

Prefiltering the input force profile prior to each pass should be investigated as a way to improve the magnitude response of the force controller. Since the input signal is known before each grinding pass, a non-causal, linear-phase filter could be used. Thus, the magnitude of the desired input signal could be altered without affecting the phase.

The results of this research suggest that the material removal rate can be indirectly controlled by the applied normal force. CSDL has mounted a lightweight, modified air-powered grinder to the end of the PUMA. Preliminary force control tests with the grinder spinning were performed. Figure 73 shows a preliminary result. With the grinder

spinning, the controller is tracking a sinusoidal input force profile while rejecting a -10% ramp disturbance. The workpiece was measured before and after 4 grinding passes using the same frequency input. The material removal was measured at three points along the width of the workpiece and the results are shown in Figure 74. The reason that the material removal is not uniform across the width of the weld has not been fully analyzed.

The air grinder and force sensor are heavier than the payloads tested during the frequency response experiments discussed in section 3. Their combined weight approaches the payload capacity of the PUMA. Before a complete series of force control experiments is performed, the frequency response of the plant with this payload should be estimated. Because of the added weight, the frequency response may differ from that calculated in this thesis.

Some of the experiments in Section 6 should be repeated during grinding. If it is necessary to add an additional filter to the force measurement, then the extra phase lag should be accounted for. These experiments may show that it is not necessary to alter the plant model used by the force control law during grinding. It may be adequate to simply determine a new plant compliance for the case of the running grinder. Otherwise, a grinding model may have to be integrated into the plant model used by the force controller. One way of doing this that

has been considered at CSDL is to model grinding as a nonlinear damper. Then, the force controller would be redesigned for a plant consisting of a time delay, compliance, and damper in series.

Once the tracking performance of the force controller with the grinder operating is satisfactory, the contours ground into the weld should be characterized. This may be done by using the sinusoidal system identification techniques discussed in section 3. These techniques apply to the characterization of nonlinear systems. In this case, the input is the normal force profile and the output is the change in weld contour. Thus, a sinusoidal normal force would be applied to a flat steel workpiece and the magnitude and phase of the ground contour would be measured. This could be done at many frequencies and amplitudes to build up a function (probably nonlinear) that relates material removal to amplitude and frequency. The results of these experiments could be compared with those predicted by the grinding model currently being developed at CSDL.

In addition to testing force control during grinding, it is important to test force control on complex contours. This would involve the measurement of a complex contour and the generation of a data base. A vision system, such as the one developed at CSDL, would be suitable for this purpose. A camera and light source could be mounted in a fixed position above a table. Then a workpiece could be placed on the table

for measurement. To create the data base, the position of the workpiece would be manually incremented after each measurement. Software would have to translate this data base into a nominal trajectory and download this trajectory to VAL-II. Integration of the system in this way will aid in specifying the level of positional disturbances that the force controller should be designed for.

In addition to the further experiments, force control would be improved by reducing the time delay. This would yield the most significant improvement in force controller performance compared with the other recommendations mentioned.

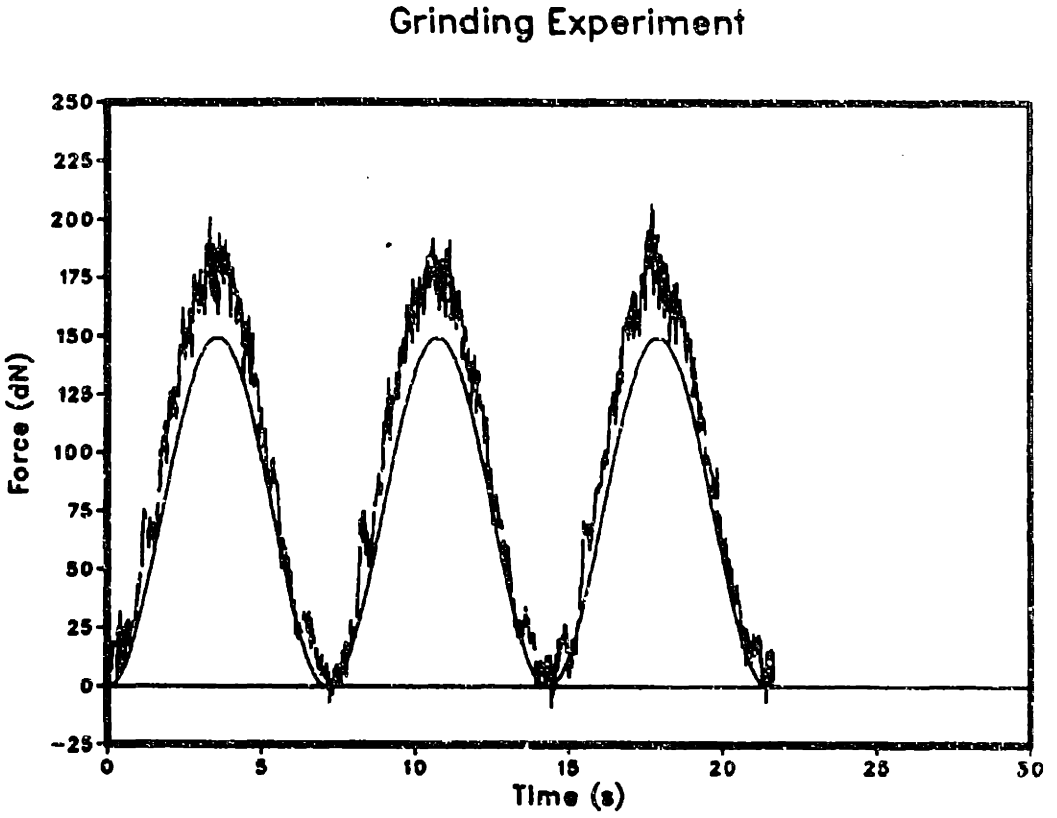

Figure 73. Preliminary force control test with grinder running: (rejecting -10% ramp)

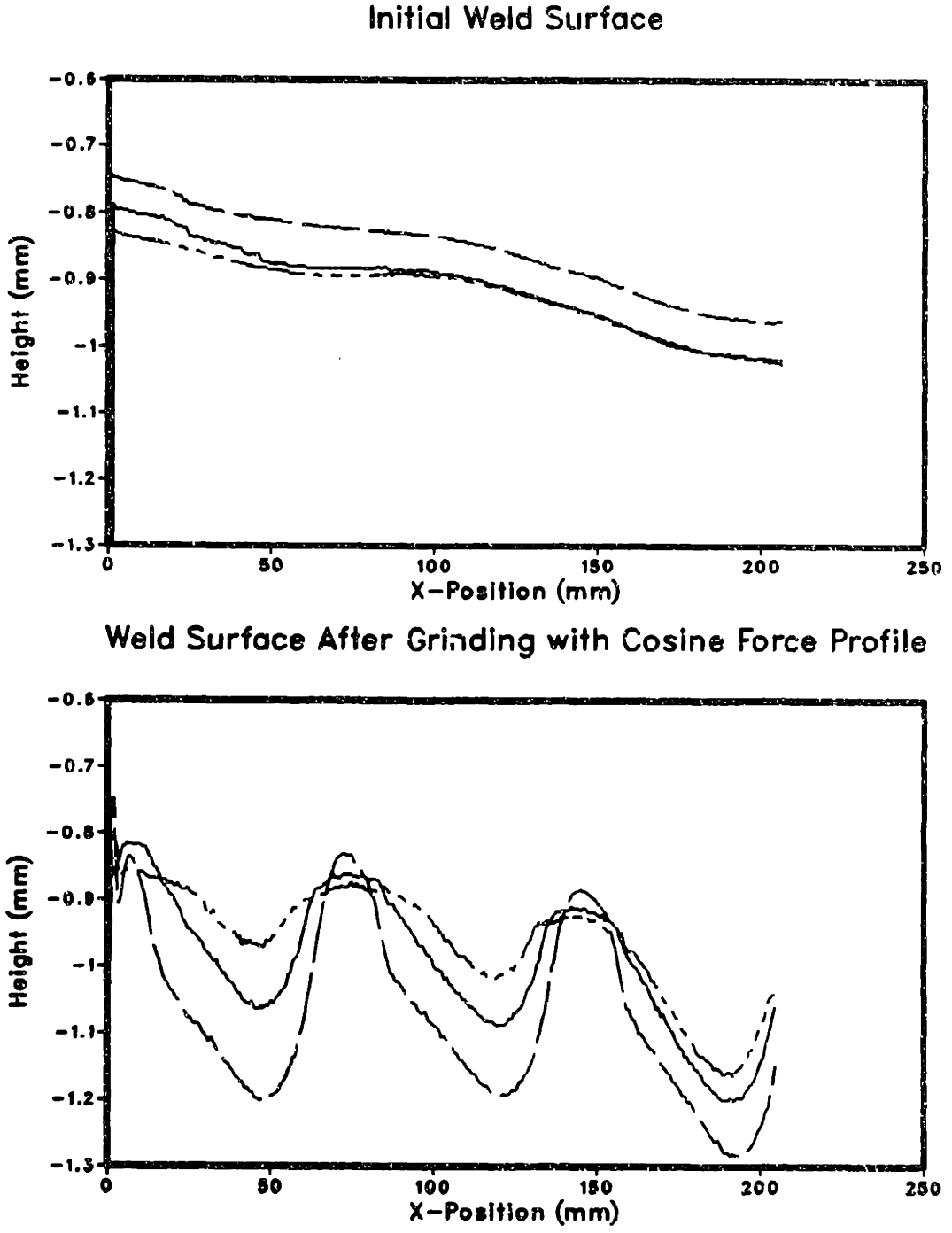

Figure 74. Preliminary material removal data from grinding test

LIST OF REFERENCES

1. Armstrong, B., Khatib, J., and Burdick, J., "The Explicit Dynamic Model and Inertial Parameters of the PUMA 560 Arm", Proceedings of IEEE International Conference on Robotics and Automation 1986, (San Francisco, 1986) pp. 510 - 518.

2. Astrom, K. J. and Wittenmark, B., Computer Controlled Systems - Theory and Design, (Prentice-Hall, Inc., Englewood Cliffs, N.J., 1984).

3. Craig, J. J. and Raibert, M. H., "A Systematic Method of Hybrid Position/Force Control of a Manipulator", Proceedings of IEEE Computer Software & Applications Conference 1979, (Chicago, 1979) pp. 446-451.

4. Drake, S., "Using Compliance in Lieu of Sensory Feedback for Automatic Assemble", Sc.D. Thesis. Department of Mechanical Engineering, Massachusetts Institute of Technology, Cambridge, Ma. (1977).

5. Good, M. C., Sweet, L. M., and Strobel, K. L., "Dynamic Models for Control System Design of Integrated Robot and Drive Systems", Journal of Dynamic Systems, Measurement, and Control 107, 53 (1985).

6. Hogan, N, "Impedance Control: An Approach to Manipulation: Part I - Theory, Part II - Implementation, Part III - Applications", Journal of Dynamic Systems, Measurement, and Control 107, 1. (1985).

7. Hollerbach, J. M., "A Recursive Formulation of Lagrangian Manipulator Dynamics", IEEE Transactions on Systems, Man, and Cybernetics SMC-10, (11) 730 (1980).

8. Ivers, D. E., "Process Modelling of Coated Abrasive Disk Grinding as Part of a Robotic Solution", S.M. Thesis. Department of Mechanical Engineering, Massachusetts Institute of Technology, Cambridge, Ma. (1985).

9. Laming, T. ' 'A Perturbation Approach to Surface Estimation", S. M. Thesis. Department of Mechanical Engineering, Massachusetts Institute of Technology, Cambridge, Ma. (1984).

10. Luh, J. Y. S., "An Anatomy of Industrial Robots and Their Controls", IEEE Transactions on Automatic Control AC-28, (2). 133 (1983).

11. Mason, M. T., "Compliance and Force Control for Computer Controlled Manipulators", IEEE Transactions on Systems, Man, and Cybernetics SMC-II, (6). 418 (1981).

12. Nevins, J. L. and Whitney, D. E., "Computer-controlled Assembly", Scientific American 238, (2). 62 (1978).

13. Paul, R. P., Robot Manipulators: Mathematics, Programming, and Control, (MIT Press Cambridge, Massachusetts and London, England, 1981).

14. Paul, R. and Shimano, B, "Compliance and Control", Proceedings Joint Automatic Control Conference 1976, (San Francisco, 1976) pp. 694 - 699.

15. Raibert, M. H. and Craig, J. J., "Hybrid Position/Force Control of Manipulators", ASME Journal of Dynamic Systems, Measurement, and Control 102, 126 (1981).

16. Salisbury, J. K., "Active Stiffness Control of a Manipulator in Cartesian Coordinates", Proceedings 19th IEEE Conference of Decision and Control 1980, (Alburqueue, 1980) vol. 1. pp. 95 - 100.

17. Stepien, T. M., "A Microprocessor-Based Control System for Robotic Deburring", S.M. Thesis. Department of Mechanical Engineering, Massachusetts Institute of Technology, Cambridge, Ma. (1984).

18. Stepien, T. M., Sweet, L. M., Good, M. C., and Tomizuka, M., "Control of Tool/Workpiece Contact Force with Application to Robotic Deburring", IEEE Journal of Robotics and Automation, to appear in (1986).

19. Sullivan, B. K., "A Structured Light Vision System for Robotic Grinding", S. M. Thesis. Department of Mechanical Engineering, Massachusetts Institute of Technology, Cambridge, Ma. (1986).

20. Welch, P. D., "The Use of Fast Fourier Transform for the Estimation of Power Spectra: A Method Based on Time Averaging Over Short, Modified Periodograms", Modern Spectrum Analysis, D. G. Childers, Ed. (John Wiley & Sons, Inc., New York. 1978), pp. 17 - 20.

21. Whitney, D. E., "Resolved Motion Rate Control of Manipulators and Human Prostheses", IEEE Transactions on Man-Machine Systems MMS-10, (2). 47 (1969).

22. Whitney, D. E., "The Mathematics of Coordinated Control of Prosthetic Arms and Manipulators", Journal of Dynamic Systems, Measurement, and Control, (F) 303 (1972).

23. Whitney, D. E., "Force Feedback Control of Manipulator Fine Motions", Journal of Dynamic Systems, Measurement, and Control 99, 91 (1977).

24. Whitney, D. E., "Historical Perspective and State of the Art in Robot Force Control", IEEE International Conference on Robotics and Automation 1985, (St. Louis, 1985) pp. 262 - 268.

APPENDIX A. CTRL-C SIMULATION FOR NONLINEAR CONTROLLER

```
// Nonlinear Control Law Simulation
erase
clear -v
//Inititialize variables
rand('normal');
n=142;
h=0.028;
a=50.;
w=3.14;
m=0.02;
noise=0;
mmod = 0.01;
gain = 0.14;
b=.20;
bmod = .10;
k1=0.;
k=-1;
lasty=0;
lastd=0;
cntr=0;
lastu = 0;
//
// Calculate input and input time vectors
//
for i = 1:(n+10);...
k = k + 1;...
r(i) = a*(1 - cos(w*k*h));...
end;
//if i < 25; r(i) = 0; else r(i) = 50;...
//
// reset k and find initial u
//
k = -1;
initc=(1/mmod)*log((mmod*r(5) + bmod)/bmod);
du1 = 0;
du2 = 0;
du3 = 0;
du4 = 0;
du5 = 0;
```

```
//
// Start Simulation
//
for i = 1:n;...
        k = k + 1;...
        t(i) = k*h;...
        rp(i) = r(i);...
        du  = du1;...
        du1 = du2;...
        du2 = du3;...
        du3 = du4;...
        du4 = du5;...
        u = lastu + du;...
        lastu = u;...
        d = 0;...
        lastd = d;...
        del = du1 + du2 + du3 + du4;...
        y(i) = noise*rand + (b/m)*(exp(m*(u - d)) - 1);...
        yhat = (y(i) + bmod/mmod)*exp(mmod*del) - bmod/mmod;...
        if i < 6; ri4 = r(i+4); else ri4 = (1-gain)*r(i+4)+gain*yhat;end;...
        du5 = (1/mmod)*log((mmod*r(i+5) + bmod)/(mmod*ri4 + bmod));...
        if i = 1; du5 = du5 + initc;end;...
        data(i, 1) = t(i);...
        data(i, 2) = y(i);...
        inp(i, 1) = t(i);...
        inp(i, 2) = r(i);...
        end;

plot(t,rp,'solid', t,y,'dashed')
ylabel('magnitude',' llllllll')
xlabel('time',' lll')
```

APPENDIX B. SELECTED CODE FROM LABORATORY IMPLEMENTATION OF NONLINEAR CONTROLLER

This code is not a complete program. Only the code for the nonlinear control law has been included.

```
      **** Initialization code  ****
main()
{
      **** Operator Interface code ****

      **** File access code ****

        /* initialize reg */
        clcntr = 0;
        tstcntr = -1;
        tadv = cp.adv;
        tadv_1 = cp.adv - 1;
        m = cp.slope;
        b = cp.yint;
        bovm = b/m;
        movb = m/b;
        invm = 1/cp.slope;
        mmobb = m*m/b*b;
        clgain = (double)cp.kn/cp.kd;
        clgain2 = 1. - clgain;
        lastc = (int)(invm*log((m*d[tadv-1]+b)/b));
        dc1 = 0.;
        dc2 = 0.;
        dc3 = 0.;
        dc4 = 0.;
        dc5 = 0.;

      **** Code to run experiment ****

} /* altrndc3 */
```

```
reg(mforce)
int mforce;
{
        int di_0, di_1, i;
        double rcntrl, cur_pos, pos_in_4;

        tstcntr++;
        i = tstcntr;

        /* remember that mforce has reversed sign!!! */
        mforce = -mforce;

        /* calculate estimated z position */
        if(mforce >= 0){
                cur_pos = invm*log(movb*mforce+1);
        } /* if */
        else{
                cur_pos = -invm*log(-movb*mforce+1);
        } /* else */

        /* update state variables */
        dc1 = dc2;
        dc2 = dc3;
        dc3 = dc4;
        dc4 = dc5;

        /* sum displacement commands in progress */
        pos_in_4 = cur_pos + dc1 + dc2 + dc3 + dc4;
```

```
        /* calculate yhat ( estimated force ) in 4 sample periods */
        if(pos_in_4 >= 0){
                yhat = bovm*(exp(m*pos_in_4) - 1);
        } /* if */
        else{
                yhat = -bovm*(exp(-m*pos_in_4) - 1);
        } /* else */

        /* Find desired force in 4 sample periods accounting for
           measurement.  Wait for 5 samples before starting closed loop */
        if(i < tadv){
                di_1 = d[i + tadv_1];
        } /* if */
        else{
                di_1 = clgain2*d[i + tadv_1] + clgain*yhat;
        } /* else */

        /* Desired force in 5 sample periods */
        di_0 = d[i+tadv];

        /* Calculate change in displacement */
        if( di_0 >= 0 ){
                if( di_1 >= 0){
                dc5 = invm*log((m*di_0+b)/(m*di_1+b));
                } /* if */
                else{
                dc5 = invm*log(movb*di_0-mmobb*di_0*di_1+1-movb*di_1);
                } /* else */
        } /* if */
        else{
                if( di_1 >= 0){
                dc5 = -invm*log(movb*di_1-mmobb*di_0*di_1+1-movb*di_0);
                } /* if */
                else{
                dc5 = invm*log((b-m*di_1)/(b-m*di_0));
                } /* else */
        } /* else */

        rcntrl = lastc + dc5;
        lastc = rcntrl;

        return (int)rcntrl;

} /* reg */

**** Error Handling and minor subroutines ****
```